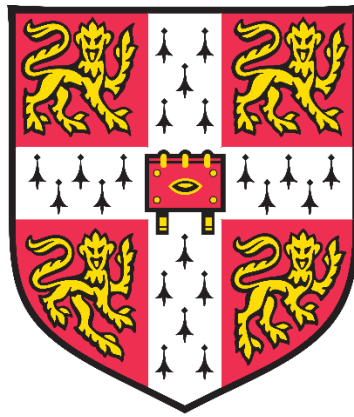


Resistive-type Superconducting Fault Current Limiter (RSFCL) and Its Application in Power Systems



XIUCHANG ZHANG

Churchill College

University of Cambridge

A thesis submitted for the degree of

Doctor of Philosophy

August 2017

Dedicated to my parents

Declaration of Originality

The work presented in this thesis was carried out in Department of Engineering, University of Cambridge, under the supervision of Dr. T. A. Coombs from January 2014 to August 2017.

The author declares that this thesis is his original work, except for where specific reference is made to others' work. This thesis has not been previously submitted in part, or in whole, to any other universities for a degree, diploma or other qualification. This thesis is within the limit of 65,000 words length.

Xiuchang Zhang

Churchill College

October 2017

Abstract

With the rapid increase in electrical loads, a considerable percentage of global power systems have been stretched to their designed capacity, leading to a sharp rise in the fault current. High fault current levels have severe impact on power systems. They can increase the likelihood of overcurrent damage, which may destroy electrical facilities or even cause system blackout. The resistive-type superconducting fault current limiter (RSFCL) is a device that can help to mitigate the increasing level of fault currents. It can also contribute to the performance, stability and efficiency of electricity grids. In order to promote the RSFCL more effectively, it is essential to study the device itself and conduct simulations regarding the performance and applicability from the system point of view.

Chapter 1 and Chapter 2 of this thesis introduced fundamentals of superconductivity and RSFCLs, respectively. In Chapter 3, a power system model was built, and the transient analysis of short-circuit currents was given. Then, the operating principle of RSFCL was explained, and a step-resistance RSFCL model was introduced. To validate the current limiting performance of the SFCL module, wind farm protection schemes were studied under various fault scenarios. After thorough analysis it was concluded that the optimal allocating strategy of SFCLs was the installation of one SFCL at the integrating point of the system model.

Chapter 4 presented a comprehensive study on the performance and optimal allocation strategy of RSFCLs. The two power system models used in this chapter were built based on the UK network standard. To assess the impact of incorporating SC material properties on the performance of SFCLs, three different models were compared throughout the study. Although computing time can be reduced when step-resistance and exponential equation models were used, such simplifications led to strong overestimations of the SFCL performance and resulted in wrong conclusion of

optimal installing strategies. For both power system models, the simultaneous use of three SFCLs was the best protection strategy in terms of the performance, economic efficiency and reliability of the overall grids. To draw this conclusion, all the potential combinations of two, three, four, and five SFCLs were studied under a wide number of fault scenarios and measuring strategies.

In Chapter 5, a series of experiments were performed to study the magnetic field-angular dependence of the critical current of different commercial YBCO samples. We selected ten 2G-HTS tapes with broad differences in width, fabrication process, and laminar structure. The obtained $I_c(B, \theta)$ characteristics of HTS samples were applied in the simulation of RSFCLs, showing unneglectable effect on the first peak limiting performance during faults. This study is helpful to the design and simulation of RSFCLs and other HTS applications which require superconducting wires operating inside magnetic fields.

In Chapter 6, we presented a High Frequency (HF) AC-assisted quench study of the YBCO conductor. The differences in quench processes triggered by HF AC field were recorded and studied. We found that AC signals of 10 kHz can trigger quench of the HTS tape. Also, the device proved to be effective at guaranteeing uniform quench of the sample. After then, we placed the experimental device in a magnet, to study whether the quench process can be accelerated by external DC magnetic field. It was found that the DC field can reduce the quench time, but its performance was dependent on the amplitude of transport current and the characteristics of HF AC signals. In addition, the angle between the DC magnetic field and the tape surface showed a huge impact on the quench time. Finally, a comprehensive field-angular dependence study about the quench time of the YBCO sample was conducted, revealing the same pattern as $J_c(\theta, B)$ dependence of the tape, but with a greater anisotropy. To summarize, this technique showed outstanding performance regarding quench acceleration and tape protection, and therefore has huge potential to be applied in RSFCLs.

Acknowledgement

First and foremost, I would like to express my sincere gratitude to my supervisor, Dr. Tim Coombs, for his superb guidance and generous assistance during my PhD Study. Without his encouragement and insightful ideas, this dissertation could not have been completed.

In the meantime, I would like to express my deep thanks to my fiancée for her continuous support during the last four years. I understand being apart for such a long time is very hard for a girl especially at her age. Thank you so much, my love.

I would like to acknowledge all my colleagues in the superconductivity group at University of Cambridge for their generous assistance and inspiring discussion. I would like to thank Dr Zhaoyang Zhong and Dr Jianzhao Geng, for taking the time and having the patience to explain many fundamental theories of superconductivity, and for their kind and patient help during my studies of simulation and experiment. My gratitude is also to my other group mates Dr Lin Fu, Dr Wei Wang, Dr Zhen Huang, Dr Yujia Zhai, Dr Yiran Chen, Dr Michal Chudy, Boyang Shen, Chao Li, Heng Zhang, Qihuan Dong, Qinyu Wu, and Jamie Gawith, for always being willing to share their innovative ideas and for the invaluable friendship. It has been a great pleasure to work in such a wonderful group.

Last but not least, I am grateful for everything that my family has done for me. I would never have gotten through this without your loving care and support.

List of Publications

1. **X. Zhang**, H. S. Ruiz, J. Geng, & T. A. Coombs. (2017). **Optimal location and minimum number of superconducting fault current limiters for the protection of power grids.** *International Journal of Electrical Power & Energy Systems*, 87(2): 136-143.
2. **X. Zhang**, Z. Zhong, H. S. Ruiz, J. Geng, & T. A. Coombs. (2016). **General approach for the determination of the magneto-angular dependence of the critical current of YBCO coated conductors.** *Superconductor Science & Technology*, 30(2):025010.
3. **X. Zhang**, H. S. Ruiz, J. Geng, B. Shen, L. Fu, H. Zhang, & T. A. Coombs. (2016). **Power flow analysis and optimal locations of resistive type superconducting fault current limiters.** *Springerplus*, 5(1):1972.
4. **X. Zhang**, J. Geng, Z. Zhong, B. Shen, J. Gawith, C. Li, H. Zhang, & T. A. Coombs (2017). **Active quenching technique developed for resistive-type superconducting fault current limiters: quench acceleration and protection.** *Submitted to Superconductivity Science and Technology.*
5. **X. Zhang**, Z. Zhong, J. Geng, B. Shen, C. Li, H. Zhang, Dong Q. & T. A. Coombs (2017). **Magnetic field-angular dependence of critical current and n-values in 2G HTS tapes.** *Submitted to Cryogenics.*
6. B. Shen, J. Geng, **X. Zhang**, L. Fu, C. Li, H. Zhang, Q. Dong, J. Ma, J. Gawith, & T. A. Coombs. (2017). **AC losses in horizontally parallel HTS tapes for possible wireless power transfer applications.** *Physica C: Superconductivity and its Applications*. 543.
7. B. Shen, J. Li, J. Geng, L. Fu, **X. Zhang**, & C. Li, & T. A. Coombs **Investigation and comparison of ac losses on stabilizer-free and copper stabilizer HTS tapes.** *Physica C Superconductivity & Its Applications*, 541, 40-44.
8. B. Shen, J. Geng, C. Li, **X. Zhang**, L. Fu, H. Zhang, Q. Dong & T. A. Coombs (2017). **Optimization study on the magnetic field of superconducting Halbach Array magnet.** *Physica C Superconductivity & Its Applications*, 538, 46-51.
9. B. Shen, J. Li, J. Geng, L. Fu, **X. Zhang**, H. Zhang, Q. Dong & T. A. Coombs (2017). **Investigation of ac losses in horizontally parallel HTS tapes.** *Superconductor Science & Technology*, 30(7).

10. Z. Zhong, M. Chudy, H. S. Ruiz, **X. Zhang**, & T. A. Coombs (2017). **Critical current studies of a HTS rectangular coil.** *Physica C Superconductivity & Its Applications*, 536, 18-25.
11. J. Geng, H. Zhang, C. Li, **X. Zhang**, B. Shen, & T. A. Coombs (2017). **Angular dependence of direct current decay in a closed YBCO double-pancake coil under external ac magnetic field and reduction by magnetic shielding.** *Superconductor Science Technology*, 30(3), 035022.
12. H. Zhang, J. Geng, B. Shen, L. Fu, **X. Zhang**, C. Li, H. Zhang, & T. A. Coombs. (2017). **Magnetization of coated conductor stacks using flux pumping.** *IEEE Transactions on Applied Superconductivity*, 27(4), 1-5.
13. J. Geng, B. Wang, M. Baghdadi, J. Li, B. Shen, H. Zhang, **X. Zhang**, & T. A. Coombs. (2017). **Feedback control of a rectifier type HTS flux pump: stabilizing load current with minimized losses.** *IEEE Transactions on Applied Superconductivity*, 27(4), 1-4.
14. C. Li, B. Li, F. Guo, J. Geng, **X. Zhang**, & T. A. Coombs. (2016). **Studies on the active SISFCL and its impact on the distance protection of the EHV transmission line.** *Protection & Control of Modern Power Systems*, 1(1), 18.
15. J. Geng, B. Shen, C. Li, H. Zhang, K. Matsuda, J. Li, **X. Zhang** & T. A. Coombs. (2016). **Voltage-ampere characteristics of YBCO coated conductor under inhomogeneous oscillating magnetic field.** *Applied Physics Letters*, 108(26), 815.
16. B. Shen, L. Fu, J. Geng, **X. Zhang**, H. Zhang, Dong, Q., & T. A. Coombs. (2016). **Design and simulation of superconducting Lorentz Force Electrical Impedance Tomography (LFEIT).** *Physica C Superconductivity & Its Applications*, 524, 5-12.
17. J. Geng, K. Matsuda, B. Shen, H. Zhang, **X. Zhang**, L. Fu, & T. A. Coombs. (2016). **HTS persistent current switch controlled by ac magnetic field.** *IEEE Transactions on Applied Superconductivity*, 26(3), 1-4.
18. J. Geng, K. Matsuda, L. Fu, J. F. Fagnard, H. Zhang, **X. Zhang**, Q. Dong, & T. A. Coombs. (2016). **Origin of dc voltage in type ii superconducting flux pumps: field, field rate of change, and current density dependence of resistivity.** *Journal of Physics D Applied Physics*, 49(11), 11T01.
19. H. Zhang, J. Geng, B. Shen, **X. Zhang**, M. Baghdadi, & T. A. Coombs. (2016). **Uniform magnetic field mapping with HTS coils: conceptual design and optimization.** *IEEE Transactions on Applied Superconductivity*, 26(3), 1-5.

20. J. Geng, K. Matsuda, L. Fu, B. Shen, **X. Zhang**, & T. A. Coombs. (2016). **Operational research on a high-Tc rectifier-type superconducting flux pump.** *Superconductor Science & Technology*, 29(3), 035015.
21. B. Shen, L. Fu, J. Geng, H. Zhang, **X. Zhang**, Z. Zhong, Q. Dong, & T. A. Coombs. (2016). **Design of a superconducting magnet for Lorentz force electrical impedance tomography.** *IEEE Transactions on Applied Superconductivity*, 26(3), 1-6.
22. H. S. Ruiz, **X. Zhang**, & T. A. Coombs. (2015). **Resistive-type superconducting fault current limiters: concepts, materials, and numerical modelling.** *IEEE Transactions on Applied Superconductivity*, 25(3), 1-5.

Contents

List of Figures	i
List of Tables	x
Chapter 1 Fundamentals of Superconductivity	1
1.1 Meissner effect.....	1
1.2 Classification of superconductors	2
1.2.1 Low T_c and high T_c superconductors.....	2
1.2.2 Type-I and Type-II superconductors.....	4
1.3 Flux pinning and critical current characteristics.....	9
1.4 Critical state models.....	13
1.4.1 The Bean model.....	14
1.4.2 The Kim model.....	17
1.5 Flux creep, flux flow and the Exponential E–J constitutive law	18
1.6 Conclusion	21
Chapter 2 Background of the application of Resistive-type Superconducting Fault Current Limiters (RSFCLs).....	22
2.1 Problems of high fault current levels	22

2.2	Review of Protection Strategies for the Transmission and Distribution Systems	24
2.2.1	Fault location technologies.....	24
2.2.2	Fault prediction technologies	25
2.2.3	Fault protection technologies	26
2.3	Brief Introduction to the Circuit Breaker Concept	27
2.3.1	The operating principle of circuit breakers	27
2.3.2	Types of circuit breakers	29
2.3.3	Disadvantages of circuit breakers.....	31
2.4	Optimal Fault Protection Scheme	31
2.5	Ideal Superconducting Fault Current Limiter Characteristics	33
2.6	Types of Superconducting Fault Current Limiters.....	35
2.7	Operating Principle of the RSFCL.....	36
2.8	Practical Implementation of HTS RSFCLs.....	38
Chapter 3 Preliminary Study of Simulation of RSFCLs in the Power System		43
3.1	A Power System with Grid-Connected Wind Farm	43
3.1.1	Modelling and parameters of the studied system	44
3.1.2	Rated operation state of the system model	48

3.2	Simulations and Analysis of Short-Circuit Fault in the Power System Model	49
3.2.1	Simulations of short-circuit faults in the system model	49
3.2.2	Analysis of the short-circuit fault	51
3.3	Design and Performance Test of an RSFCL Model	55
3.3.1	Operating principle of the RSFCL	55
3.3.2	Design of the RSFCL model	57
3.3.3	Performance test of the RSFCL model	64
3.4	Analysis of System Behaviour under a Distribution Grid Fault	66
3.4.1	Current limiting performance of the SFCL at Location 1	67
3.4.2	Current limiting performance of the SFCL at Location 2	68
3.4.3	Current limiting performance of the SFCL at Location 3	68
3.4.4	Current limiting performance of the simultaneous integration of two SFCLs at Location 1 and Location 4	69
3.5	Analysis of System Behaviours under Customer Grid Fault & Transmission Line Fault	71
3.5.1	Customer grid fault analysis	71
3.5.2	Transmission line fault analysis	72
3.6	Conclusions	73

Chapter 4 Real-Time RSFCL Model and its Optimal Allocation Strategies in Power Systems	76
4.1 Conventional Modelling Methods of RSFCLs for Power System Protection	76
4.2 Topology of the Power System and the RSFCL Models	79
4.2.1 Modelling of the power system based on the UK network standards	
79	
4.2.2 The step-resistance RSFCL model	82
4.2.3 The real time E-J power law RSFCL model	82
4.3 Network Stability, Current Limiting Performance and Recovery Characteristics.....	85
4.4 Identification of the Optimal Location	92
4.4.1 Single SFCL installation.....	93
4.4.2 Multiple installation of SFCLs	97
4.5 Comparison between Behaviours of the Exponential-Resistance and E-J Power Law RSFCL Models	104
4.5.1 The power system and RSFCL models	105
4.5.2 Performance analysis of the RSFCL models	108
4.5.3 Optimal installation strategies of the RSFCLs	110
4.6 Conclusions.....	115

Chapter 5 General Approach for Determining the Magnetic Field-Angular Dependence of Critical Current of YBCO Tapes for RSFCLs 117

5.1 Introduction..... 117

5.2 Experimental Setup..... 119

5.3 Measured YBCO Coated Conductors 123

5.4 Generalizing the magnetic field-angular function $I_c(\mathbf{B}, \theta)$ 125

5.5 Validation of the Fitting Function $I_c(\mathbf{B}, \theta)$ Using the second Group of YBCO Samples..... 134

5.6 Simulation of RSFCLs behaviours with consideration of the magnetic field-angular dependence of critical current $I_c(\mathbf{B}, \theta)$ 138

5.7 Conclusion 142

Chapter 6 Active Quenching Technique Developed for RSFCLs: Quench Acceleration and Protection 143

6.1 Introduction..... 143

6.2 Experimental System 144

6.3 Study of Quench Triggered by HF AC Magnetic Field 147

6.3.1 Transient study of the quench development..... 147

6.3.2 Study on influence factors of the quench time 151

6.4 Study of Active Quench under Various External DC Fields..... 155

6.4.1 Field-angular dependence of critical current of the studied sample.....	155
6.4.2 Relationship between the quench time and the intensity of DC background field	158
6.4.3 Relationship between the quench time and the angle of DC background field	161
6.4.4 Magnetic field-angular dependence of the quench time	163
6.5 Conclusion	164
Chapter 7 Conclusions and Future Work.....	166
References	170

List of Figures

Figure 1.1: Illustration of the Meissner effect: the field cooling response of an ideal conductor and a superconductor..... 1

Figure 1.2: The critical current characteristics and the history of discovery of some important superconducting materials [7]. The world record of the highest critical temperature of 200 K was achieved by H_2S under high pressure at 150 GPa. This temperature is higher than the lowest atmospheric temperature in Antarctica.4

Figure 1.3: Phase diagram of type-I and type-II superconductors. (a) The type-I superconductor only has one critical field, beyond which the material enters the normal state directly. (b) Type-II superconductors have two critical fields, H_{c1} and H_{c2} . When under applied fields between H_{c1} and H_{c2} , the materials are in a transactional phase where magnetic flux enters the superconductors in the form of fluxons.5

Figure 1.4: The magnetization characteristics of type-I ((a) and (b)) and type-II ((c) and (d)) superconducting materials [8].6

Figure 1.5: Variation trends of the number of super electrons, n_s^* , and decay of the magnetic field, H , with respect to the increasing distance from the surface of (a) type-I and (b) type-II superconductors. The penetration depth, λ , and the coherence length, ξ , are shown. Type-I superconductors have GL parameter $\kappa = \lambda/\xi < 1/2$ and type-II superconductors have GL parameter $\kappa = \lambda/\xi > 1/2$8

Figure 1.6: The structure of a single vortex [11]. The core region can be considered to be a normal region, surrounded by a circulating current which shields the magnetic field.....	10
Figure 1.7: Two neighbouring vortices of a type-II superconductor [13]. For simplification of the analysis, the current distribution of each vortex is assumed to be uniform in the area of the other vortex.....	10
Figure 1.8: An Abrikosov flux line lattice of <i>NbSe2</i> at 1.8 K under a 1 T magnetic field. The figure was experimentally observed using a scanning tunnelling microscope [16].	11
Figure 1.9: Illustration of defects proposed as flux pinning sites in YBCO thin films [18].....	12
Figure 1.10: A superconducting slab with infinite length in the y-z plane. A magnetic field is applied in the z direction.	15
Figure 1.11: Further demonstration of the field-current characteristics of the Bean model: the relationship between the induced screening current and variation in the applied magnetic field.....	16
Figure 1.12: Current characteristics of type-II superconductors: flux creep state, flux flow state and normal state.	18
Figure 1.13: The energy landscape of a pinned vortex under a uniform external current.	19
Figure 1.14: The E-J power law model with different n values. n=1 and n=∞ correspond to the linear Ohm's law and the Bean model, respectively.	21

Figure 2.1: Diagram of the phasor measurement units (PMU) fault location method [42].	25
Figure 2.2: The principle and procedure of AC Current Breaking. The arc can restrike after action of the breaker if the voltage is high enough.	28
Figure 2.3: The current waveform and total time between the start and clearance of a fault. The time required to cut the fault is composed of the relay operating time and breaking time.	28
Figure 2.4: Electrical Circuit of an RSFCL. The impedance R_p and L_p stands for the shunt impedance of the RSFCL.	36
Figure 3.1: Model of the studied power system which has a grid-connected wind power plant.....	45
Figure 3.2: Voltage curves at the substation TR2 (Bus 1) under normal operation.	48
Figure 3.3: Power flow at various places in the studied power system model. ...	49
Figure 3.4: Locations of the three proposed faults in the studied power system model.....	50
Figure 3.5: Current flowing from transformer 2 (Bus 3) and wind farm (Bus 4) to domestic load branch & total current of domestic loads (Bus 5).....	51
Figure 3.6: Single-phase equivalent circuit diagram of a power system [120]. ..	52
Figure 3.7: Diagram of the voltage angle and the impedance angle during normal operation [119].....	53

Figure 3.8: Diagram of the periodic and the aperiodic components of short-circuit current [121].....	55
Figure 3.9: Equivalent diagram of a simple power circuit (a) without and (b) with SFCL [122].	56
Figure 3.10: Phase A of the SFCL model developed in the Simulink/SimPowerSystem module of Matlab.....	58
Figure 3.11: The current limiting behaviour of the SFCL while it is under a short-circuit fault. For the sake of clarity, only current profiles of one phase are plotted.	60
Figure 3.12: Diagram of the single phase of the advanced SFCL model which has the switching branch.	61
Figure 3.13: Performance of the advanced SFCL model and the corresponding Bus 2 current profiles.	63
Figure 3.14: Current curves at substation TR2 without and with application of 5, 10, 15, 20, 25, 30, and 35 Ω RSFCLs.	64
Figure 3.15: Four possible locations for installation of SFCLs in the studied system model.....	66
Figure 3.16: Current output of the wind farm when the distribution fault happens (with and without the SFCL at Location 1).	67
Figure 3.17: Current output of the wind farm when the distribution fault happens (without SFCL, SFCL at Location 1, and SFCL at Location 2).	68

Figure 3.18: Current output of the wind farm when the distribution fault happens (with and without the SFCL at Location 3).	69
Figure 3.19: Current output of the wind farm when the distribution fault happens (without and with SFCLs at Location 1 and Location 4).....	70
Figure 3.20: Current flowing into the domestic branch under a customer grid fault (without and with different SFCL installation strategies).....	71
Figure 3.21: Current output of the wind farm when the transmission line fault happens (without and with different SFCL installation strategies).....	73
Figure 3.22: Reduction of fault current of wind farm achieved by SFCLs at different locations.	74
Figure 4.1: The power system model built based on the UK grid standard. Three prospective fault positions and five potential SFCL locations are illustrated.	81
Figure 4.2: Performance comparison between the step SFCL model and the E–J power law based SFCL model: (a) resistance growth, (b) fault current characteristics, (c) current distribution in the SFCL, (d) temperature curves of each phase. The displayed insets in subplots (a) and (d) are measured in the corresponding units of the main plot.....	86
Figure 4.3: Generator parameters and voltages of branch 2 in response to a 200 ms three-phase to ground fault at branch 1.....	87
Figure 4.4: Current curves of phase A under a branch 1 fault (Fault 1) when the SFCL resistance increases from 0.2 R to 2.0 R.	89

Figure 4.5: SFCL resistance and temperature dynamics with and without the assistance of the Bypass switch strategy shown in the bottom of the figure.	91
Figure 4.6: Flowchart of the algorithm for determining optimal installation strategy of SFCLs. Parameters being initialized during the third step: number of $k = 1$; number of installed SFCL $Sk = 1$; maximal current reduction $Rm = 0$; current reduction margin of one additional $SFCL = CRM$; number of measured points Cm ; optimal strategy $OP = 0$	93
Figure 4.7: Reduction in first peaks of fault currents achieved by single SFCL installed at different locations of the power system.....	95
Figure 4.8: Reduction in first peaks of fault currents achieved by different combinations of dual SFCLs.....	97
Figure 4.9: Total reduction in first peaks of fault currents achieved by different combinations of three SFCLs.....	99
Figure 4.10: Total reduction in first peaks of fault currents achieved by different combinations of four and five SFCLs.	101
Figure 4.11: Single-line diagram of the power system layout considered as the case study.	107
Figure 4.12: Fault-current limiting dynamics of SFCL-3 responding to Fault-1. The current sharing profile between the SC and the shunt resistance of the E-J power law SFCL model is also displayed.	109
Figure 4.13: First peak limiting performance of the 31 installation strategies. Results are shown only for the most hazardous measurement conditions	

identified during the analysis. The green dash-dotted lines show the prospective fault current levels without the SFCLs. The red dashed lines represent the current levels for the normal operation of the power grid (I_n), and the threshold value for safety regulation (I_{sr}) is defined as three times this value (purple solid lines) as common practice.....	112
Figure 4.14: Flowchart of the algorithm for the identification of the optimal SFCL strategy.....	113
Figure 5.1: Picture of the sample holder and the neck offset for coaxial configuration.....	120
Figure 5.2: Picture and dimensional drawing of the rotation stage. The high precision manual rotation stage had a graduation of 1° and vernier of 5.	120
Figure 5.3: Picture of the Agilent 6680A 5000-Watt system power supply, 5V, 875A.....	121
Figure 5.4: Picture of the experimental apparatus.	122
Figure 5.5: In-field magneto-angular dependence of the critical current I_c for the 2G-HTS tapes summarized in Table 5.1. Solid symbols correspond to the experimental data acquired for an external magnetic field of 50 mT (red-squares), 100 mT (yellow-triangles), 200 mT (blue-diamonds), 300 mT (green-circles), and 400 mT (purple-triangles), respectively. Solid lines, correspond to the results obtained from our extended version of the Kim's model. As greater the applied magnetic field is, the lower the critical current. The orientation of the field angle and the direction of the transport current for all cases is illustrated in the top-left pane of the figure.	126

Figure 5.6: Magnetic field-angular dependence of measured commercial YBCO tapes: comparison between experimental data (symbols) and fitting curves (solid lines). Experimental measurement at less important angles was not plotted for clarity.....	134
Figure 5.7: Comparison between current limiting performance of the original E-J power law RSFCL model and the E-J model with $J_c(\theta, B)$ dependence. The fault level without RSFCL is 23 kA. ($\theta = 90^\circ$, magnetic field perpendicular to the ab-plane)	140
Figure 5.8: Comparison between current limiting performance of the original E-J power law RSFCL model and the E-J model with $J_c(\theta, B)$ dependence. The fault level without RSFCL is 9 kA. ($\theta = 90^\circ$, magnetic field perpendicular to the ab-plane)	141
Figure 6.1: Schematic drawing of the experimental system.	145
Figure 6.2: (a) Picture of the sample holder in the air gap of the field magnet. (b) Picture of the 2G HTS tape that placed in the middle of two coupled copper coils.....	146
Figure 6.3: Dynamic voltage characteristics of the YBCO wire under HF AC magnetic field. The YBCO wire was carrying transport current of 150A. The frequency and intensity of the HF AC field were 50 kHz and 20 mT, respectively. The magnetic field was applied for 5 ms.....	148
Figure 6.4: Dynamic voltage characteristics of the YBCO wire under the HF AC magnetic field of 9 ms.....	149

Figure 6.5: Dynamic voltage characteristics of the YBCO wire under the HF AC magnetic field of 10 ms.....	149
Figure 6.6: Dynamic voltage characteristics of the YBCO wire under the HF AC magnetic field of 15 ms.....	150
Figure 6.7: In-field magnetic-angular dependence of the studied sample: experimental data (symbols) and fitting curves (solid lines). Experimental measurements at less important angles were not plotted for clarity.	157
Figure 6.8: Reduction in quench time caused by the increase of DC field intensity and the HF AC field frequency. The transport current remained at 100 A and the intensity of HF AC field was set at 10 mT. The direction of DC field was always perpendicular to the sample surface.....	159
Figure 6.9: Quench time of the sample when quench processes were triggered by 10 kHz/ 20 mT AC magnetic field. The experiments were conducted when the sample was placed in different DC background fields and carried different transport current. See Figure 6.7 for the data of I_c for the sample.	160
Figure 6.10: Angular dependence of quench time under 300 mT DC background field. The sample carried 100 A transport current, and its quench procedures were triggered by 10 mT HF AC magnetic field with frequency of 10 kHz, 20 kHz and 50 kHz.	162
Figure 6.11: Magnetic field-angular dependence of quench time of the YBCO sample. The transport current of the tape was 100 A and the HF AC field used to trigger quench processes was 10 kHz/ 20 mT.	163

List of Tables

Table 2.1: Different options to reduce short-circuit currents [34]. The methods were categorized based on two standards.	32
Table 2.2: Current status of the RSFCLs that have already been field-tested over the world.	42
Table 3.1: Technical parameters of the transformers in the power system model.	47
Table 3.2: Technical parameters of the transmission lines in the power system model.....	47
Table 3.3: Fundamental parameters of the RSFCL model.....	58
Table 3.4: Performance of RSFCLs with various quench impedance.	65
Table 4.1 Legend meanings for Figure 4.7 to Figure 4.10.....	94
Table 4.2: Optimal installation strategies for SFCLs according to the step-resistance and E–J power law models.....	103
Table 4.3: Parameters of the loads, transformers and transmission lines.	106
Table 4.4: Calculated recovery time t_r of the SFCLs depicted in Figure 4.11 without (-) and with (*) the assistance of bypass switches.....	110
Table 4.5: Table of protection strategies, s , accounting for the deployment of up to five SFCLs.	111

Table 4.6: Operational safety margin (OSM) for the s protection strategies, which consider the installation of up to 3 RSFCLs.	115
Table 5.1: Technical parameters of the first group of 2G-HTS tapes.	124
Table 5.2: Technical parameters of the second group of 2G-HTS tapes.....	125
Table 5.3: In-field magneto-angular dependence of the critical current I_c for the 2G-HTS tapes summarized in Table 5.1 for the external magnetic field intensities displayed in Figure 5.5, and for the angles $\theta = 0^\circ$ ($B//ab - plane, B \perp I$) and $\theta = \pm 90^\circ$ ($B//c - axis, B \perp I$).....	127
Table 5.4: Fitting parameters found after the minimization procedure of Equation 5.5 is performed, it leading to Equation 5.6 and the matching of the experimental results displayed in Figure 5.5.	132
Table 5.5: Percentage decline (Pd) of magnetic field-critical current (50 mT and 300 mT, 0° and $\pm 90^\circ$) with respect to self-field critical current for the studied 2G-HTS tapes	135
Table 5.6: Optimal fitting parameters of the tapes and corresponding precision information.....	138
Table 6.1: Variation of quench time along with change in transport current and applied HF AC magnetic field	152

Chapter 1

Fundamentals of Superconductivity

On July 10, 1908, Dutch physicist Heike Kamerlingh Onnes, director of the low-temperature laboratory at Leiden University, successfully liquefied helium. This breakthrough made it possible to study the characteristics of different materials in ultra-cold environments. Three years later, using liquid helium as a refrigerant, Professor Onnes found that the electrical resistance of solid mercury abruptly disappeared at the temperature of 4.19 K [1], which opened the door to more than a century's research regarding a completely new area of scientific study: superconductivity.

1.1 Meissner effect

Nowadays, the definition of superconductivity includes not only zero electrical resistance but also the expulsion of magnetic flux fields occurring in certain materials, which are called superconductors. The phenomenon of perfect diamagnetism was discovered by W. Meissner and R. Ochsenfeld in 1933 [1], and after became known as the Meissner effect.

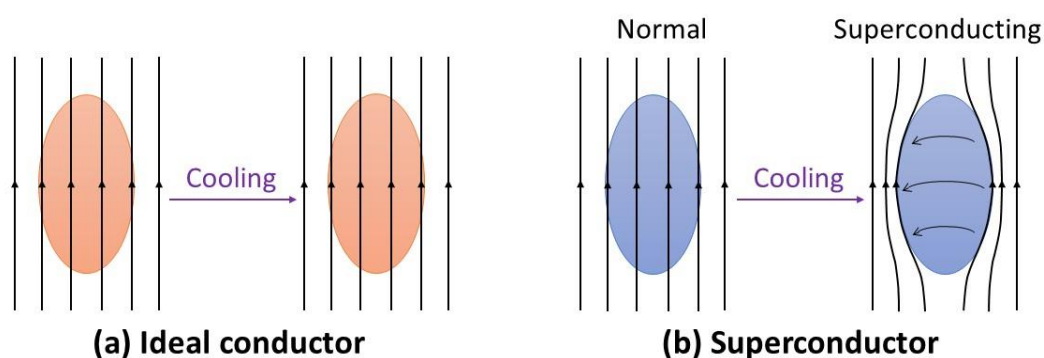


Figure 1.1: Illustration of the Meissner effect: the field cooling response of an ideal conductor and a superconductor.

The perfect conductivity of an ideal conductor determines that the magnetic flux inside the material cannot change ($dB/dt = 0$). Hence, the magnetic field inside the sample remains unchanged after the field cooling process (when a magnetic field is applied prior to cooling), as illustrated by Figure 1.1 (a). However, Figure 1.1(b) shows that a superconductor exhibits an entirely different characteristic: the magnetic field can go through the superconductor when it is in the normal state, but all the magnetic field is expelled after the superconductor is cooled below its critical temperature (T_c), except for at the surface of the material. The Meissner effect occurs due to a shielding current induced by the applied magnetic field. The shielding current develops at the surface of the superconductor. Since the critical current density cannot be infinitely high, the magnetic field must penetrate into the superconductor to a certain depth, defined as the penetration depth, λ , of the superconductor (which will be discussed in the next section). Perfect diamagnetism implies that when the Meissner effect is active, a superconductor has a magnetic susceptibility $\chi = -1$.

1.2 Classification of superconductors

Since Onnes discovered the zero-resistance characteristic of mercury immersed in liquid helium, scientists have never stopped exploring new materials which possess this marvellous property. Intuitively, based on the magnitude of the critical temperature, superconducting materials are categorised into low T_c and high T_c superconductors. As more was learnt about these new materials and their characteristics, researchers defined type I and type II superconductors according to their different responses to applied fields.

1.2.1 Low T_c and high T_c superconductors

Over more than a century's exploration, scientists have made tremendous advances in both theoretical explanations and experiments, and new materials were found in

quick succession. In 1961, Nb_3Sn was found by Kunzler, the first superconducting material which could be used in high-field applications. This compound is capable of preserving its critical current density, $J > 105 \text{ A} \cdot \text{cm}^{-2}$, at 4.2 K while under a magnetic field of 8.8 T [2].

In 1986, J.G. Bednorz and K.A. Muller discovered that the critical temperature of copper oxide based superconductors can reach 35 K [3]. This was used as the boundary to distinguish low T_c from high T_c superconductors. This remarkable scientific result significantly expanded people's expectations for the development of superconductivity. During the decade after that, a series of superconducting materials were synthesized, including the most studied representatives, $YBa_2Cu_3O_7$ (YBCO) and $Bi_2Sr_2CaCu_2O_8$ (BSCCO), the critical temperatures of which are 93 K and 105 K, respectively [4, 5]. Up to now, the highest critical temperature achieved at atmospheric pressure was 135 K, for $HgBa_2Ca_2Cu_3O_3$. H_2S claimed the world record for the highest critical temperature of 200 K under high pressure at 150 GPa [6].

The discovery of YBCO and BSCCO aroused keen research interest around the world due to their engineering-level critical currents and critical magnetic fields. Since the critical temperatures of YBCO and BSCCO are both higher than the boiling point of liquid nitrogen at 77 K, high-cost liquid helium based cryogenic systems are no longer necessary. The significant reduction in cooling costs is another important reason that the application of high T_c superconductors has become such a hot research topic over the years. Figure 1.2 illustrates the critical current characteristics and the history of discovery of some important superconducting materials.

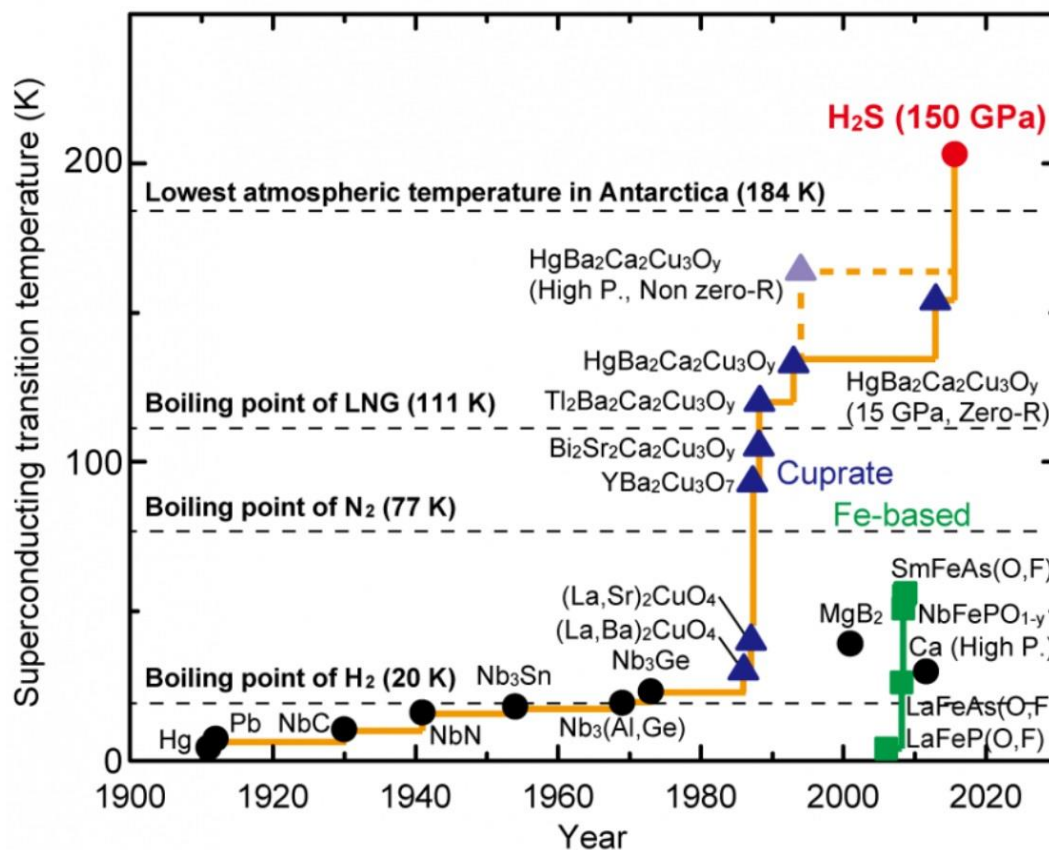


Figure 1.2: The critical current characteristics and the history of discovery of some important superconducting materials [7]. The world record of the highest critical temperature of 200 K was achieved by H_2S under high pressure at 150 GPa. This temperature is higher than the lowest atmospheric temperature in Antarctica.

1.2.2 Type-I and Type-II superconductors

Superconducting materials can be categorised into Type-I and Type-II superconductors based on their different reactions to applied fields. When under an external magnetic field, initially all superconductors enter the Meissner state. However, superconducting materials can have different behaviours as the field intensity increases. Some superconductors directly return to the normal state after the applied field exceeds the critical magnetic field, and these are defined as type-I superconductors. Type-II superconductors are those which have a transitional phase between the superconducting state and the normal state. Unlike type-I superconductors which only have one critical

field, H_c , type-II superconductors have two critical fields: the lower critical field, H_{c1} , and the upper critical field, H_{c2} , as shown in Figure 1.3. With an applied field smaller than the lower critical field, H_{c1} , type-II superconducting materials show perfect diamagnetism. When the external magnetic field increases to levels between H_{c1} and the upper critical field, H_{c2} , magnetic flux enters the superconductors in the form of fluxons, and this state is called the mixed state. If the applied field is higher than H_{c2} , the materials lose their superconductivity and become normal.

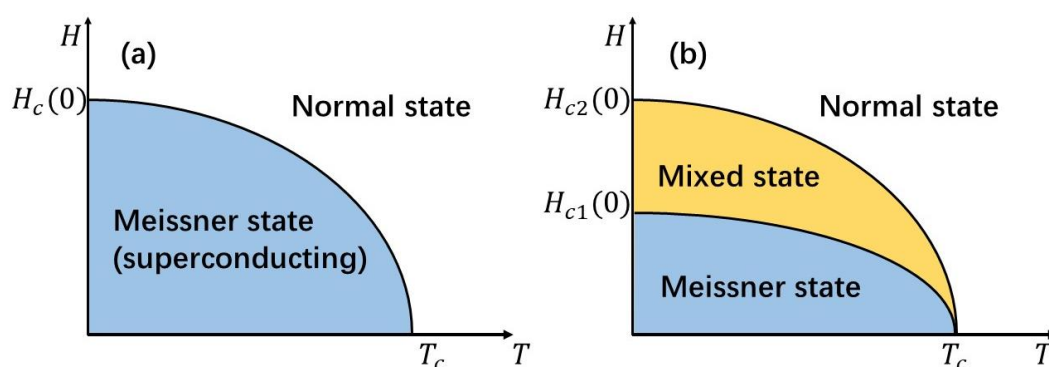


Figure 1.3: Phase diagram of type-I and type-II superconductors. (a) The type-I superconductor only has one critical field, beyond which the material enters the normal state directly. (b) Type-II superconductors have two critical fields, H_{c1} and H_{c2} . When under applied fields between H_{c1} and H_{c2} , the materials are in a transitional phase where magnetic flux enters the superconductors in the form of fluxons.

Figure 1.4 demonstrates the magnetization and internal magnetic field of type-I (subfigures (a) and (b)) and type-II (subfigures (c) and (d)) superconducting materials when the superconductors are placed in external magnetic fields. As can be seen from the figure, type-I superconductors remain perfectly diamagnetic when the applied field is lower than the critical field. During this period, the applied field is entirely expelled from the materials. However, when B_a becomes higher than B_c , the magnetization suddenly drops to zero and full penetration of the applied field occurs. Hence, it can be concluded that for type-I superconductors, a small increase of magnetic field near B_c can lead to a very sharp transition to the normal state.

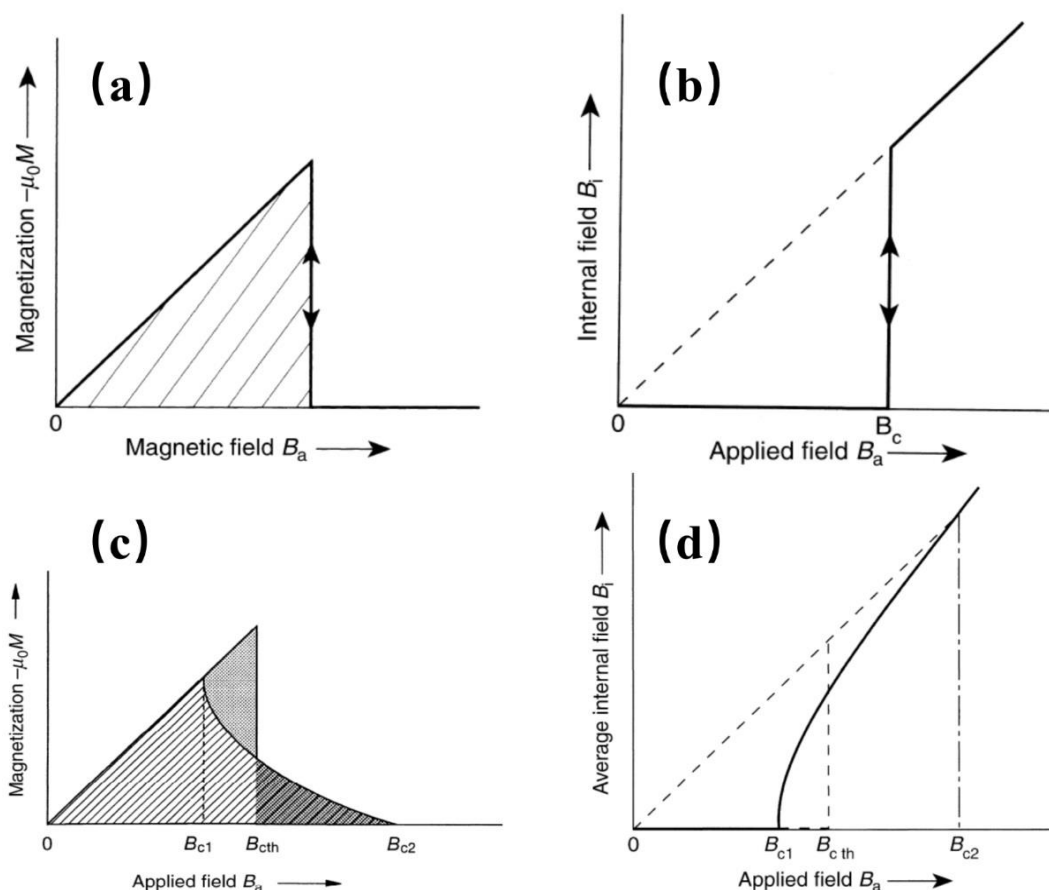


Figure 1.4: The magnetization characteristics of type-I ((a) and (b)) and type-II ((c) and (d)) superconducting materials [8].

Like type-I superconductors, the susceptibility of type-II superconductors also remains at -1 when $B < B_{c1}$, which indicates that the Meissner effect is effective during this period. As the applied field increases further, the susceptibility gradually grows until the magnetic field starts penetrating into the sample from the surface. This transition which involves partial penetration of the magnetic flux is defined as the mixed state, or the *Shubnikov* phase. Finally, the susceptibility reaches zero at $B = B_{c2}$ where the internal field equals the external field, and the superconductivity of the material vanishes. Most type-II superconductors are alloys and compounds, such as Nb_3Sn , MgB_2 and the family of high- T_c cuprates. Unlike type-I superconductors which have a critical magnetic field of usually a few milli-Tesla, type-II materials normally have a much higher upper critical field [9].

Theoretically, the difference between type-I and type-II superconductors can be macroscopically explained by a theory developed by V. L. Ginzburg and L. D. Landau in 1950: the Ginzburg-Landau (GL) theory [10]. This theory proposed a phenomenological explanation of superconductivity with the aid of general thermodynamic arguments, and enabled the calculation of the lower and upper critical magnetic fields, H_{c1} and H_{c2} .

Minimization of the free energy inside the superconducting materials enables two differential equations to be derived, and two important characteristic length parameters of superconductivity, the penetration depth, λ , and the coherence length, ξ , can be obtained from solving the two GL equations. The penetration depth, λ , describes how deep the magnetic field can penetrate a superconductor. The coherence length, ξ , represents the distance within which the density of super electrons is too low for the material to be considered in the superconducting state. It has been stated before that the main difference between type-I and type-II superconductors is whether the material enters the normal state directly after penetration of the magnetic field, or whether a mixed phase exists during the transition. Therefore, the two types of superconductors can be distinguished by the ratio between the penetration depth and the coherence length which called the Ginzburg-Landau parameter:

$$\kappa = \frac{\lambda}{\xi} \quad (1.1)$$

According to the definitions of λ and ξ , a superconducting sample with $\kappa < 1$ implies that it is a type-I superconductor, otherwise the sample belongs to the second type. The reason for this is that $\xi > \lambda$ means that the mixed state doesn't exist, and the superconductivity of the sample breaks down immediately as long as the magnetic field penetrates the interior. Type-I and type-II superconductors tend to have huge differences in their GL parameters. For instance, as a type-I material, lead has $\kappa = 0.48$, while the κ value of YBCO is 95. A more specific method for the classification of type-I and

type-II involves the thermodynamic quantity of B_{c2} , which can be obtained using the GL theory [11]:

$$B_{c2} = \kappa\sqrt{2}B_{c1} \quad (1.2)$$

It can be deduced from Equation 1.2 that only one critical magnetic field exists when the GL parameter of a superconducting sample $\kappa < 1/\sqrt{2}$, suggesting that the sample is a type-I superconductor. A sample with $\kappa > 1/\sqrt{2}$ means it has both lower and upper critical fields, hence it is a type-II superconductor (see Figure 1.5).

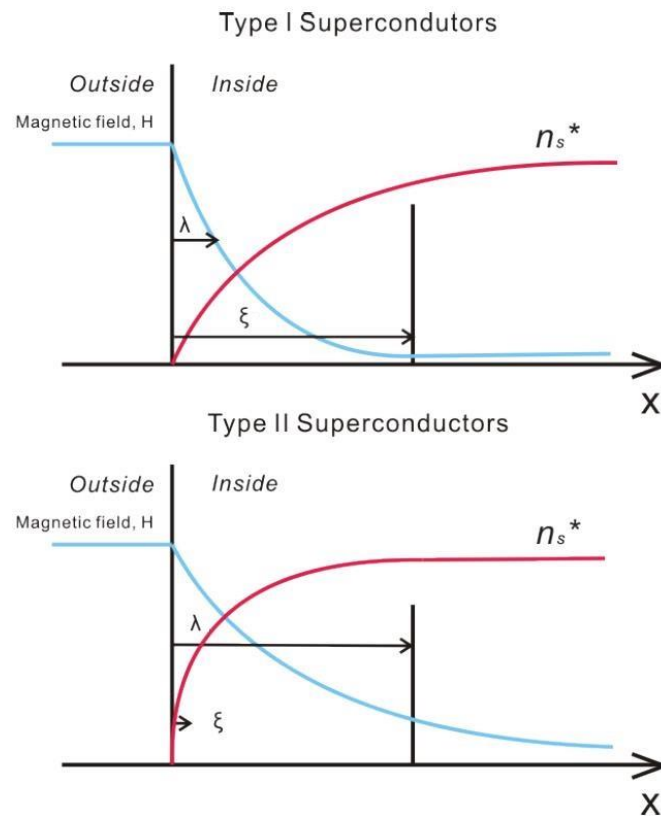


Figure 1.5: Variation trends of the number of super electrons, n_s^* , and decay of the magnetic field, H , with respect to the increasing distance from the surface of (a) type-I and (b) type-II superconductors. The penetration depth, λ , and the coherence length, ξ , are shown. Type-I superconductors have GL parameter $\kappa = \lambda/\xi < 1/\sqrt{2}$ and type-II superconductors have GL parameter $\kappa = \lambda/\xi > 1/\sqrt{2}$.

1.3 Flux pinning and critical current characteristics

As stated in the previous section, the magnetic field must penetrate into the superconductor to a certain depth since the critical current density cannot be infinitely high. The normal—superconducting interface of a superconductor is created by the magnetic energy within the penetration depth. In order to drive the superconducting material into the normal state, energy from the magnetic field is required to break off the super electrons within the coherence length. Hence, the surface energy of the normal—superconducting interface of superconductors can be studied using the penetration depth, λ , and the coherence length, ξ .

Using A to represent the area of the interface, the magnetic energy, E_1 , which penetrates the superconductor can be expressed by:

$$E_1 = \lambda A \frac{1}{2\mu_0} B_c^2 \quad (1.3)$$

The energy needed to break down the super electrons within the coherence length is:

$$E_2 = \xi A \frac{1}{2\mu_0} B_c^2 \quad (1.4)$$

Therefore, the energy absorbed by the interface is the abstraction of E_1 and E_2 :

$$\Delta E = E_1 - E_2 = A \frac{1}{2\mu_0} B_c^2 (\xi - \lambda) \quad (1.5)$$

For a type-II superconductor, the penetration depth is usually much greater than the coherence length, which means that the surface energy is negative, and the direction of energy transfer is from the interface to the superconductor. The energy gained by the superconductor tends to increase with the expansion of the area of normal—superconducting interface. This phenomenon maximises the interface area, A . The

maximum area ultimately leads to nucleation of the vortices, each vortex containing a single magnetic fluxon.

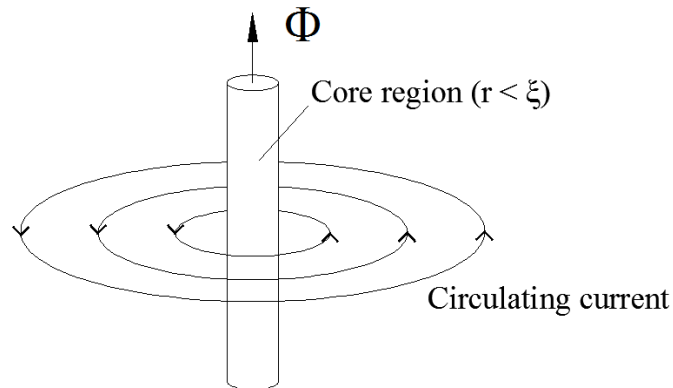


Figure 1.6: The structure of a single vortex [11]. The core region can be considered to be a normal region, surrounded by a circulating current which shields the magnetic field.

The structure of a single vortex can be seen in Figure 1.6. It has a core region with a diameter of the coherence length, ξ . The material within the core region can be considered to be in the normal state due to the low density of super electrons. The circulating current flows in the region surrounding the core region to shield the magnetic field. A vortex in the mixed state, including the core region and the circulating current, is treated as a whole body. When the circulating current is effected by a Lorentz force, the force is considered to be transmitted to the entire vortex [12].

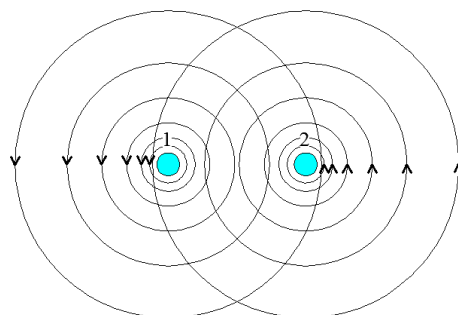


Figure 1.7: Two neighbouring vortices of a type-II superconductor [13]. For simplification of the analysis, the current distribution of each vortex is assumed to be uniform in the area of the other vortex.

For two neighbouring vortices with a short distance, as shown in Figure 1.7, each vortex experiences a repulsive force with the same magnitude and opposite direction, originating from the interaction of the two circulating currents. When the superconductor doesn't carry a critical current, the vortices reach a stable arrangement under the influence of interparticle repulsive forces and the magnetic stress, which is known as the Abrikosov flux line lattice (FLL) [14]. The FLL refers to a hexagonal distribution, as can be seen in Figure 1.8. This perfect hexagonal pattern only appears in pure superconducting materials. The uniform distribution can minimize the potential energy between vortices, but it also means that a magnetic gradient cannot form. According to Ampere's law, a zero magnetic gradient implies zero current. Hence, neither a magnetization current nor transport current can flow in a pure type-II superconductor without destroying its superconductivity [15], which means that pure type-II superconductors are not suitable for engineering applications.

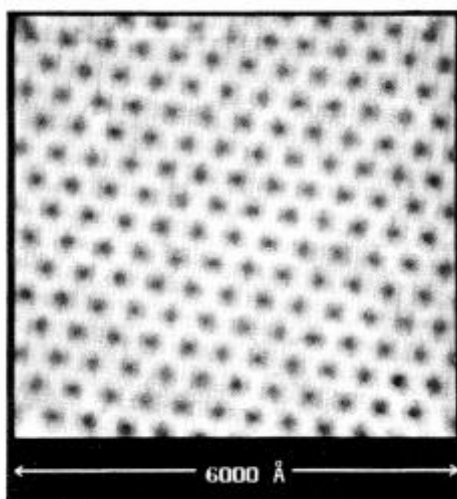


Figure 1.8: An Abrikosov flux line lattice of $NbSe_2$ at 1.8 K under a 1 T magnetic field. The figure was experimentally observed using a scanning tunnelling microscope [16].

The problem of the zero critical current of pure type-II superconductors can be solved by having defects inside the material. The defects are able to “trap” the vortices inside them, providing a counterforce to balance the Lorenz force, F_l , experienced by the

vortices so that vortex motion can be prevented. The defects which help to form the magnetic gradient are defined as “pinning centres”. The force that the defects exert on the vortices is known as the “pinning force”, F_p , and its function of enabling nonzero critical currents in type-II superconductors is called “flux pinning”. There are many types of defects capable of acting as pinning centres, such as inhomogeneities in the material, atomic defects within the crystal lattice, non-superconducting particles, and grain boundary dislocations [17]. Figure 1.9 provides an illustration of the defects which have been proposed as flux pinning sites in YBCO thin films.

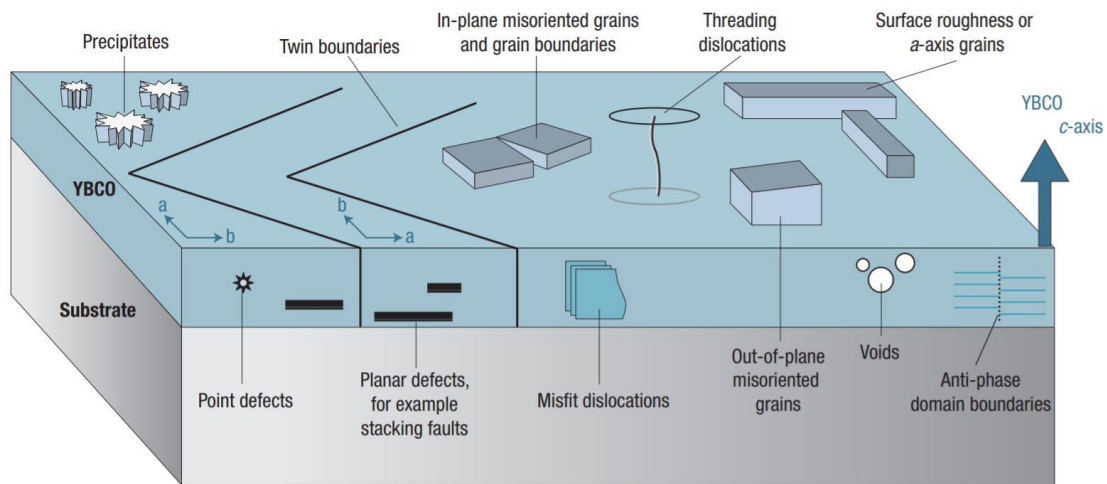


Figure 1.9: Illustration of defects proposed as flux pinning sites in YBCO thin films [18].

A pinning centre can prevent the movement of vortices and the dissipation of energy as long as the pinning force, F_p , is higher than F_l . Otherwise, the Lorentz force pushes the vortices out of the pinning centres. Hence, the critical state is $F_p = F_l$. Since the expression of F_l is:

$$F_l = J \times B \quad (1.5)$$

the critical current density of the superconductor, J_c , can be defined as:

$$J_c = \frac{F_p}{B} \quad (1.6)$$

According to Equation 1.6, the conceptual definition of critical current density refers to the condition that the magnitude of J_c is just high enough to induce a Lorentz force equal to the maximum available pinning force. Hence, for a type-II superconductor at fixed temperature and magnetic field, the critical current density is directly proportional to the pinning force. Normally, the determination of J_c using this pinning force definition is rather difficult. So, for practical applications, the critical current density of a superconductor is defined as the value at which a voltage drop of $10^{-4}V/m$ can be measured. This is a judicious choice of criterion to determine J_c , since at this point the flux motion is just about to begin.

1.4 Critical state models

Based on experimental observations of the macroscopic behaviour of type-II superconductors, several critical state models have been developed as straight forward approaches for better understanding their engineering applications. The simplest and most widely applied class of models is employed to calculate the current and field distributions of superconductors under different conditions.

The term “*critical state*” is used since it is assumed that the magnetic gradient from the outer to the inner layers of a type-II superconductor is always equal to the critical current density, J_c . When a magnetic field stronger than the lower critical field, H_{c1} , is applied to a superconductor, the critical state appears due to shielding effects of the flux vortices with the circulating current. After entering the material, the vortices become trapped by defects in the sample, and the penetration depth depends on the intensity of the applied field. The superconducting material within the penetration depth is in a critical state and carries a superconducting current, while the interior region without flux is considered to be in a “*virgin state*” which still retains zero current.

Out of all the critical state models that have been developed, this section focuses on those used in this thesis. The first to be introduced is the Bean model, proposed by C. P. Bean [19, 20]. It assumes a constant and uniformly distributed critical current density over the entire material, and can be used for intuitive estimation of the magnetisation of regular shape type-II superconductors. The next discussion is about the Kim model, proposed by Y. B. Kim [21, 22], in which the critical current is defined as magnetic field dependent. The Kim model allows for more precise prediction of material magnetisation.

1.4.1 The Bean model

The Bean model is the simplest among all the critical-state models. Two assumptions are made as preconditions:

- i. The magnetic field has no influence on the critical current density, J_c .
- ii. In the areas of the superconductor in the *critical state*, no current flows; in the areas in the *virgin state*, the current density equals J_c :

$$\begin{aligned} J(x) &= \pm J_c && \text{if } |E(x)| \neq 0 \\ J(x) &= 0 && \text{if } |E(x)| = 0 \end{aligned} \quad (1.7)$$

Equation 1.7 indicates that, in the Bean model, the current flowing through superconductors can only take values of $\pm J_c$ or 0. It can be illustrated using a superconducting slab of infinite length in the y-z plane, as shown in Figure 1.10. A uniform magnetic field is applied in the z direction, which induces a screening current flowing in a circular path along the surface of the slab. Since the y-z plane of the slab is assumed to be infinitely long, the current path in the x direction can be neglected compared to that along the y axis. Therefore, the current is assumed to flow solely in the y direction.

Under the influence of the external magnetic field, H_a , a shielding current is induced at the edges of the slab, which sets up a magnetic field in the opposite direction of the applied field, so that the applied field can be cancelled. When the external field is low, it cannot penetrate to the centre of the material, hence the interior of the superconductor remains current free (see Figure 1.10a). The gradient of the field inside the slab is a constant equal to:

$$\frac{\partial H_y}{\partial H_x} = \pm J_c \quad (1.8)$$

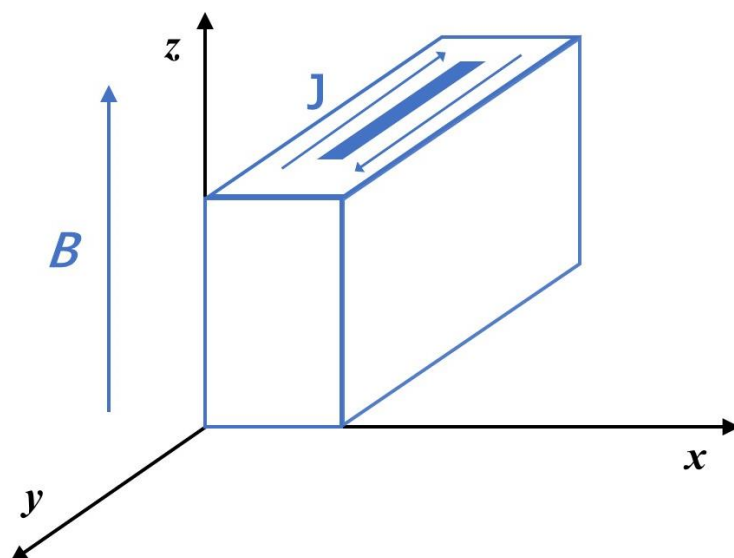


Figure 1.10: A superconducting slab with infinite length in the y - z plane. A magnetic field is applied in the z direction.

When the magnetic field increases to a certain point, it fully penetrates the superconductor and induces a current density $\pm J_c$ in the entire slab, as shown in Figure 1.10b. This value of external field is defined as the penetration field, denoted by H_p . With a further rise of H_a , the magnetic field penetrating into the slab sees an upward shift since the magnitude of the shielding current cannot exceed the critical current

density, J_c (see Figure 1.10c). Moreover, because the shielding current remains the same as in the $H_a = H_p$ case, the profile of the penetrated field also stays unchanged.

Figure 1.11d illustrates the situation in which the applied field decreases from the magnitude of H_m ($H_m > 2H_p$). Following Lenz's law, an inverted screening current appears at the surface of the superconducting slab and propagates towards the interior. With the external magnetic field dropping by $2H_p$ from H_m , the lowest point of the penetrated field in the previous case, $H_m - H_p$, becomes the new peak value. In addition, as shown in Figure 1.11e, the shape of the penetrated field and the direction of the shielding current completely reverse. Finally, if the applied field begins to increase again, a shielding current with reversed direction appears at the edges, accordingly (see Figure 1.11f).

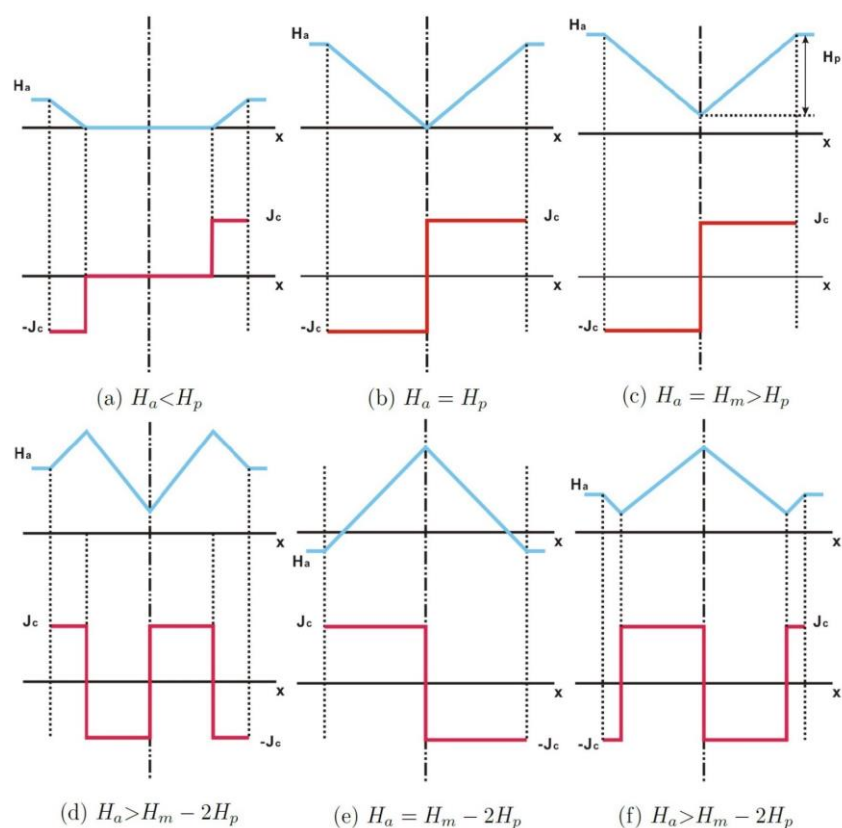


Figure 1.11: Further demonstration of the field-current characteristics of the Bean model: the relationship between the induced screening current and variation in the applied magnetic field.

Other than estimating the magnetisation of an infinitely long superconducting rod or a superconducting slab with infinite width, the Bean model is also capable of estimating the magnetisation and AC losses inside superconducting wires [22]. In summary, the Bean model is an elegant and powerful tool for explaining general magnetic and magnetisation behaviours inside type-II superconductors.

1.4.2 The Kim model

The Bean model assumes that the critical current density of superconducting materials remains unchanged regardless of external conditions. This approximation significantly simplifies the study of the magnetization characteristics of type-II superconductors. However, the accuracy is compromised since the critical current can be influenced by both the magnetic field and the temperature. In order to achieve more precise estimates, Kim, Hempstead and Strand improved the Bean model by introducing the magnetic field and temperature dependence of the critical current [22], to create the Kim model. The critical current thus becomes a local variable instead of a constant over the entire superconductor:

$$J_c(B) = \frac{\alpha(T)}{B_0 + B} = J_{c0}(T) \frac{1}{1 + \frac{B}{B_0}} \quad (1.9)$$

where B_0 is a constant dependent on the material properties, and $J_{c0}(T) = \alpha(T)/B_0$.

The temperature dependence of α was also proposed, which can be expressed as:

$$\alpha = \frac{1}{d}(a - bT) \quad (1.10)$$

where the constant, d , is related to the physical microstructure of the superconductor, and $\frac{a}{b} \leq T_c$.

1.5 Flux creep, flux flow and the Exponential E–J constitutive law

In both the Bean model and the Kim model, the Abrikosov flux line lattice is assumed to be very stable, and cannot be disturbed by thermal activation. However, this assumption doesn't hold as long as $T > 0 K$. As demonstrated in Section 1.3, when the current carried by a superconductor is smaller than its critical current, the FLL is stably formed by the pinning force. However, the vortices still can possibly escape the pinning centres under the influence of thermal activation. This process is known as “*flux creep*” [23]. For cases in which $J > J_c$, the Lorentz force becomes high enough that the pinning force can no longer hold the FLL inside the pinning centres. This movement of the FLL is called “*flux flow*” [24]. Hence, the current characteristics of type-II superconductor can be described by Figure 1.12.

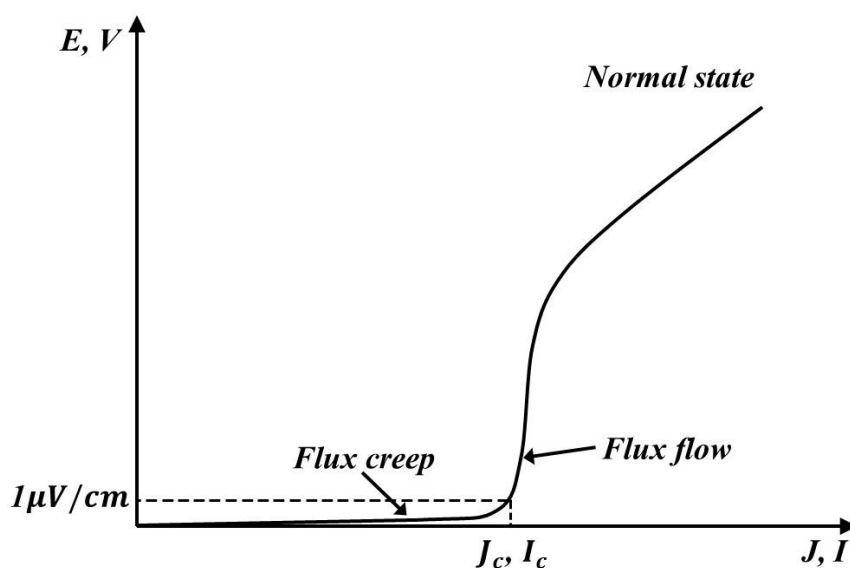


Figure 1.12: Current characteristics of type-II superconductors: flux creep state, flux flow state and normal state.

The theory of thermally activated flux creep proposes that vortices could be depinned from the minimum potential position by random thermal forces, with an escape rate, R , determined by the Boltzmann factor:

$$R = v_0 e^{-\frac{U}{kT}} \quad (1.11)$$

where U is the height of the activation barrier, and v_0 describes a microscopic attempt frequency, typically in the order of $10^{-8} \sim 10^{-10}/s$. k represents the Boltzmann constant, and T stands for the absolute temperature. The effective height of the activation barrier tilts with the rise of current, as can be seen in Figure 1.13, which indicates that the probability for the vortex to escape the barrier from one side gradually becomes higher than from the other.

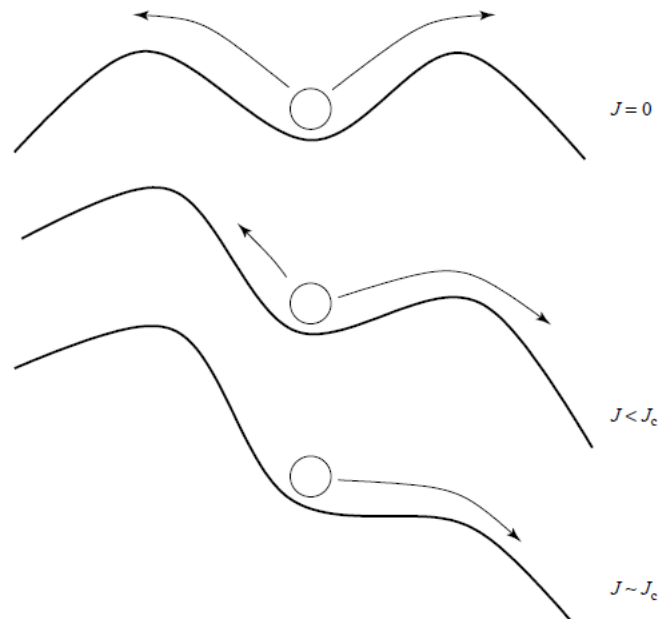


Figure 1.13: The energy landscape of a pinned vortex under a uniform external current.

Since movement of the vortices leads to an electric field according to the Lorentz transformation, it can be derived from the flux creep theory that the relationship continues between the current and the electric field in the superconductor. This exposes

another inaccurate assumption of the critical state model, because both models assume a step relation between E and J . Several expressions to describe $E - J$ characteristics have been proposed [25-28], among which the most commonly used model for practical simulations is the $E - J$ power law:

$$E = E_0 \left(\frac{J}{J_0(B)} \right)^n \quad (1.12)$$

where n is a parameter that shows the stiffness of the $E - J$ relationship. The value of n is determined by the properties and microstructure of the material. $J_0(B)$ is the measured critical current for a given electrical field, usually $E_0 = 10^{-4} V/m$.

In this model, instead of strictly propagating from the surface toward the centre of the superconductor with a constant current density, the current distribution becomes a consequence of the constitutive law. The $E - J$ power law agrees well with the experimental I-V curves of many type-II superconductors, partially due to its strong inclusivity. For $n = 1$, the law transforms into the linear Ohm's law ($\mathbf{E} = \rho \mathbf{J}$); for $n = \infty$, it corresponds to the Bean model. Moreover, $n = 5$ indicates that the material has strong flux creep, $n = 15$ describes weak flux creep, and $n = 50$ is the limitation between HTS and LTS superconductors [29]. The E-J relationship illustrated by the Bean model and the E-J power law model are shown in Figure 1.14.

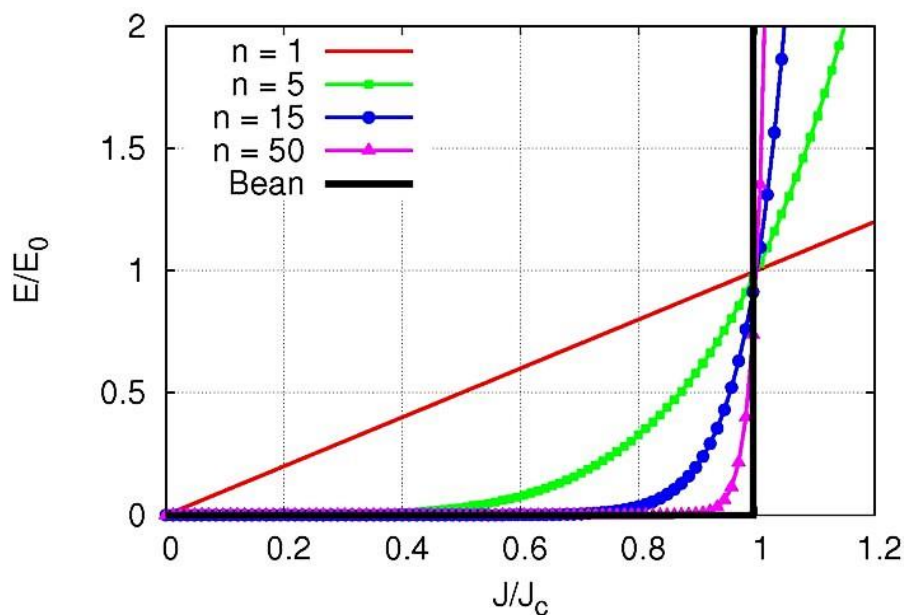


Figure 1.14: The E–J power law model with different n values. $n=1$ and $n=\infty$ correspond to the linear Ohm’s law and the Bean model, respectively.

1.6 Conclusions

This chapter introduced the fundamental knowledge of superconductivity. It began with the discovery and basic properties of superconductors. In brief, the most important features of superconductivity are ideal conductivity and perfect diamagnetism. Superconducting materials can be categorized into LTS and HTS superconductors according to their critical temperature. Type-I and type-II superconductors were defined based on their behaviour under a magnetic field. Since the study in this thesis is focused on type-II superconductors, the most important characteristics and theories of type-II superconductors were presented, including flux pinning, flux creep, flux flow theories, the critical state models, and the exponential E–J constitutive law.

Chapter 2

Background of the application of Resistive-type Superconducting Fault Current Limiters (RSFCLs)

With the rapid increase in electrical loads, a considerable percentage of global power systems have been stretched to their designed capacity, leading to a sharp rise in the fault current. Moreover, distributed generation and clean energy sources, such as wind and solar, being added to the already overburdened systems have also caused an increase in the fault current level. High fault current levels have severe impact on power systems. They can increase the likelihood of overcurrent damage, which may destroy electrical facilities or even cause system blackout [30-33]. The superconducting fault current limiter (SFCL) is a device that can help to mitigate the increasing level of fault currents [34, 35]. It can also contribute to the performance, stability and efficiency of electricity grids. This chapter introduces the problems of high fault current levels, the traditional system protecting schemes, and the necessity of applying superconducting fault current limiters.

2.1 Problems of high fault current levels

Nowadays, lifestyle quality in most cities across the world depends upon a reliable supply of electrical power. The electrical power required by domestic loads and industrial loads is typically transmitted via transmission systems and distribution systems. The majority of distribution systems operate in a radial topology, in which the customer loads are fed by upstream power sources. Power grid topology and diverse protection schemes have been studied in the past as the grid developed. However, over

the last few years, a considerable number of generation systems have been added to the existing power system, leading to a tremendous rise in fault current levels, which represents a serious threat to the stability and security of distribution networks.

Since increasingly more renewable generation systems are being integrated into the already overburdened UK distribution network, different parts of the power systems which have different voltage levels will all be affected (see below) [36], for instance:

1. Dense urban 11 kV and 33 kV distribution networks in which the designed capacities are nearly reached by existing equipment.
2. Isolated 132 kV substations which connect large-scale distributed generation and rural networks.
3. Isolated low voltage (LV) substations with deep penetration of distributed generation.

The continuous rise of fault current levels does not only occur in the UK, Europe and America. It is also an issue of concern for developing countries with rapid economic growth, like China. For instance, with the present construction of the Ultra-High Voltage (UHV) grid in China, the short-circuit current level of the 500 kV, 220 kV and 10 kV substations in some high load cities have exceeded 63 kA, which is the maximum interrupting capacity for existing circuit breakers [37]. In Guangdong Province, the three-phase short circuit current at one 230 kV substation reached 87 kA in 2010, and more than 40 substations there have experienced fault current levels beyond 59.9 kA. Furthermore, in 2015, the maximum level for the fault current increased to 105 kA [38], which is motivation to reconsider the currently used strategies for protection of the distribution and transmission systems.

2.2 Review of Protection Strategies for the Transmission and Distribution Systems

Regardless of the fault cause, fault currents have effects on the performance and reliability of the power system which cannot be underestimated.

It is well known that protection systems play a crucial role in the difficult task of delivering electric power. Failure of these protection systems may affect the safety, reliability, and efficiency of the overall power system and its capacity to deliver electricity. Among all the techniques of fault management [39], fault location, fault prediction, and fault protection are the most important aspects to be considered.

2.2.1 Fault location technologies

Several decades ago, identification of the fault location was performed by visual inspection of the transmission line. As the first fault location method, this technique requires no sophisticated equipment and is relatively effective, but severe economic losses can be attained if the fault location is not identified quickly. In the 1970s, Takagi *et al.* [40] proposed single-ended fault location methods, which use Intelligent Electronic Devices (IEDs) to identify the location of a single line-to-ground fault based on the reflective properties of transmission lines. Another new technique called synchronized phasor measurement was introduced in the mid-1980s [41]. This method requires two phasor measurement units (PMU), which were invented by Virginia Tech in 1988, being placed at both ends of a very long transmission line. In order to achieve very accurate time keeping, these two PMUs are synchronized to a GPS satellite. The three-phase phasors of voltage and current simultaneously measured by the PMUs are tagged with an external reference clock signal, and then sent to the relays at the other ends of the protected line through a communication channel. Fault direction

discrimination, fault-type identification and fault location can be confirmed through calculation of pre-defined algorithms using this data [42]. The protection scheme of synchronized phasor measurement is illustrated in Figure 2.1.

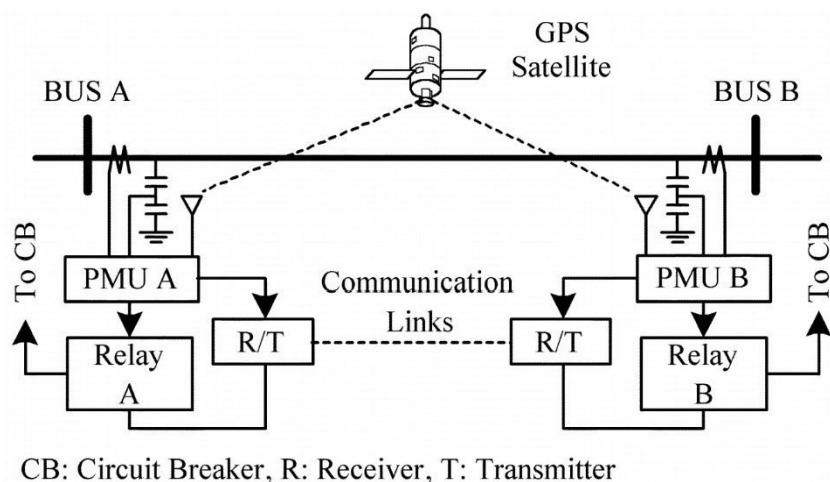


Figure 2.1: Diagram of the phasor measurement units (PMU) fault location method [42].

2.2.2 Fault prediction technologies

Fault prediction techniques aim to detect a failure in power system components early enough to allow the suspected component to be maintained or replaced before a catastrophic fault occurs. This technology is mainly composed of early fault detection (EFD) techniques, data mining, and exploration of hidden failures [43-45].

A considerable portion of EFD research focuses on the early detection of damaged components of power equipment such as transformers, insulators, and fault arresters, through thermal analysis and other non-invasive technologies. In other words, EFD is an early warning fault prevention method. It benefits from microprocessor based controls and automation, as well as instrumentation capable of capturing and monitoring the current, voltage, and thermal states of some important components in the power networks, e.g. the transformers and the switchgear, and then to identify whether a potential fault is about to occur when minor changes are detected.

However, due to the complexity and massive amount of recorded data, faults cannot be easily identified at an early stage. Fortunately, with the rapid development of high speed communications and storage media technology, nowadays it is possible to establish comprehensive power system operational databases, leading to the possibility of distinguishing potential transmission and distribution faults through statistical data mining approaches [46].

However, because of the existence of hidden failures, it is impossible to guarantee the safety and reliability of the power system even if all faults can be predicted or detected. Hidden failure refers to the fact that the relay may have an undetected defect that remains dormant until abnormal operating conditions are reached [47]. It is undetectable during normal operation but will be exposed as a direct consequence of other system disturbances which might cause a relay system to incorrectly and inappropriately disconnect the circuit element(s). Hidden failures have been identified as key factors for power system cascading failures. In fact, major disturbances have shown that hidden failures are involved in over 70% of the studied blackouts [48]. It is difficult to model hidden failures with high accuracy because of its complex origin. Nevertheless, plenty of approximation models have been proposed to study how to reduce hidden failure probabilities whilst increasing the system reliability [45, 49-51].

2.2.3 Fault protection technologies

Compared to fault prediction techniques, fault protection is a more mature technology. This technology has progressed dramatically since Thomas Edison proposed the idea of the circuit breaker in 1879 [52], whose idea is still of great importance to modern grid protection strategies. Plenty of advanced equipment and techniques have been invented along with the development of power systems, such as distributed automation, detecting high impedance faults, and fault current limiters. Current commercial applications of automated functions such as Fault Location

Isolation, Service Restoration, Volt/Var Control, Optimal Feeder Reconfiguration, and Relay Protection Re-coordination have all made the power grids smarter and more reliable.

2.3 Brief Introduction to the Circuit Breaker Concept

2.3.1 The operating principle of circuit breakers

As one of the most important roles among all fault protection devices, the circuit breaker (CB) is supposed to detect a fault condition, and then interrupt the current flow with the cooperation of other equipment such as an over-current relay.

Under short-circuit conditions, the calculated maximum prospective short circuit current may be many times higher than the rated current of the circuit. When electrical contacts open to interrupt a large current, there is a tendency for an arc to form between the opened contacts, which allows the current to continue.

To be more specific, when the current passes through a natural zero at each half-cycle, the arc carrying the current goes out momentarily. However, due to the voltage which immediately reappears across the open contacts of the circuit breaker, the arc ‘restrikes’ and will continue to carry current for the next half-cycle until the next current zero, where it goes out again and the process repeats [53]. This is shown in Figure 2.2.

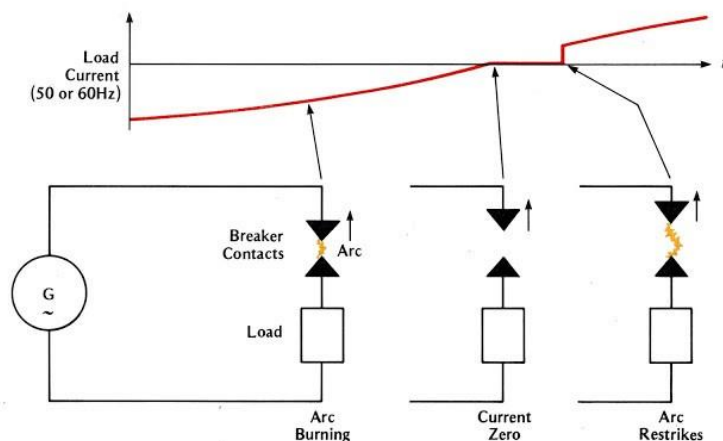


Figure 2.2: The principle and procedure of AC Current Breaking. The arc can restrike after action of the breaker if the voltage is high enough.

As the open contacts continue to separate, the arc path, i.e., the distance between these two open contacts, increase. At some point, when the current passes a natural zero, the arc path becomes too long that the voltage cannot breakdown anymore, which means the arc cannot restrike again, and the fault current is interrupted [53].

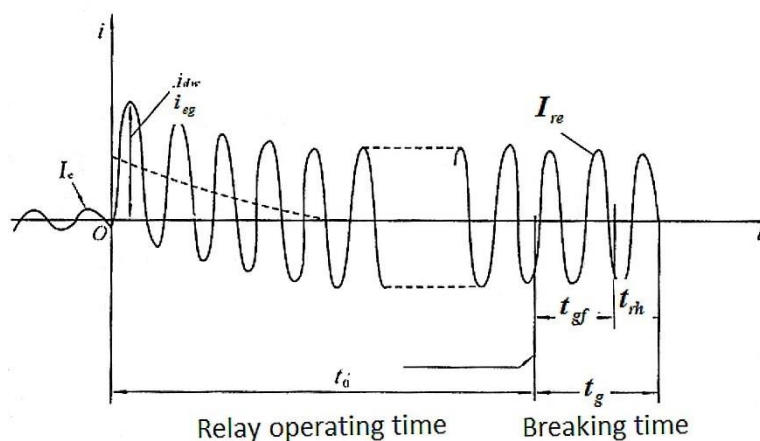


Figure 2.3: The current waveform and total time between the start and clearance of a fault. The time required to cut the fault is composed of the relay operating time and breaking time.

In Figure 2.3, the breaking process is summarized in two stages. The first is the relay operating time, i.e., before reaching the relay protection time, t_0 . The second is defined

by the AC breaker breaking time, t_g , where t_{gf} is the action time of the AC breaker and t_{rh} is the time of the burning arc.

2.3.2 Types of circuit breakers

Circuit breakers are categorized by the medium and the method used for interruption of the current. The following 5 types of circuit breaker are generally the most widely used ones.

1. Oil circuit breakers

Oil circuit breakers (OCB) are rarely used for offshore grids, but are very common in onshore installations. An oil circuit-breaker consists of a set of breaking contacts, totally immersed in oil for each one of the phases, either in a common tank or in three separate tanks. A mechanism, which may be mechanical, hydraulic or pneumatic, drives all the moving contacts simultaneously, in order to close the circuit.

The interruption process is based on the creation of hydrogen and acetylene gas bubbles, as the oil decomposes as a result of the arc established between the switching contacts. The disadvantages of using oil as a quenching medium in a circuit breaker are its flammability and high maintenance costs, which forces the search for alternative quenching media [54].

2. Air circuit breakers

Air-break circuit breakers (ACB) operate with their contacts in free air. However, their method of arc control is entirely different from that of oil circuit-breakers. In this case, arc control depends on the suppression of the re-striking voltage, which gives the ACB very different performance characteristics. ACB are always used for low-voltage

interruption and now tend to replace high-voltage oil breakers up to 11 kV and even higher. HV circuit-breakers on most offshore installations are in fact ACBs [55].

3. Vacuum circuit breakers

Vacuum circuit-breakers (VCB) are becoming increasingly popular, especially for medium ranges of voltage grids, due to their excellent performance and compactness. Their operating principle differs from OCBs and ACBs. VCBs operate by providing no medium in which for the arc to reform [56], whereas the OCB functions by flushing out the ‘combustion’ products of the arc, and the ACB by suppressing the re-striking voltage wave.

4. SF6 circuit breakers

SF6 circuit breakers use sulphur hexafluoride as an alternative for oil. The advantages of using this substance as an insulating and interrupting medium come from its high dielectric strength and outstanding arc-quenching properties. SF6 circuit-breakers are much smaller than air-break circuit-breakers of the same rating, and the dielectric strength of the SF6 under standard atmospheric pressure is equal to that of air at ten atmospheres. However, the decomposition products of SF6 discharged as a gas following extinction of the very hot arcs are harmful to the environment, and also contain a small amount of fluorine which may react with metallic parts of the breaker [57].

5. Air-blast circuit-breakers

Air-blast circuit-breakers are widely used for onshore grids, but they are confined to extra high voltage and high breaking capacity transmission systems. This type of CBs operates similarly to OCBs, except that the arc products are forced away by the release of compressed air rather than by oil [58].

2.3.3 Disadvantages of circuit breakers

Circuit breakers are quite mature devices that have been significantly improved over the last century. They are necessary components of any protection system, but they should be the last resort of the protection schemes. In fact, the limitations and unwanted side effects of CBs are becoming more serious with the development of modern power systems. For instance, circuit breakers usually operate after 2–4 cycles of a fault current in an attempt to limit both the magnetic and the thermal effects of a fault [59]. However, the first fault current peak tends to be the highest, which may cause serious damage to equipment due to mechanical stresses from electro-magnetic interactions [60]. Furthermore, it is well known that continuity of supply has long been the Holy Grail for power engineers, and circuit breakers will always interrupt this supply when operated.

In addition, fuses which are also extensively used in power systems, in conjunction with circuit breakers, must be physically replaced once burned out, which occasionally leads to longer periods of system interruption [61]. Moreover, they are only available for voltages below 35 kV.

As stated before, in some cases the circuit breakers within current manufacturing capability are not capable of clearing a short-circuit current due to insufficient maximum rating. Thus, studying fault protection strategies that can effectively limit the fault current level is of paramount importance, and new control schemes need to be developed in order to achieve safer and more reliable modern electric grids.

2.4 Optimal Fault Protection Scheme

Several strategies could be used to control the fault current level of the grid as shown in Table 2.1. However, the most common measures used today all suffer from certain

limitations. For instance, splitting of bus bars or separating large networks into smaller ones would require huge investment, and inserts permanent resistance into the system [62]. Choosing a higher transformer impedance would also cause an operating loss, and would decrease the power system stability as well. Furthermore, even though the so-called I_s -Limiter can achieve small impedance at nominal operation and fast increase of impedance at fault conditions, it has to be serviced after each trigger (just like fuses) and its scalability to high voltage levels is very limited [63].

Table 2.1: Different options to reduce short-circuit currents [34]. The methods were categorized based on two standards.

Permanent increase of impedance at nominal and fault conditions		Condition based increase of impedance: small impedance at nominal load, fast increase of impedance at fault	
Splitting into sub grids; Introducing a higher voltage range; Splitting of bus bars.	High impedance transformers; Current Limiting air core reactors.	High voltage fuses (<1 kA, <36 kV); I_s -Limiter, CLiP (<1 kA, <36 kV); FCL circuit breakers (< 1kV).	Novel Concepts Superconductors; Semiconductors; e.g. FACTS Hybrid systems.
Topological methods	Apparatus methods		

It would be desirable to have an efficient method to clamp fault currents to a level that is less harmful to the power system during the first peak of the fault current, as well as allowing the circuit breakers to act effectively when needed, or not at all if the fault current is fleeting or temporary.

For this purpose, the novel idea of a superconducting fault current limiter (SFCL) is proposed based on this characteristic of HTS. The quench characteristics of high temperature superconductors (HTS) offer the possibility of limiting fault currents without changing the normal operation of the grid [64]. To be more specific, superconducting materials can carry a large amount of current with near-zero resistivity in the superconductivity state, but when the temperature exceeds the critical temperature of the superconductor, a so-called quench takes place, i.e., the superconducting state disappears, resulting in a rapid increase of electrical resistivity [65]. This rapid transition from near-zero resistivity to high resistivity, which can occur in less than a cycle if so desired, inserts a considerable resistance into the system at the opportune time and thereby limits the fault currents [66].

Another outstanding advantage that the SFCL holds is that, unlike devices like fuses or I_s -Limiters, the SFCL can be automatically reset after the fault has been cleared [67]. Moreover, the maintenance costs of the 2G HTS SFCL system are relatively low once the setup is finished, and therefore, high running costs can be avoided, such as in the case of powered electronic devices.

Hence, based on the state of the art of fault protection technologies and the increasingly higher grid requirements, the SFCL as a prospect is very promising. SFCL will find more and more applications in modern power grids due to its fast response, quick and automatic recovery, excellent current limiting performance, and low maintenance costs.

2.5 Ideal Superconducting Fault Current Limiter Characteristics

A superconducting fault current limiter is a revolutionary power system device developed to deal with the increasing incidence and level of fault currents. It can

improve the performance, stability, and efficiency of electricity grids. As explained in Section 2.4, with its capability to rapidly increase the impedance, a superconducting fault current limiter can mitigate prospective fault currents to a lower manageable level. Moreover, thanks to their fast transition from a low to a high impedance, as well as their automatic resetting ability after clearance of system faults, a superconducting device can limit, in a very short time, the value of any fault current [68].

The main features that an ideal SFCL should achieve are listed below [69-72]:

- 1) Virtually zero impedance during rated operation of the power system (low AC loss).
- 2) Ability to reduce the fault current to a desirable percentage before the first peak.
- 3) Capable of repeated operation for multiple faults in a short period of time.
- 4) Quick and automatic recovery.
- 5) Sufficient capacity to mitigate the high fault currents in a modern power system.
- 6) No negative influence on the normal operation of relays and circuit breakers.
- 7) Compact, light-weight and low maintenance costs.

In reality, one would like to have an SFCL that satisfies all of the aforementioned features, however, certain trade-offs and compromises have to be made in nearly all categories and types of SFCLs.

2.6 Types of Superconducting Fault Current Limiters

SFCLs can be divided into several categories according to their different structures, such as resistive type SFCLs, shielded iron core type SFCLs, DC biased iron core type SFCLs, transformer type SFCLs, fault current controlled type SFCLs, and bridge type SFCLs. However, essentially, all the aforementioned SFCLs can be included into three basic design methodologies based on their operating principles for limiting the fault currents. Those are:

- i. **Resistive type SFCL:** This is the simplest of the three methods. The superconductor is placed in series with the grid, usually in the form of a non-inductively wound coil. When a fault occurs, the temperature of the superconductor rises and the thermal energy accumulated inside the superconductor leads to its quenching. It then resets once the electric current is limited. There are many examples of this type of SFCL, such as the one built during the ECCOFLOW project which was installed in Kosice, Slovakia [73].
- ii. **Inductive type SFCL:** This method involves the use of an iron core with a superconducting coil wrapped around it. During normal operation, the coil acts as a barrier to the magnetic flux and prevents the primary and the secondary from being linked. Under fault conditions the flux produced by the primary rises sufficiently to drive the superconducting coil to the normal state. This enables the magnetic circuit to be completed and the impedance to rise. An example of this design is the Areva/Bruker design installed at Augsburg [74].
- iii. **Saturated Core SFCL:** This method involves pre-saturating an iron core with a superconducting DC coil. When a fault occurs, the core is driven out of saturation. This leads to an increase in impedance and limitation of the current. An example

of this design is the one being currently tested by substation as part of a project sponsored by ETI [75].

Despite multiple concepts for SFCL designs being conceived in the last two decades, resistive-type SFCLs are the most promising due to their potential to be smaller, and the expected decrease in prices for 2G coated conductors [76]. Thus, in this project we focus on the integration of resistive-type SFCLs into simplified power system models in order to explore their behavior inside real power grids.

2.7 Operating Principle of the RSFCL

Due to their structural characteristics, resistive-type superconducting fault current limiters can be built very compact and light compared to other types of SFCLs. The electrical circuit of an RSFCL is shown in Figure 2.4.

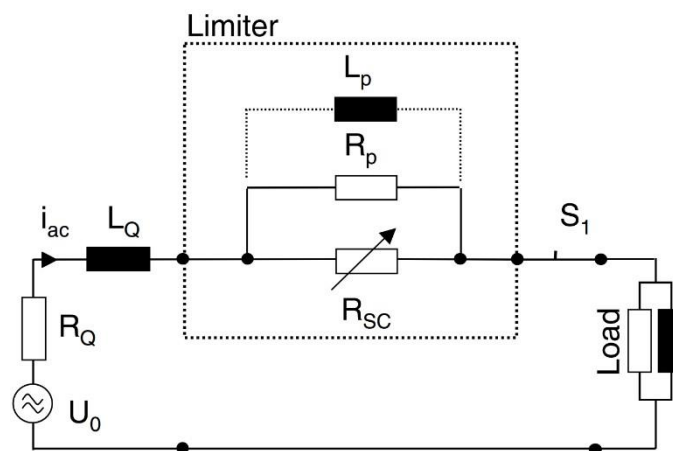


Figure 2.4: Electrical Circuit of an RSFCL. The impedance R_p and L_p stands for the shunt impedance of the RSFCL.

The resistance of the superconductor as represented by the variable resistance, R_{sc} , in Figure 2.4 is zero under D.C. conditions, while under A.C. conditions there is a small AC loss during normal operation. The impedance increases rapidly after the current carried by the superconductor exceeds a certain critical current threshold. The

resistance, R_p , which is connected in parallel with R_{sc} , is the shunt resistance that is used to prevent the superconductor from being destroyed by hot spots during the quench. This shunt resistance, R_p , has to be in contact all over the length of the superconductor, R_{sc} , in order to achieve the desired protection. In addition, this parallel resistance can protect the superconductor from overvoltage, since the limited current can be adjusted by R_p if R_{sc} rises too rapidly. The switch, S_1 , clears out the short-circuit fault after the heat energy inside the SFCL reaches a pre-defined level, in order to control the temperature of the superconductor.

Due to the quench and the heating of the superconductor, a recovery time is needed before the SFCL can operate in the normal state again. The recovery time mainly depends on the design and properties of the superconducting material, and it usually ranges from several cycles to tens of cycles for 2G HTS tapes SFCL [77].

Instead of using a shunt resistance to suppress the negative influence of hot spots, another method has been proposed by Bock *et al* [78], which helps to suppress the occurrence of hot spots during the quench period by adding a normal conducting coil in parallel to the superconductor. This arrangement uses the fact that the superconductor's critical current can be affected by any external magnetic field. Thus, in the setup, a normal conducting coil is placed coaxially outside a superconducting tube. After the quench is initialized at the weakest point of the superconductor, the growing resistance, R_{sc} , forces the current to flow in the parallel coil. The coil induces a magnetic field which lowers the critical current in the remaining superconducting regions. Consequently, it magnetically assists the acceleration of the quench process and mitigates the hot-spot problem.

From the basic operational concept of an SFCL it can be seen that differences in physical characteristics do not affect the applicability of superconducting materials in SFCLs [34, 69]. However, accurate sizing of the amount of required material is a serious

challenge which depends on the properties of the superconductor and the power system. For instance, under the assumption that the superconductor heats up uniformly during a broad transition, for low J_c materials, the amount of required material can be roughly estimated by the magnitude of voltage the superconductor needs to carry after entering the normal state. For high J_c materials, the quantity is mainly determined by how much thermal energy the material can absorb without degradation. Also, the material volume still needs to be small enough that the SFCL can heat up to above T_c before reaching the actuation time of the circuit breaker.

Before the manufacturing of high temperature superconducting materials with reproducible quality, very successful projects were carried out using SFCLs using low temperature superconducting materials such as NbTi alloys [79, 80]. Nonetheless, despite the cost of NbTi alloys in the superconductivity market being very competitive, LTS SFCLs do not seem possible for commercial use due to the high cooling cost and the difficulties of managing a cryogenic system with a nearly zero helium loss. Since HTS SFCLs are intentionally designed to operate at liquid nitrogen temperature, they substantially reduce the cryogenic cost of the entire system.

2.8 Practical Implementation of HTS RSFCLs

HTS materials in diverse configurations such as bulks, thin films, or coated conductors have been extensively used for prototyping SFCL worldwide (Table 2.1 at the end of this chapter).

In 2003, the first field test of a the CURL10 SFCL for medium-voltage-level applications was built with melt cast processed Bi2212 tubes cut into bifilar coils, showing virtually no degradation of the material after two years of tests [81]. Using the same bulk material but cut into monofilar coils, the first commercial medium voltage SFCLs were released in 2009 by Nexans SuperConductors GmbH for two customers

[64]: Applied Superconductor Limited in UK, and Vattenfall in Germany. Most recently, an SFCL with a rated power of 4.4 MVA (11 kV, 0.4 kA) was installed in the UK in early 2012, and it has been operating since mid-2013 [82]. A novel concept of magnetic field assisted quench propagation was also developed in order to overcome the difficulties of scaling of the bifilar concept to high voltages, with a successful proof-of-concept test achieved in the United States in 2005 [83]. At the demonstration scale, other bulk geometries made of Bi2212 were tested in Switzerland reporting a medium voltage SFCL with a rated power of 6.4 MVA (8 kV, 0.8 kA) [84].

Bi2223/Ag multifilamentary tapes have also shown to be feasible for the prototyping of SFCLs, but commercial implementation of these devices has not been pursued. Two major research projects were conducted on the base of this material and small scale prototypes were successfully tested. The first was conducted in Brazil aiming for the design of an SFCL with a rated power of 6 MVA (15 kV, 0.4 kA), but only laboratory scale proofs for the validation of the Bi-2223/Ag concept were reported [85]. The other project of relevance was conducted in Italy for an SFCL with a rated power of 40 kVA (500 V, 80 A) [86].

Many HTS materials have also been studied in the past for the prototyping of SFCL at small scale with very promising results [87]. However, the most prominent alternatives have become YBCO coated conductors, also called the second generation (2G) of HTS. The wide application of YBCO materials was due to their larger cooling surface area (in contrast to the bulk volume ratio), better performance under electro-mechanical stress and thermal shocks induced by fault currents, as well as increased design flexibility for practical purposes.

Before the appearance of commercialized 2G HTS conductors, many efforts were made and continue to be made in order to determine the correct combination, sizing, deposition technique, and physical properties of the different materials composing this

kind of structure (HTS, substrate, buffer, etc.). Toward this purpose, research on SFCL also played a major role. One of the first successes of the concept proof for using YBCO thin films in SFCL was achieved by Siemens-Germany during the 1990s, where different deposition techniques and substrates were compared and tested for low, medium, and high voltage rated powers [88]. This was maybe the most successful project on the implementation and characterization of YBCO thin films for SFCLs at that time, although in the same period other important designs were also proposed by companies like Toshiba in Japan [89]. In the following decade most of the research on SFCL based YBCO thin films was mainly dominated by Japan [90-93] and Korea [94-96] by pursuing some novel designs.

The first successful proof-of-concept test of an SFCL based upon coated conductors was reported in 2003 by the European SUPERPOLI project [97]. In this project, YBCO coated stainless-steel tapes were fabricated for the design of three modules connected in series with minimum current limitation effect at 2.4 kA. It successfully operated (with no material degradation) at 20 kV for prospective short-circuit currents up to 50 kA. Other YBCO coated conductors with specific features were also tested for the same purposes in Germany [98]. Based on the experience acquired from these projects, different design concepts were further proposed for the use of commercial 2G HTS tapes [99]. Superpower Inc. was the first that showed the feasibility of using commercial tapes for manufacturing SFCL at low and high power grids [100]. Almost at the same time, in Korea, two different size coils made of American Superconductor (AMSC) tapes were successfully tested in an SFCL rated at (13.2 kV, 630 A), leading to the conceptual design of the SFCL rated at (22.9 kV, 630 A), which has operated in south-east Seoul since 2011 [101]. In Japan, a consortium formed by different companies and research institutes has successfully tested a (6.6 kV, 600 A) SFCL. During this project, the researchers optimized the thickness of the silver protecting layer of the AMSC tape, and laminated it with a high-resistive stabilizing metal layer [102].

In the same year, AMSC, Nexans, Siemens, and Los Alamos National Laboratory, reported the successful test of a (138 kV, 1.2 kA) SFCL installed in the Southern California Edison Grid as part of the DOE project called Superlimiter [103]. Continuation of this project was granted by the DOE (DE-FC26-07NT43243) in 2009 [104], but the final project report has not been yet released. In China, Shanghai Jiaotong University has manufactured their own 2G HTS tapes for the testing of a (10 kV, 200 A) SFCL-concept in 2012 [77], and with the experience they are currently pursuing studies into the physical properties and performance of their own tapes compared with the ones provided by AMSC for the prototyping of SFCL in DC systems [105]. The German government funded project called ENSYSTROB, has installed the world's largest SFCL on the base of 2G HTS conductors in the Boxberg grid, successfully operating with a medium voltage rated power of 6.4 MVA (12 kV, 533 A) [106]. During the recently ended European project ECCOFLOW [107], a (24 kV, 1 kA) SFCL was designed to meet the specific requirements of two hosting utilities, Endesa in Spain, and VSE in Slovakia, but the testing results have not been yet disclosed.

Finally, it is worth mentioning that despite the number of projects on SFCL based on MgB₂ wires being smaller [108-110], their low manufacturing cost featuring high n -values furthers the possibility of using liquid hydrogen as conductive-coolant [111], which makes MgB₂ wires highly attractive for the prospective commercial deployment of this technology.

Table 2.2: Current status of the RSFCLs that have already been field-tested over the world.

Material	Data	Year / Ref. ^a	Country / Lead Company
NbTi	6.6 kV, 1.5 kA	1993 / [80]	JPN / Toshiba
NbTi/CuNi	40 kV, 315 A	1996 / [79]	FRA / Alsthom
Bi2212	6.9 kV, 600 A	2003 / [81]	DEU / ACCEL - Nexans
Bi2212	8.6 kV, 800 A	2005 / [83]	USA / DOE - EPRI
Bi2212	12 kV, 100 A	2009 / [64]	GB - DEU / Nexans / ASL
Bi2212	12 kV, 800 A	2009 / [64]	GB - DEU / Nexans / ASL
Bi2212	11 kV, 400 A	2012 / [82]	GB / ASL
Bi2223	500 V, 80 A	2005 / [86]	ITA / CESI
YBCO*	765 V, 135 A	1999 / [88]	DEU / Siemens
YBCO*	200 V, 1kA	2004 / [112]	JPN / Mitsubishi
YBCO*	6.6 kV, 200 A	2005 / [95]	KOR/ KEPRI
2G HTS	20 kV, 2 kA	2003 / [97]	EU / Superpoli project
2G HTS	6.6 kV, 600 A	2009 / [102]	JPN / Toshiba
2G HTS	138 kV, 1.2 kA	2009 / [103]	USA / IGC-Superpower
2G HTS	22.9 kV, 630 A	2012 / [101]	KOR / KEPRI
2G HTS	10 kV, 200 A	2012 / [77]	CHN / Shanghai Jiaotong Uni.
2G HTS	12 kV, 533 A	2012 / [106]	DEU / Ensystrob project
2G HTS	24 kV, 1kA	2013 / [107]	EU / Eccoflow project

Chapter 3

Preliminary Study of Simulation of RSFCLs in the Power System

This Chapter presents a power system model built with interconnected Distributed Generation (DG), including transient analysis of the system with and without short-circuit faults. The design and the working principle of a step-resistance SFCL model is illustrated and explained. In order to give a clear overview of the important role that an SFCL plays in a power grid, the current limiting behaviour of the designed SFCL module is demonstrated through its integration into the power system model. Finally, based on simulation results of the SFCLs' performance at different locations in the system, the optimal location of the SFCL for protecting the entire system is identified.

3.1 A Power System with Grid-Connected Wind Farm

To achieve sustainability and reduce CO₂ emissions, renewable energy generation has been growing rapidly over the last decade, especially for the development of wind plants. For instance, wind power supplied 5.3% on average of the UK's electricity demand in December 2011, reaching a record share of 12.2% on 28th December. Furthermore, the Chinese government has set a target that at least 12% of electrical energy must be provided from renewable sources by 2020, where the total installed grid-connected wind capacity in China should be about 30 GW [113]. Thus, based on this figure, it is clear that study of the behaviour of power systems when wind farms are connected is of great importance.

Whilst wind farms proliferate, the development of the grid network is being left behind, which leads to a series of challenges about how to integrate ever-increasing

wind power into the grid. This is of special concern in regions with rich wind sources but weak grid networking. As the connected generation capacity of the network grows, the short-circuit capacity also increases. In other words, by connecting wind farms, the wind turbines become extra current suppliers for the grid. When there is a short-circuit fault in the system, the short-circuit current or fault current will be much higher than the one that the grid network was initially constructed for. Thus, with wind farms connected to the system, serious faults can generate surge currents more than one hundred times the normal operating currents, resulting in damage to expensive grid-connected equipment.

In addition, the islanding issue caused by the direct connection of distributed generators to the power grid also needs to be taken into consideration. Islanding refers to the condition in which a DG continues to power a location even though electrical grid power from the electric utility is no longer present. Islanding can be dangerous to utility workers, who may not realize that a circuit is still powered, and it may prevent the automatic re-connection of devices. For this reason, DGs must detect the islanding condition and immediately stop the power production, which is known as anti-islanding [114].

As stated before, the SFCL has almost negligible resistance in the superconducting state during normal operation, and is capable of reducing the fault current level within the first cycle of the fault current [115]. Hence, an SFCL could offer powerful solution to control the fault current level, power quality, and islanding issues, when large scale wind farms are integrated into the power grids.

3.1.1 Modelling and parameters of the studied system

In order to determine whether the installation of an SFCL is needed for a specific power system, the short-circuit characteristics of the system need to be studied. Figure

3.1 shows the power system model with grid-connected wind power plant simulated in this chapter.

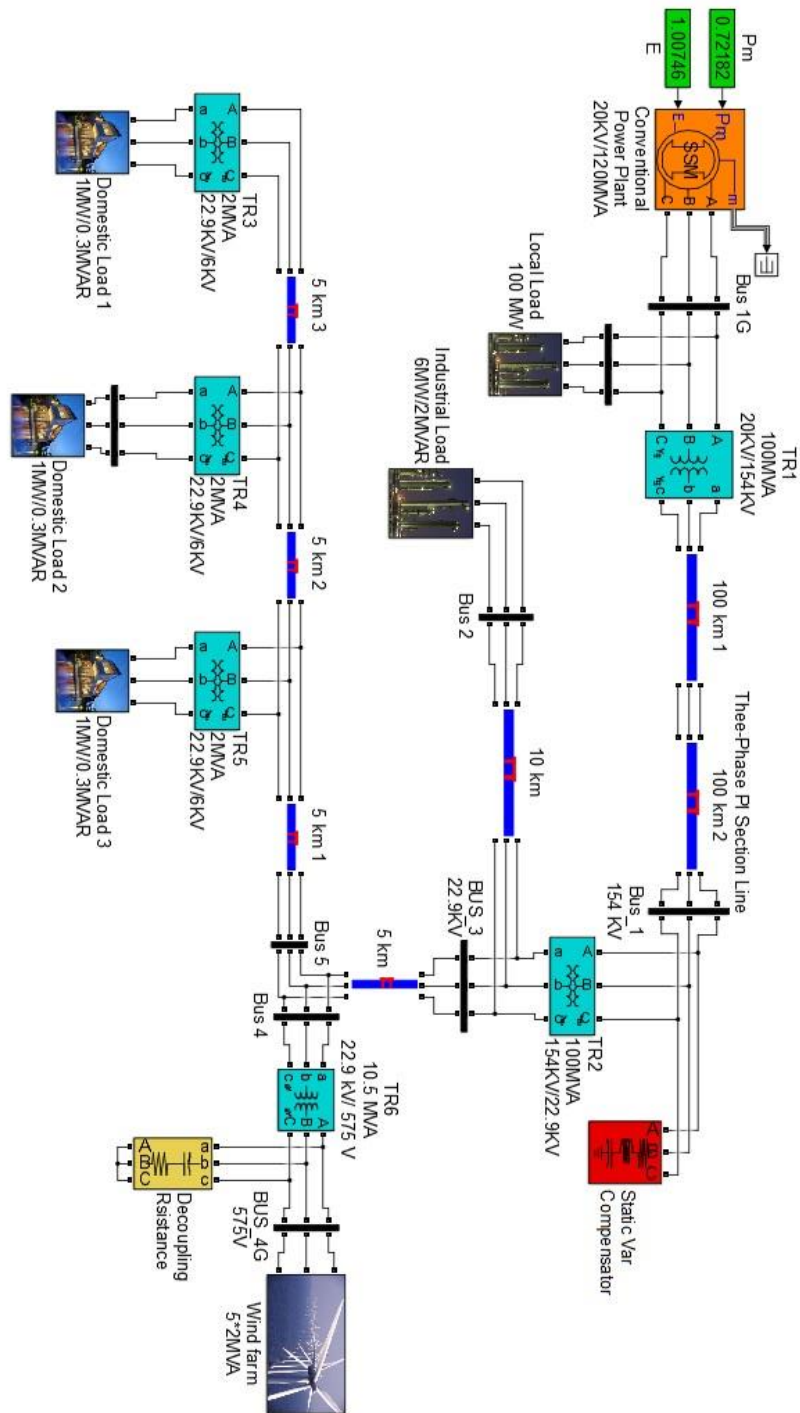


Figure 3.1: Model of the studied power system which has a grid-connected wind power plant.

The modelled power system is built based on the Korean electric transmission and distribution power system [116]. The power system is composed of a 120 MVA conventional power plant, modelled by a three-phase synchronous machine with rated line to line RMS voltage of 20 kV. This conventional power plant has a 100 MW local load, and then it is connected with 200 km long 154 kV three-phase π section transmission lines after a step-up transformer TR1. Next to the substation (TR2) where the voltage is stepped down to 22.9 kV from 154 kV, a static var compensator is installed to maintain the system voltage level. The substation TR2 has two separate distribution branch networks outwards, one connected to a high power industrial load (6 MW), and the other connected to 6 low power domestic loads (1 MW each). The 10 MVA wind farm is composed of five fixed-speed induction-type wind turbines that all have a rated power output of 2 MVA. It is connected to the domestic loads branch network via a step-up transformer (TR6) and moreover is capable of feeding the Industrial Load through 5 kilometres of overhead transmission line. In addition, since the wind turbines cannot be connected directly in series with the transformer TR6 (because the transformer can be seen as an inductive element), a high-value decoupling resistance (100 M Ω) is added in parallel with the wind farm block.

The detailed parameters of the transformers are not labelled in Figure 3.1 because of the space limitation. The parameters, which in agreement with the IEEE standards [26, 117], are listed in Table 3.1.

Table 3.1: Technical parameters of the transformers in the power system model.

Transformer No.	Nominal power and frequency Pn (VA), fn (Hz)	Winding 1 parameters V_{1,Ph-Ph} (Vrms), R1 (pu), L1 (pu)	Winding 2 parameters V_{2,Ph-Ph} (Vrms), R2 (pu) , L2 (pu)
TR1	100e6, 60	20000, 0.03, 0.11	154e3, 0.03, 0.11
TR2	100e6, 60	154e3, 0.02, 0.1	22.9e3, 0.02, 0.1
TR3&TR4&TR5	2e6, 60	22.9e3, 1e – 6, 0.025	6e3, 1e – 6, 0.025
TR6	10.5e6, 60	575,8e – 6, 0.0625	22.9e3, 8e – 6 , 0.0625

The initial state parameters of the three-phase synchronous machine, as well as the fixed-speed induction-type wind turbine, are modified from the integrated Matlab models which can be assessed through the Matlab commands “power_simplealt” and “power_wind_type_4_avg”, respectively. The parameters of the transmission lines for different voltage levels used in this project are listed in Table 3.2, where all the overhead lines parameters are based on the national standard given in [118].

Table 3.2: Technical parameters of the transmission lines in the power system model.

Voltage Levels	Positive- and zero-sequence resistances (Ω/km) [r1 r0]	Positive- and zero-sequence inductances (H/km) [l1 l0]	Positive- and zero-sequence capacitances (F/km) [c1 c0]
22.9 KV	[0.044965, 0.11241]	[1.01e-3, 3.54e-3]	[7.471e-9, 4.394e-9]
154 KV	[3.211786e-3, 8.029286e-3]	[1.04e-3, 3.64e-3]	[17.780e-9, 10.457e-9]

3.1.2 Rated operation state of the system model

With initial parameters set for all the equipment, the system can operate at the rated state, i.e., all bus-voltages can be maintained at nominal levels when adjusting the static var compensators. The simulation is performed for 0.3 seconds. As an example, the voltage curves at the substation TR2 (Bus 1) are shown in Figure 3.2.

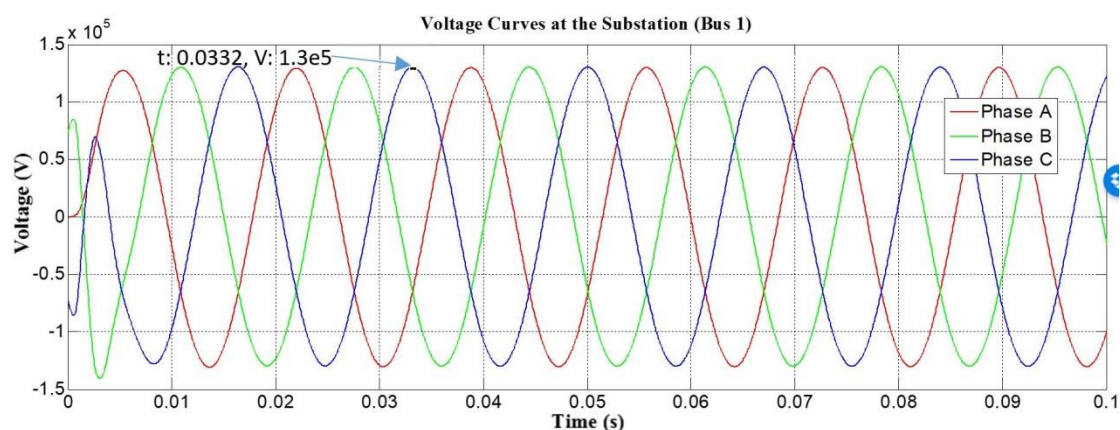


Figure 3.2: Voltage curves at the substation TR2 (Bus 1) under normal operation.

Figure 3.2 demonstrates that voltages at the substation reached the steady state after the first two cycles. According to the relationship between the peak voltage and the line to line voltage, it can be calculated that the rated phase-voltage at this point equals: $V_{TR2-P} = V_{TR2-Ph} \times \frac{\sqrt{2}}{\sqrt{3}} = 125.7 \text{ KV}$. Compared to this rated value, the data cursor in Figure 3.2 shows that the stable voltage of the simulation result is only 3.3% higher (129.8 KV).

Figure 3.3 presents the rated power flow at several locations in the studied power system model. Firstly, it can be seen from the power output of the wind farm that the five 2 MVA wind turbines generate 9.689 MW during normal operation. In total 3.135 MW out of the 9.689 MW is supplied to the domestic loads branch network (green curve), 6.528 MW is transmitted towards Bus 3 (blue curve), whilst the remaining power (0.026 MW) is consumed on the transmission lines. Furthermore, the 6.528 MW

power splits into two parts, so that 6.052 MW is supplied to the industrial load branch network to fulfil its power demand, 0.228 MW is fed to the local load of the conventional power plant, and the other 0.248 MW is consumed during the transmission process. Hence, under rated operation the system can be understood in a simplified scenario as a conventional power plant that feeds its local load, and the wind farm supplies power to all the rest of the loads.

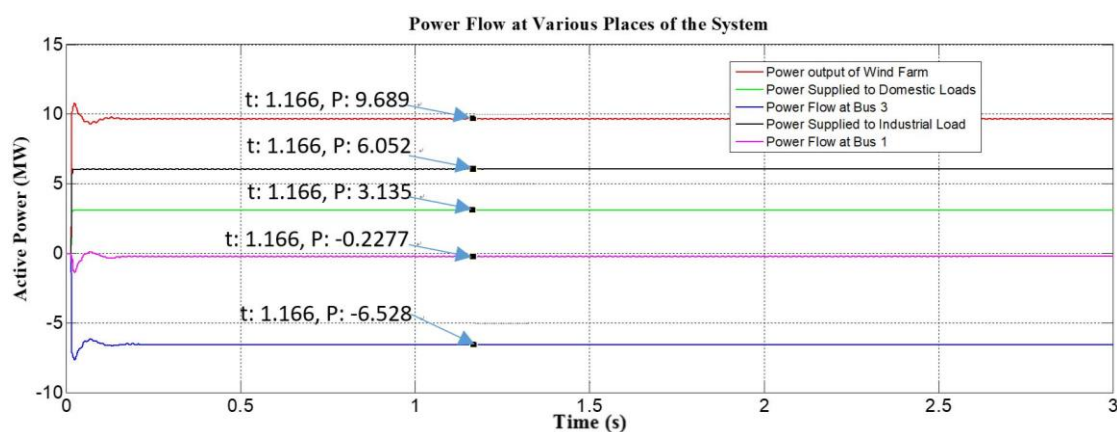


Figure 3.3: Power flow at various places in the studied power system model.

3.2 Simulations and Analysis of Short-Circuit Fault in the Power System Model

3.2.1 Simulations of short-circuit faults in the system model

Based on the designed power system model, three different types of faults of interest have been studied: the distribution grid fault, the customer grid fault, and the transmission line fault. The specific locations for these faults are shown in Figure 3.4. For simplicity and representativeness, only the three-phase-to-ground fault is simulated, as it is the worst possible scenario. When a short-circuit fault occurs, the profiles of current at Bus 3 (current output from the conventional power plant), Bus 4 (wind farm output), and Bus 5 (the domestic loads branch) are monitored.

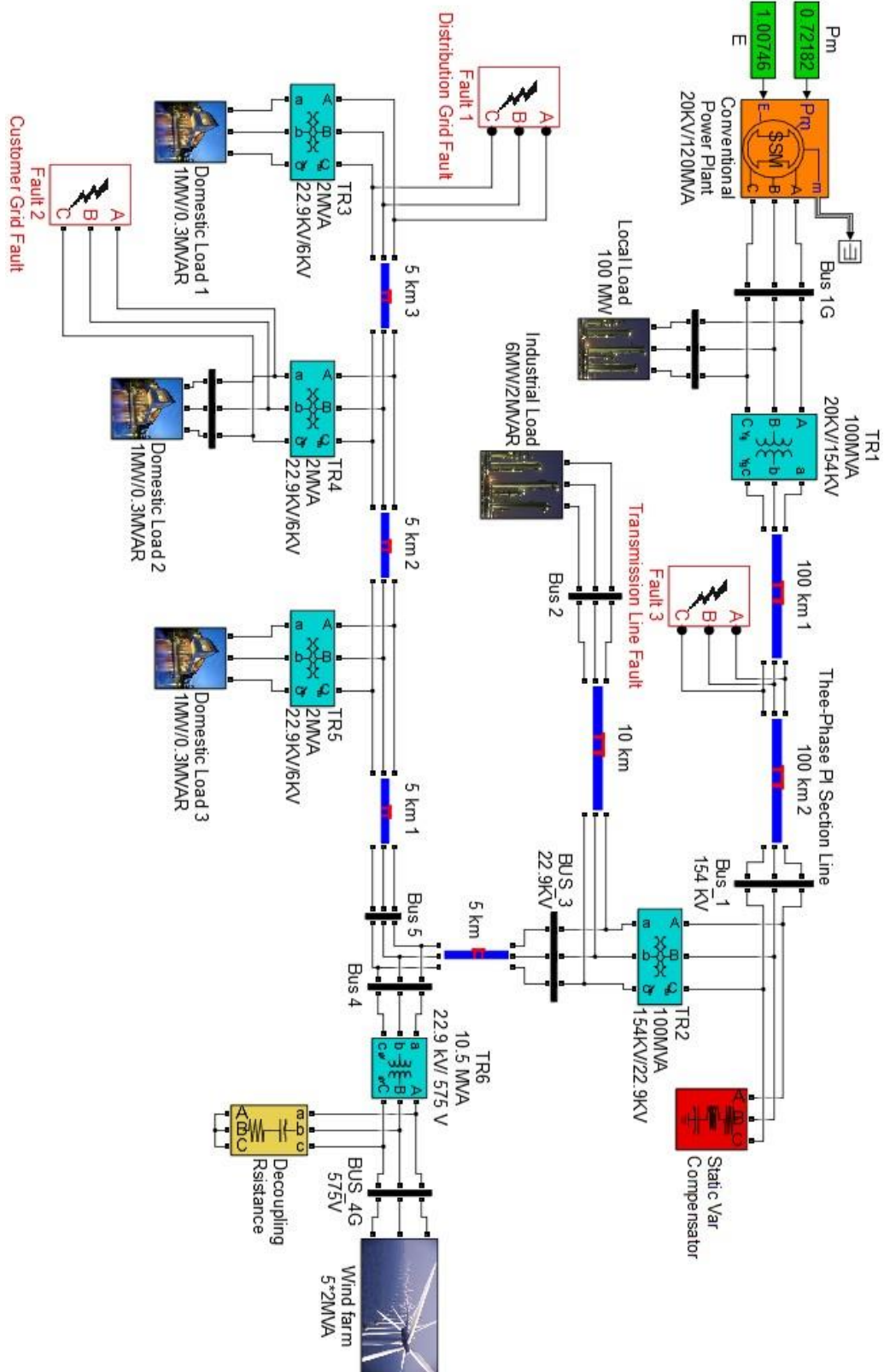


Figure 3.4: Locations of the three proposed faults in the studied power system model.

Under a three-phase-to-ground fault lasting for 150 milliseconds at the distribution grid side (Fault location 1 in Figure 3.4), the current responses at Bus 3 to 5 are plotted in Figure 3.5.

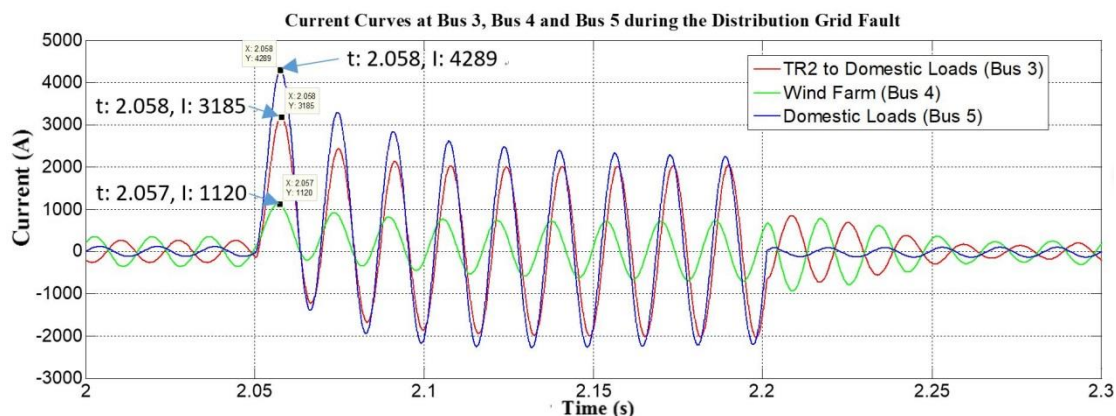


Figure 3.5: Current flowing from transformer 2 (Bus 3) and wind farm (Bus 4) to domestic load branch & total current of domestic loads (Bus 5).

It can be seen that the fault current of the domestic loads reaches as high as 4290.7 A, which is 35.9 times higher than the flowing current before the three-phase-to-ground distribution grid fault (116.2 A). With a fault current of this level, severe damage to facilities and/or even physical safety issues are very likely to happen if no effective fault current control techniques are implemented.

3.2.2 Analysis of the short-circuit fault

According to Lenz's law, the fault current cannot change suddenly at the instant of short-circuit. However, since the periodic components of current before and after the fault are not identical, a self-inductance current has to be induced in order to maintain continuity of the circuit current, thus preventing any sudden change to the circuit current. This self-inductance current is the source of the aperiodic component of short-circuit current that previously observed [119].

The transient analysis of single-phase short-circuit current begins with the equivalent circuit diagram of the system shown in Figure 3.6.

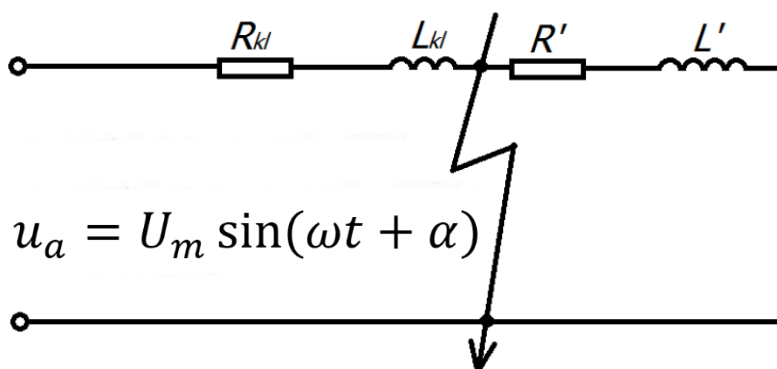


Figure 3.6: Single-phase equivalent circuit diagram of a power system [120].

Before occurrence of the fault, the phase voltage can be described as:

$$u_a = U_m \sin(\omega t + \alpha) \quad (3.1)$$

The current along the transmission line equals to:

$$i = I_m \sin(\omega t + \alpha - \varphi) \quad (3.2)$$

where I_m stands for the amplitude of the line current. The expression of I_m is:

$$I_m = \frac{U_m}{\sqrt{(R_{kl}+R')^2 + \omega^2(L_{kl}+L')^2}} \quad (3.3)$$

The parameter φ in Equation 3.2 represents the impedance angle, i.e., the angle by which the current lags the voltage, by a phase of:

$$\varphi = \tan^{-1} \frac{\omega(L_{kl}+L')}{R_{kl}+R'} \quad (3.4)$$

Illustration of the angles α and φ is given in Figure 3.7.

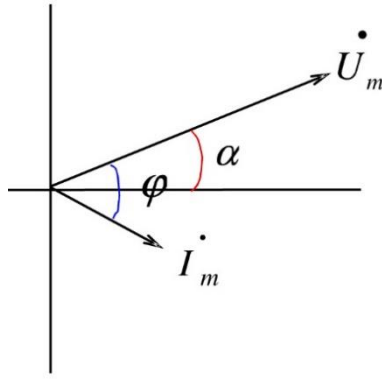


Figure 3.7: Diagram of the voltage angle and the impedance angle during normal operation [119].

After a fault occurs, the current sharply increases from the rated value. Then, when the load's impact on the short-circuit current is ignored, the expression of the short-circuit current could be derived by solving the differential equation:

$$u = U_m \sin(\omega t + \alpha) = R_{kl} i_k + L_{kl} \frac{di_k}{dt} \quad (3.5)$$

Thus, by solving the nonhomogeneous differential equation of the first order, it could be deduced that the instantaneous current is equal to [121]:

$$i_k = \frac{U_m}{Z_{kl}} \sin(\omega t + \alpha - \varphi_{kl}) + ce^{-\frac{t}{T_k}} = I_{pm} \sin(\omega t + \alpha - \varphi_{kl}) + ce^{-\frac{t}{T_k}} \quad (3.6)$$

where:

$$I_{pm} = \frac{U_m}{Z_{kl}} = \frac{U_m}{\sqrt{R_{kl}^2 + (\omega L_{kl})^2}} \text{ is the periodic component of short-circuit current,}$$

$$\varphi_{kl} = \arctan \frac{\omega L_{kl}}{R_{kl}} \text{ is the impedance angle after the short-circuit fault, and}$$

$$T_k = \frac{L_{kl}}{R_{kl}} \text{ is the time constant after the short-circuit fault.}$$

Lenz's law indicates that the current has to be continuous at the instant the short-circuit fault occurs, which means that the momentary current before the fault (expressed by i_{0+}) is equal to the momentary current after the fault (expressed by i_{0-}). Then, by substituting $t = 0$ into Equation 3.2 and Equation 3.6, the expressions for i_{0-} and i_{0+} can be deduced:

$$\begin{cases} i_{0-} = I_m \sin(\alpha - \varphi) \\ i_{0+} = I_{pm} \sin(\alpha - \varphi_{kl}) + c \end{cases} \quad (3.7)$$

Thus, based on the relationship $i_{0-} = i_{0+}$ and Equation 3.7, the integration constant c is equal to:

$$c = I_m \sin(\alpha - \varphi) - I_{pm} \sin(\alpha - \varphi_{kl}) \triangleq i_{ap0} \quad (3.8)$$

where i_{ap0} defines the initial value for the aperiodic component of the short-circuit current.

Hence, the expression of the short-circuit current can be derived by substitution of Equation 3.8 into Equation 3.6, as follows:

$$\begin{aligned} i_k &= I_{pm} \sin(\omega t + \alpha - \varphi_{kl}) + c e^{-\frac{t}{T_k}} \\ &= I_{pm} \sin(\omega t + \alpha - \varphi_{kl}) + [I_m \sin(\alpha - \varphi) - I_{pm} \sin(\alpha - \varphi_{kl})] e^{-\frac{t}{T_k}} \\ &= i_p + i_{ap} \end{aligned}$$

where $i_p = I_{pm} \sin(\omega t + \alpha - \varphi_{kl})$ stands for the periodic component of the short-circuit current, whose magnitude, I_{pm} , is a constant defined by the source voltage and circuit impedance. On the other hand, $i_{ap} = [I_m \sin(\alpha - \varphi) - I_{pm} \sin(\alpha - \varphi_{kl})] e^{-\frac{t}{T_k}}$ represents the aperiodic component of the short-circuit current, whose initial value is i_{ap0} (see Equation 3.8) and then is exponentially damped with a time constant, T_k [121]. These two fault current components, i_p and i_{ap} , are illustrated in Figure 3.8.

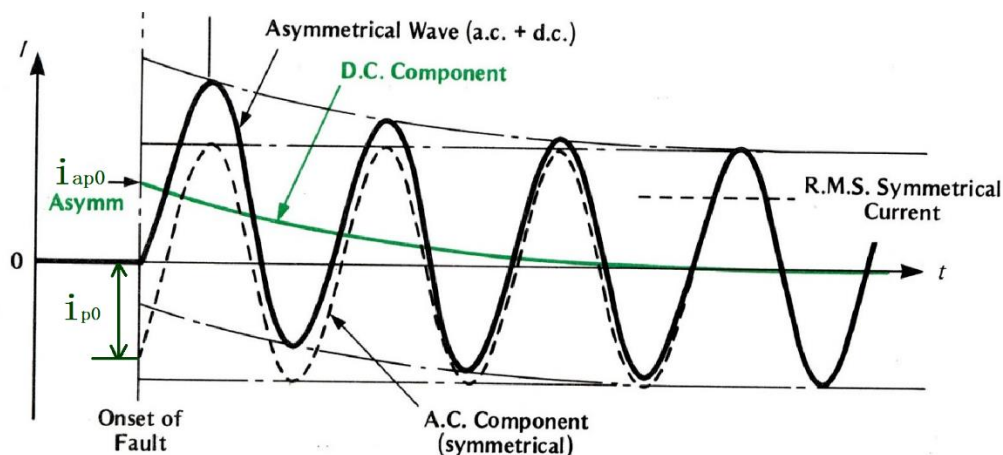


Figure 3.8: Diagram of the periodic and the aperiodic components of short-circuit current [121].

The emergence of the aperiodic component could substantially increase the peak value of the short-circuit current, where high fault current levels have enormous negative implications on the power system. For instance, it increases the possibility of short-circuit arcs which may lead to severe destruction of electrical facilities. Moreover, in the worst scenarios, the conductors could be damaged by electro-dynamic forces induced by the fault current. Also, the occurrence of harmonics as well as the significant sag in voltage nearby the fault location dramatically lowers the power quality of the network, resulting in system incompatibility with the growing demand of loads.

3.3 Design and Performance Test of an RSFCL Model

3.3.1 Operating principle of the RSFCL

Consider a simple power system model, as shown in Figure 3.9. This model consists of a source with rated voltage V_s , internal impedance Z_s , load Z_{load} , and fault impedance Z_{fault} .

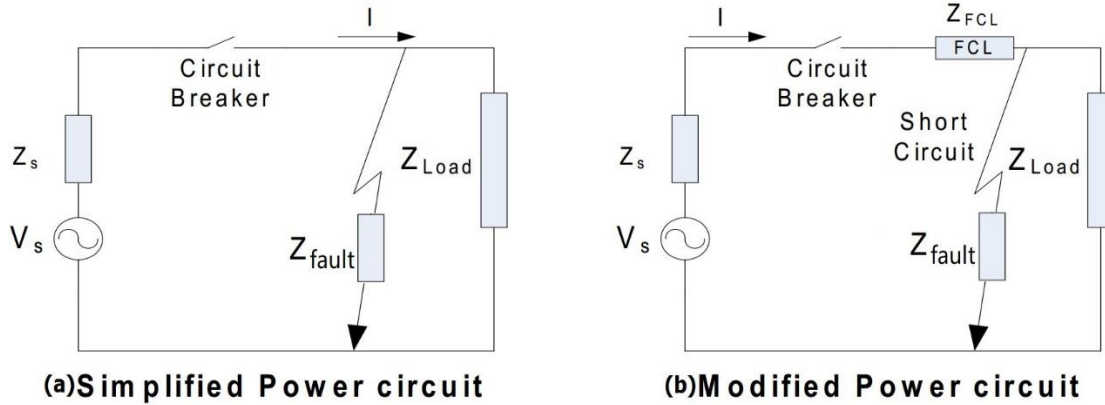


Figure 3.9: Equivalent diagram of a simple power circuit (a) without and (b) with SFCL [122].

When the system is in a steady state, the current flowing through the line is defined by:

$$I_{line} = \frac{V_s}{Z_s + Z_{load}} \quad (3.9)$$

Then, when a fault occurs as shown in Figure 3.9 (a), the current flowing through the line is defined by:

$$I_{line} = \frac{V_s}{Z_s + Z_{fault}}, \text{ where } Z_{fault} \ll Z_{load} \quad (3.10)$$

Because the source impedance, Z_s , is much smaller than the load impedance, Equation 3.10 shows that the short circuiting of the load substantially increases the current flow. However, if an SFCL is placed in series, as shown in Figure 3.9 (b), we must define I_{fault} as follows:

$$I_{line} = \frac{V_s}{Z_s + Z_{SFCL} + Z_{fault}} \quad (3.11)$$

Equation (3.11) indicates that by insertion of an SFCL, the fault current becomes a function of not only the source impedance, Z_s , and the fault impedance, Z_{fault} , but

also the impedance of the SFCL. Hence, for a given source voltage, the fault current I_{fault} decreases as the Z_{SFCL} increases.

3.3.2 Design of the RSFCL model

The three-phase SFCL module is designed by considering five fundamental parameters for the prototyping of a resistive type SFCL [123]:

1. The transition time, between the superconducting state to the normal state, simply called the SFCL response time, i.e., the time period after which the fault current limiter responds to a short-circuit fault current.
2. The minimum impedance, i.e., the impedance of the SFCL during normal operation (superconducting state).
3. The maximum impedance, i.e., impedance of the SFCL under a short-circuit fault, also called the quench state.
4. The triggering current, i.e., the amount of current required for quenching the SFCL.
5. The recovery time, i.e., the time period after which the SFCL is restored from the quenched state to its superconducting state, and the fault is cleared out of the power system.

In a three-phase power system, each phase of the SFCL must be simulated separately as each phase is triggered by only the current flowing in its own phase. In particular, under the condition of an unbalanced primary system fault, which is actually the predominant mode of faults in power distribution systems (especially in overhead systems) [124], within the first cycle of fault current during a three-phase-to-ground

fault, each phase of the SFCL will quench slightly asynchronously, which leads to an instantaneous unbalance of the phase. Furthermore, unbalanced faults can also lead to the occurrence of a quench in only one or two phases of the entire SFCL. Hence, independent modules for each one of the three phases have to be considered in order to allow for accurate simulation of the SFCL's effects on the overall power grid, and for all types of fault at diverse locations [125]. The structure of the SFCL module built in this project is shown in Figure 3.10.

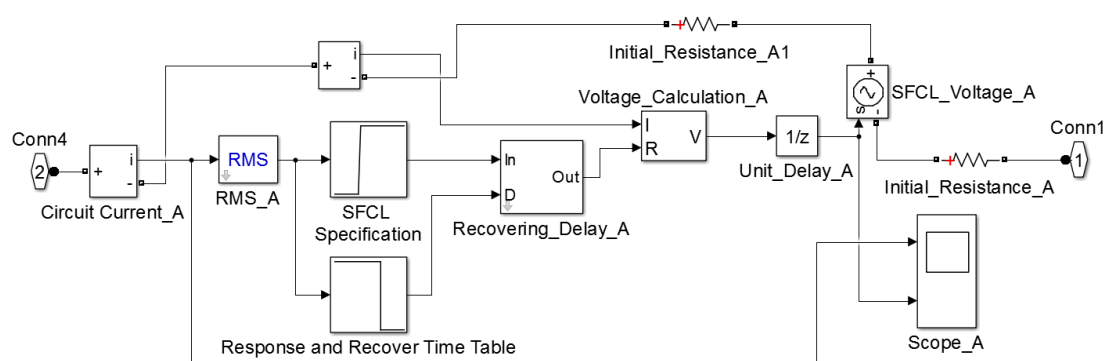


Figure 3.10: Phase A of the SFCL model developed in the Simulink/SimPowerSystem module of Matlab.

The block diagram of the SFCL for phase A is identical to the modules used for the other two phases. Thus, the entire SFCL is composed of three single-phase-modules working in parallel. The values of the fundamental parameters of a resistive type SFCL as explained above are listed in Table 3.3.

Table 3.3: Fundamental parameters of the RSFCL model.

No.	SFCL Parameters	Values
1.	Transition/Response Time	2 ms
2.	Minimum/Normal Operating Impedance	0.01 Ω
3.	Maximum/Quenching Impedance	50 Ω
4.	Triggering Current	200 A

This SFCL model is defined to be a current-controlled voltage source, equivalent to a current-controlled variable resistance. The working sequence for the operations flow in the SFCL module can be summarized as follows.

Firstly, the SFCL module calculates the RMS value of the flowing current. Then, the RMS value is compared with the SFCL characteristic curve (predefined in the “SFCL Specification” block inside the SFCL module, as shown in Figure 3.10). If the flowing current is lower than the triggering current (200 A in this case), the SFCL Specification block outputs the resistance of the superconductor as 0.01 Ω . If the incoming current exceeds the triggering current, the SFCL specification block outputs the quenching impedance (50 Ω) to the voltage calculation block after a delay of the response time (2 milliseconds [116]). In addition, the resistors on both sides of the controlled voltage source have the same resistance of 5 m Ω . These two resistors together form the initial resistance of the SFCL, which is defined as 10 m Ω .

Secondly, the voltage calculation block generates a voltage signal based on the current measurement and the resistance value determined by the SFCL Specification block. This voltage signal is then sent to the controlled voltage source through a unit delay. The reason for adding a unit delay block is to avoid the algebraic loops in this model, which may make the system unstable. Basically, an algebraic loop occurs when a signal loop exists with only direct feedthrough blocks. Direct feedthrough means that the block output depends on the value of an input port, and the value of the input is controlled by the value of the output. For the SFCL model, the output of the controlled voltage source depends on the current of the system, and in the meantime the current of the system is affected by the voltage output of the SFCL module. An effective approach to eliminate the algebraic loop is to integrate non-direct-feedthrough blocks such as the Unit Delay block [126].

Figure 3.11 shows the curves of the current flowing into phase A of the SFCL, the corresponding RMS calculation, the voltage output of the controlled voltage source, and the system current at Bus 2. The RMS calculation was conducted by running the average of one cycle of the specified fundamental frequency:

$$RMS(f(t)) = \sqrt{\frac{1}{T} \int_{t-T}^t f(t)^2} \quad (3.12)$$

where $f(t)$ is the input signal, and T is the corresponding oscillation period.

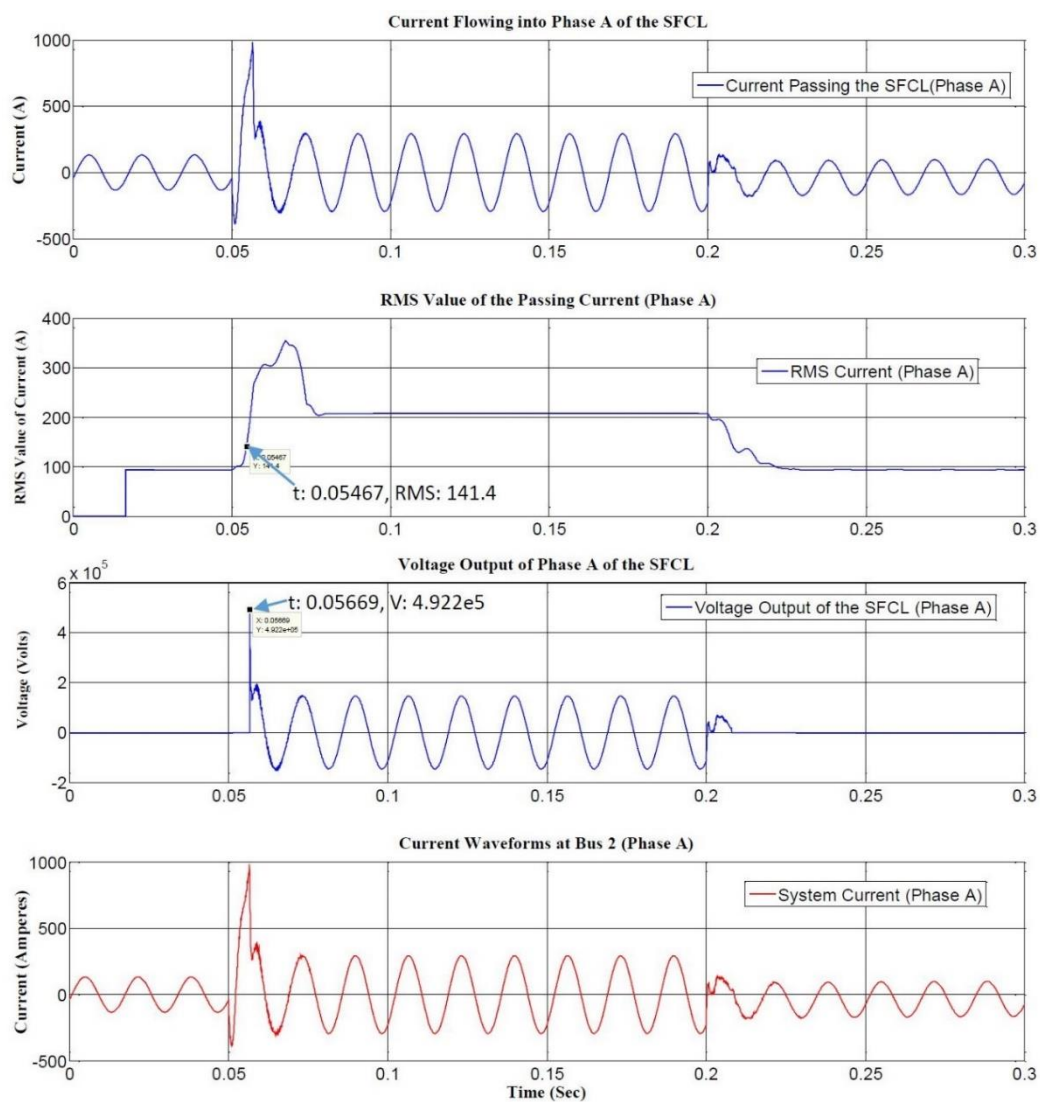


Figure 3.11: The current limiting behaviour of the SFCL while it is under a short-circuit fault. For the sake of clarity, only current profiles of one phase are plotted.

The data cursors in the second and third curves shows that the RMS value of the short-circuit current rises to the triggering current ($\frac{200 \text{ A}}{\sqrt{2}} = 141.4 \text{ A}$) at 54.7 milliseconds, and then the SFCL quenches after the defined transition time of 2 milliseconds. The response is exactly as expected, with the exception that this SFCL model is not capable of limiting the fault current during the first half cycle of the short-circuit current (a 984.4 A peak appears at 56.7 milliseconds, 6.5 times higher than the rated current). This result is due to the limitation that for a fault happening at time t_0 , the RMS calculation block can only output the RMS value of the flowing current over the past cycle, i.e., from $(t_0 - T)$ up to t_0 . Hence, the result will be just above the rated value even when the short-circuit current at t_0 is extremely high. In other words, compared to the instantaneous current, the signals that the RMS calculation block generates are always delayed due to the integral operation.

This undesirable effect needs to be eliminated because in reality the speed of resistive type SFCLs responding to short-circuit faults is much faster than that of the model shown in Figure 3.11 [77]. Thus, in order to increase the response speed of the SFCL model, a branch that monitors the real-time passing current is designed, connected in parallel with the RMS calculation block. The modified SFCL model is shown in Figure 3.12.

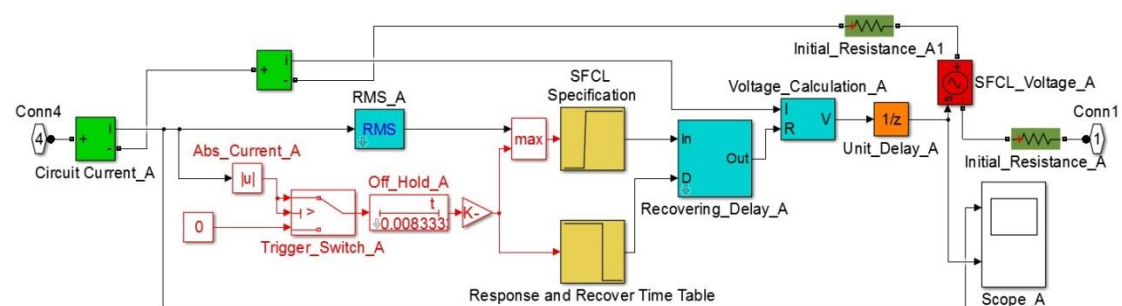


Figure 3.12: Diagram of the single phase of the advanced SFCL model which has the switching branch.

In Figure 3.12, the red blocks together form the switching branch which has the ability to generate a quenching signal during the first few milliseconds of a prospective short-circuit fault. Its working principle is as follows: to begin with, the absolute value of a measured current is sent to a switch block. When the instantaneous value of the passing current is higher than the pre-defined triggering current (200 A as stated before), the switch block outputs this real-time current to an off-hold block, otherwise, it outputs a constant 0 instead. The role of the off-hold block is that when the input becomes FALSE (0), the output becomes FALSE after the specified time delay, as long as the input is still FALSE. If the input becomes TRUE (>0) before the time delay has expired, the output stays as TRUE. By setting the time delay of the off-hold block to half of a cycle, the SFCL model can quench properly before the first peak, with negligible influence on the its recovering behaviour.

The main reason for having the switching branch and the RMS calculation branch working in parallel is that, despite the fault current being only slightly higher than the triggering current, sometimes several current peaks may be lower than the triggering current due to the existence of harmonics. This could lead to fault switching if the quenching signal solely depends on the instantaneous current. Cooperation of these two different strategies could enable the SFCL model to quench and recover not only quickly but also stably. The performance of the advanced SFCL model during the single-phase-to-ground fault is illustrated in Figure 3.13.

The first plot in Figure 3.13 describes the current flowing through phase A of the advanced SFCL model. It can be seen that the passing current exceeds 200 A at 50.3 milliseconds. Therefore, the switching branch sends a quench signal to the specification table, and then the SFCL gains resistance 2 milliseconds later even though the output of the RMS calculation block is merely 94.9 A (see Figure 3.22). Compared to the SFCL module illustrated in Figure 3.12, the bottom plot in Figure 3.13 shows how the first

peak of fault current is reduced to less than 400 A from 1000 A for the same power system model under the same fault condition.

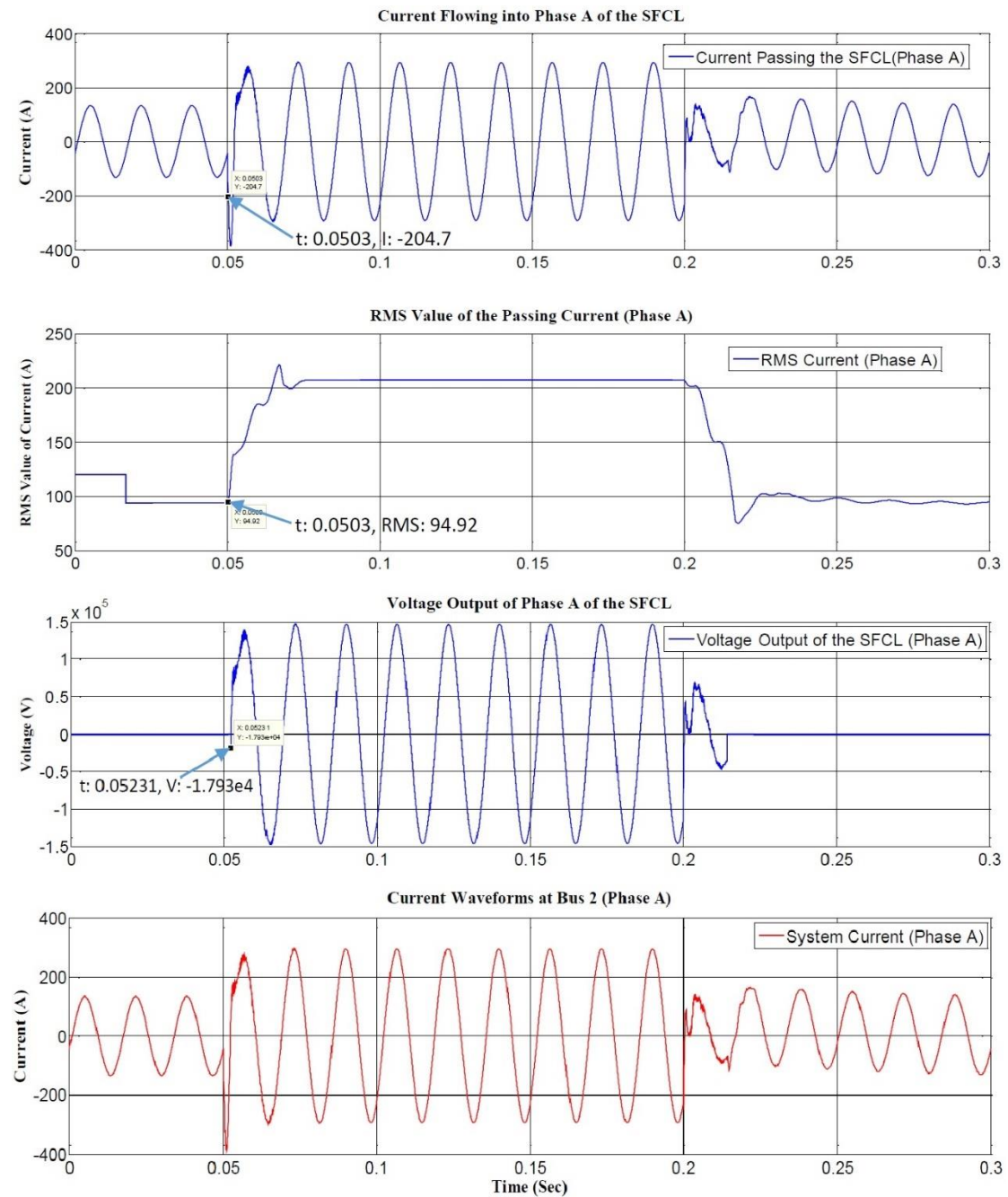


Figure 3.13: Performance of the advanced SFCL model and the corresponding Bus 2 current profiles.

3.3.3 Performance test of the RSFCL model

Before further analysis on the integration of an SFCL into the power grid, the current limiting performance of the SFCL module is tested. A three-phase-to-ground fault is initialized at the distribution grid, and the SFCL model is integrated at Substation TR2. By increasing the Maximum/Quenching Impedance from 5Ω to 35Ω , the curves of current at Substation TR2 (with and without SFCL) are achieved and are displayed in Figure 3.14.

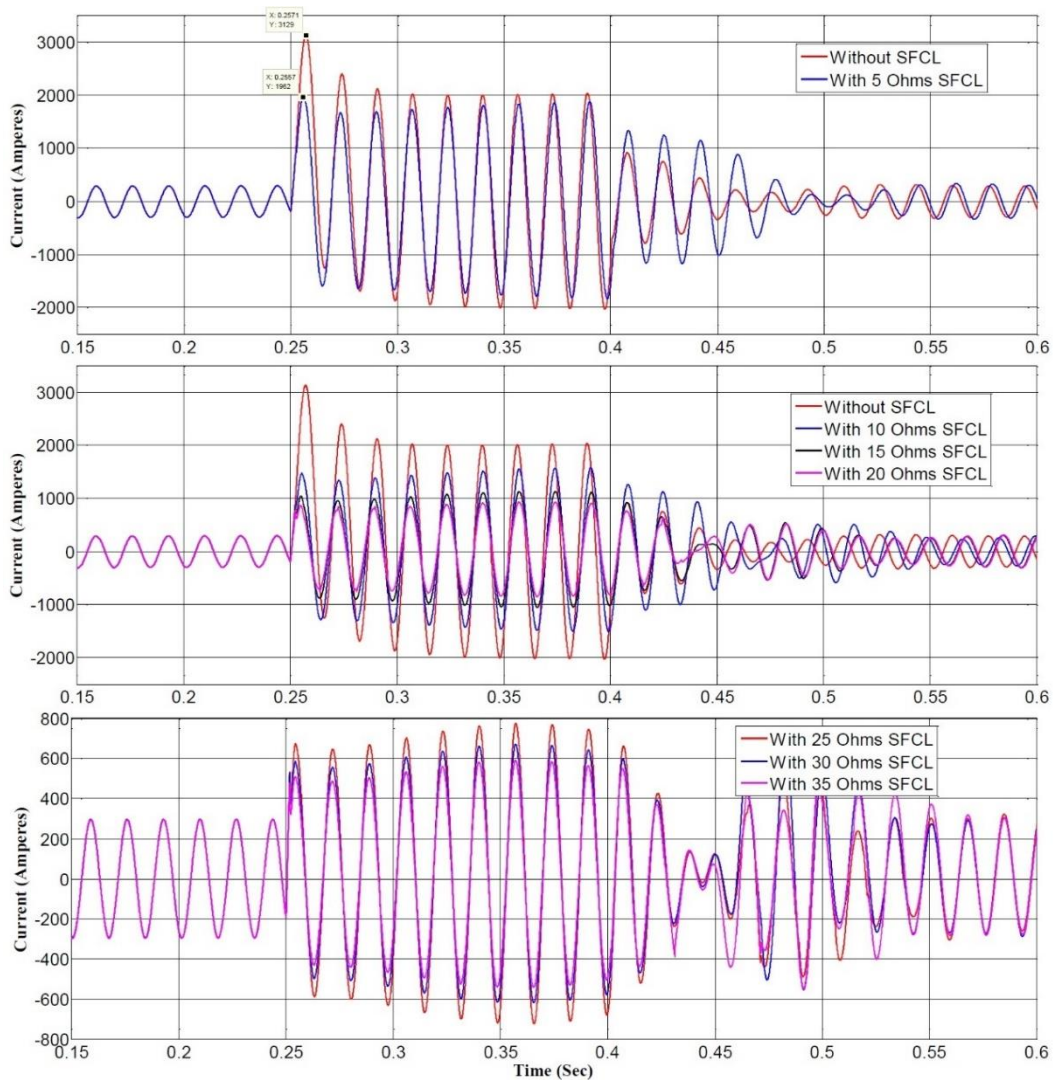


Figure 3.14: Current curves at substation TR2 without and with application of 5, 10, 15, 20, 25, 30, and 35Ω RSFCLs.

Figure 3.14 demonstrates that the fault current level at Substation TR2 (Bus 3) can be reduced from 3130.0 A to 1962.4 A by the integration of an SFCL with a quench impedance of 5 Ω , which means a 37.4% reduction of the fault current is achieved. Similarly, by increasing the quench impedance from 5 Ω to 35 Ω , we have found that the fault current levels can be limited by up to 81.1% (see Table 3.4).

Table 3.4: Performance of RSFCLs with various quench impedance.

Impedance of SFCL	Fault Current Levels	Reduction of Fault Current
0 Ω	3130.0 A	0.00%
5 Ω	1962.4 A	37.3%
10 Ω	1527.4 A	51.2%
15 Ω	1117.8 A	64.2%
20 Ω	916.3 A	70.7%
25 Ω	775.0 A	75.2%
30 Ω	671.2 A	78.5%
35 Ω	591.5 A	81.1%

As expected, the higher the SFCL quench impedance, the better the current limiting performance. However, because increasing the quench impedance requires greater investment, compromise should be made between the reduction in the fault current and the increased manufacturing cost.

3.4.1 Current limiting performance of the SFCL at Location 1

Installation of an SFCL at substation TR2 could potentially protect the transmission grid and the conventional power plant from being damaged by the fault current. Moreover, we foresaw that if the short-circuit fault appeared either at the side of the industrial load or the domestic loads, the fault current being injected from the conventional power plant could be effectively reduced. Thus, the SFCL could benefit the local load by mitigating the voltage and power drop problem.

After integration of the SFCL at Location 1 (substation TR2), the current output of the wind power plant is shown in Figure 3.16.

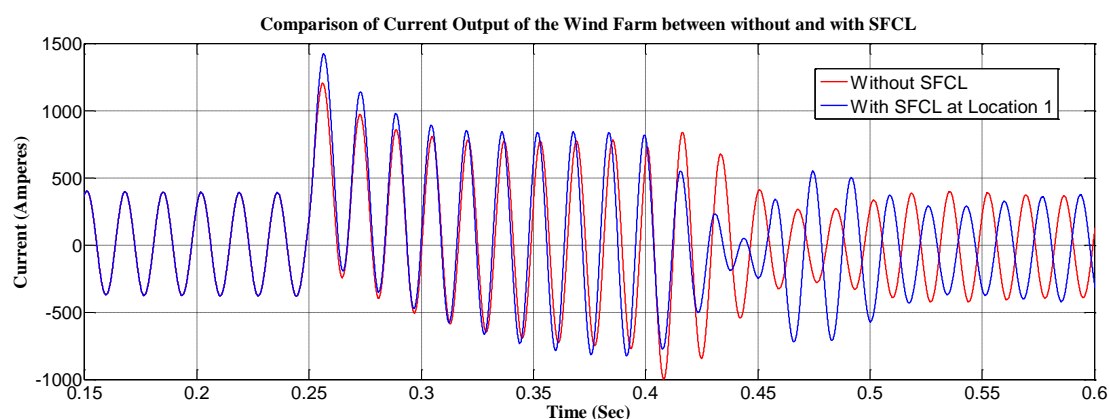


Figure 3.16: Current output of the wind farm when the distribution fault happens (with and without the SFCL at Location 1).

Unexpectedly, the current output of the wind farm under a distribution fault increased from 1124.3 A to 1433.9 A after the integration of the SFCL. In other words, installing an SFCL at Location 1 increased the DG fault current rather than limiting it, which shows that identifying the proper location of the SFCL is very important. The reason for this phenomenon is the abrupt change of impedance between the fault branch and the conventional power plant side. As illustrated by Figure 3.5, most of the short-circuit current of the domestic branch (Bus 5) under the distribution grid fault is powered by the conventional power plant. After quench of the SFCL at Location 1, the fault current

coming from the conventional power plant is substantially reduced. Therefore, the wind farm is forced to provide a higher current to the fault location (Fault 1).

3.4.2 Current limiting performance of the SFCL at Location 2

Installation of an SFCL at Location 2 is expected to be able to limit the fault current from the wind farm when the fault occurs at the Industrial Load, while an SFCL at Location 1 can reduce current coming from the conventional power plant. However, when faults occur at the domestic branch or the wind farm, the two strategies should have similar behaviour, as demonstrated in Figure 3.17.

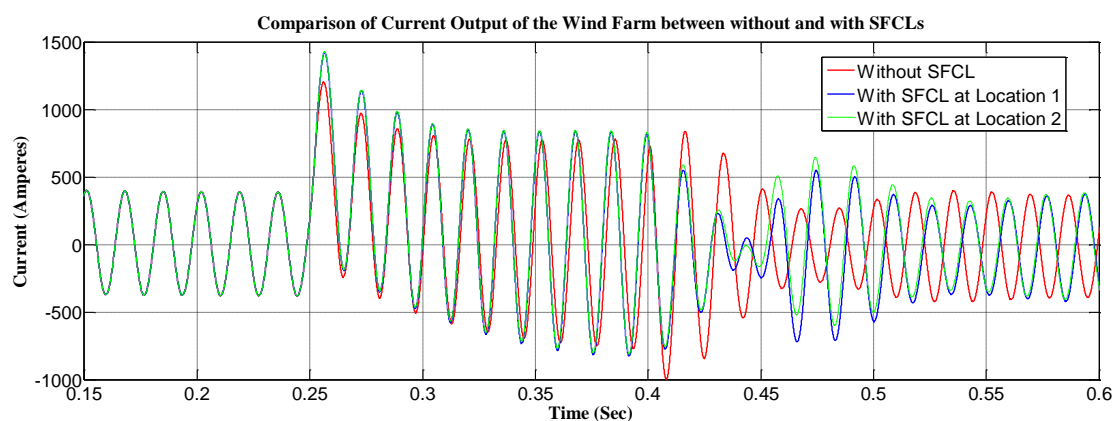


Figure 3.17: Current output of the wind farm when the distribution fault happens (without SFCL, SFCL at Location 1, and SFCL at Location 2).

3.4.3 Current limiting performance of the SFCL at Location 3

According to the system structure, it can be predicted instinctively that installing an SFCL at Location 3 (integration point) is the most effective strategy for protecting the distribution grid and the domestic loads. The reason is that, under this scenario, the SFCL could mitigate the current increase from both power plants, the conventional one and the wind farm. Simulation results of the wind farm current output after installation of an SFCL at Location 3 are shown in Figure 4.16.

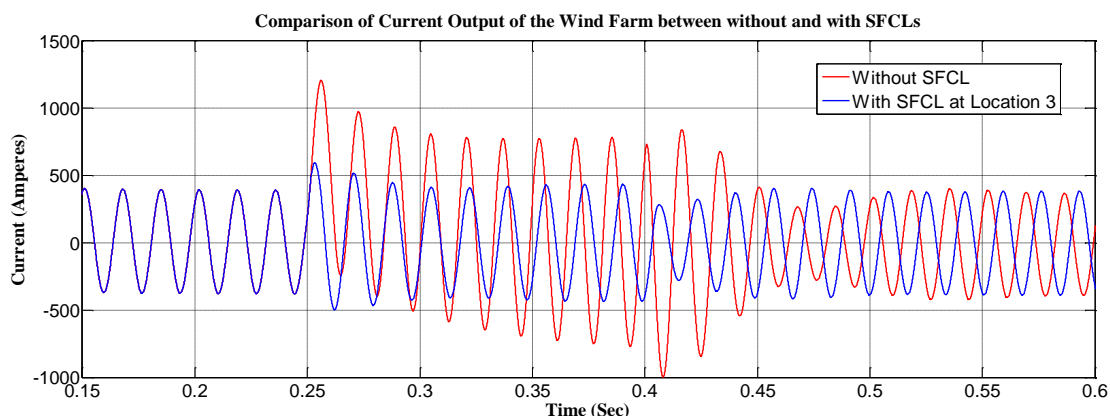


Figure 3.18: Current output of the wind farm when the distribution fault happens (with and without the SFCL at Location 3).

In this case, the wind farm fault current is significantly reduced from 1124.3 A to 566.5 A. This current level is acceptable for the wind power plant because it is lower than of the rated value 383.7 A. Moreover, the fault current coming from the conventional power plant is also effectively limited, and sag in voltages and power nearby the Local Load as well as the Industrial Load are both suppressed to an almost ideal level.

3.4.4 Current limiting performance of the simultaneous integration of two SFCLs at Location 1 and Location 4

Previous work has verified that a single SFCL integrated at Locations 1 or 2 is not capable of providing proper protection for the wind power plant during the distribution grid fault. Therefore, it is necessary to add another SFCL next to the wind farm. Theoretically, this arrangement should have better performance despite the fact that the required investment will become higher. The current limiting performance of cooperation of SFCLs at Location 1 and Location 4 is plotted in Figure 3.19.

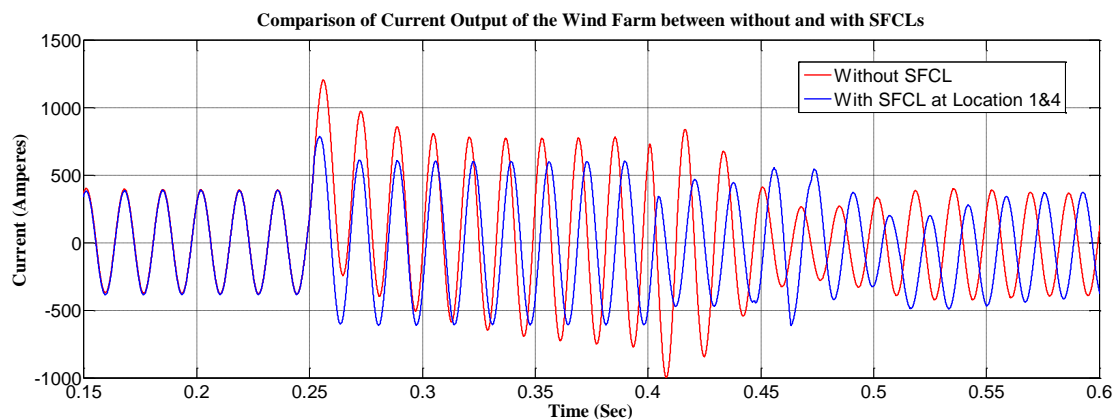


Figure 3.19: Current output of the wind farm when the distribution fault happens (without and with SFCLs at Location 1 and Location 4).

It can be seen that two SFCLs at Location 1 and Location 4 can effectively reduce the fault current at the wind power plant to 797.8 A, which is higher than the limited current achieved by a single SFCL installed at the domestic branch (Location 3). Although the performance of wind farm protection is not desirable, the main advantage of this strategy compared with the single SFCL scenario is that the fault current coming from the conventional power plant and the wind farm both can be reduced when the fault occurs at the Industrial Load.

In summary, for the wind farm protection under the distribution fault, installing the SFCL at either Location 1 (Substation TR2) or Location 2 (Branch Network) is not wise. In addition, with two SFCLs installed simultaneously at Location 1 and Location 4, the current output of the wind farm is only limited by 29.04% under a fault. However, when the SFCL is installed at Location 3 (Integration Point), the fault current can be significantly reduced by 50.4%. Thus, placing an SFCL at Location 3 is the best strategy.

3.5 Analysis of System Behaviours under Customer Grid Fault & Transmission Line Fault

3.5.1 Customer grid fault analysis

The customer grid fault is not as severe as the distribution grid fault, since it occurs in the low voltage side of the distribution network (see Figure 3.15), and the fault resistance is significantly higher due to the existence of transformer TR4. However, the fault is essentially equivalent to the distribution grid fault seen from the other part of the power system. Hence, for wind power plant protection using SFCLs, the only difference between the SFCL performances at the same locations under the two faults is basically a scaling factor. So, as demonstrated in Section 3.4, the best strategy is integrating a sole SFCL at Location 3 to protect the wind power plant. In fact, when two SFCLs are simultaneously connected to the power grid, one installed at Location 1, and the other at Location 4, the fault current level at the domestic branch (measured at Bus 5) is greater than the case of one SFCL at Location 3, as can be seen from Figure 3.20.

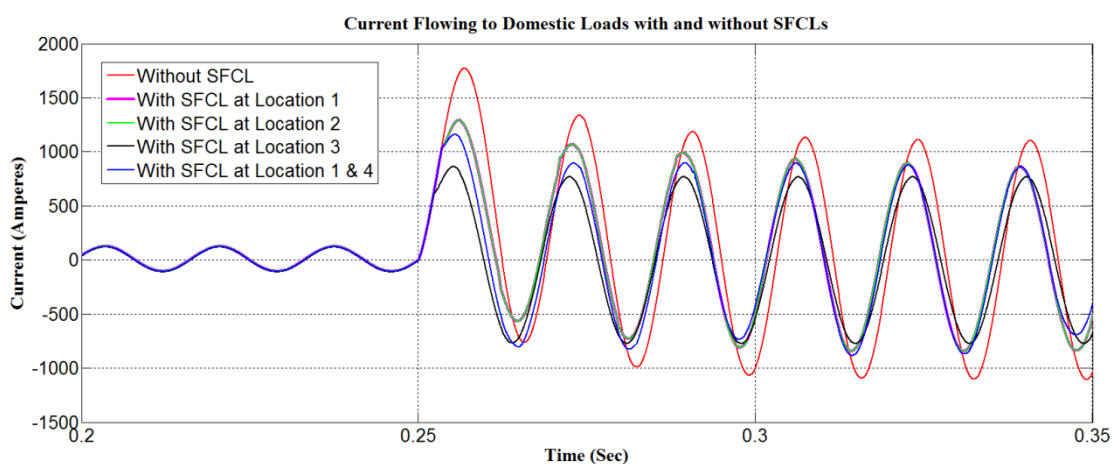


Figure 3.20: Current flowing into the domestic branch under a customer grid fault (without and with different SFCL installation strategies).

Aside from the conclusion that the optimal strategy is to install an SFCL at Location 3, it is also worth noticing that the total current flowing into the domestic loads branch could be reduced by a single SFCL either at Location 1 or Location 2, despite these strategies both having a bad influence on the wind power plant. This implies that most of the fault current comes from the conventional power plant side.

3.5.2 Transmission line fault analysis

Overhead power transmission lines are commonly exposed to a wide range of environmental hazards such as lightning strikes, falling trees, and in general any adverse climatic condition capable of inducing an electrical fault. For instance, fog and salt spray on dirty insulators may cause the insulator strings to flash over, and ice and snow loadings may cause insulator strings to fail mechanically. Thus, the likelihood of a fault on the transmission line is higher than that of other main components [127].

However, faults on overhead power lines of levels like 154 KV are quite rare, because the transmission towers and their overhead power lines are designed as tall structures, so that they can resist environmental mechanical strains [128]. Nevertheless, the occurrence of this kind of fault is extremely dangerous as the fault current magnitude in the system tends to significantly increase. For the power system model studied in this chapter, when a fault in the transmission line happens, the fault current from the conventional power plant flows towards the fault point. Also, very high fault current from the wind power plant flows upwards through the substation TR6 and enters the transmission line.

Figure 3.21 shows the behaviour of the wind farm (measured at Bus 4) when a three-phase-to-ground fault is initiated in the transmission line (Fault 3 in Figure 3.15). The models of SFCLs are placed according to the previously proposed allocation strategies.

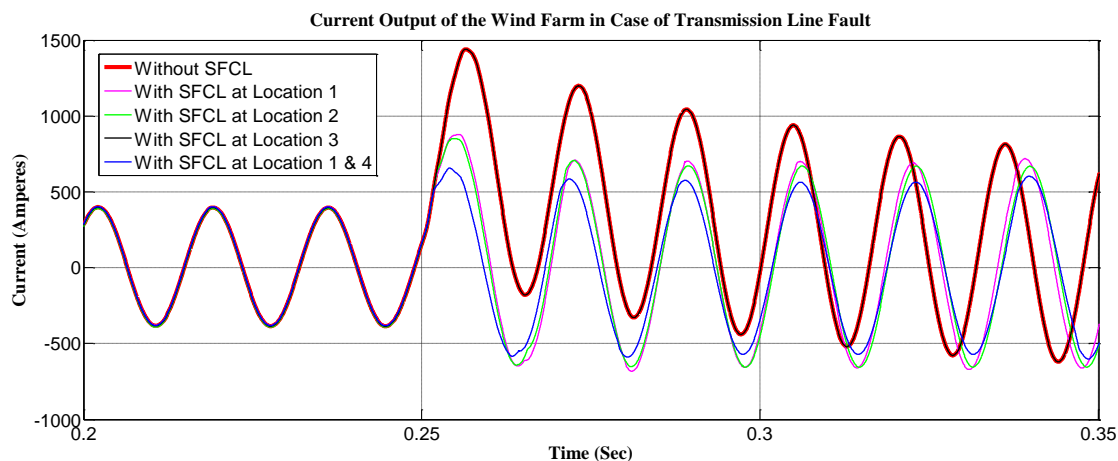


Figure 3.21: Current output of the wind farm when the transmission line fault happens (without and with different SFCL installation strategies).

Contrary to the results obtained before, the curves displayed in Figure 3.21 show that a sole SFCL installed either at Location 1 or Location 2 is capable of reducing the wind farm fault current from 1439.4 A to about 883.2 A. The reason is that, under a transmission line fault, the current output of the wind farm goes upward through Bus 3 and Bus 1 into the transmission system. Hence, both Location 1 and Location 2 lie in the path of the current. In addition, an SFCL installed at Location 3 is not helpful to the wind power plant during a transmission line fault, since the wind farm fault current does not flow through it. This fact explains why the black and red curves in Figure 3.21 are almost identical. Finally, when two SFCLs are simultaneously placed at Locations 1 and 4, a greater reduction of the wind farm fault current is achieved (down to 623.3 A). However, it cannot be neglected that the required investment for this strategy required is double that of the other plans.

3.6 Conclusions

In this Chapter, a power system model based on the Korean electric grid [116] was built, and the transient analysis of short-circuit currents was explained. The operating principle of RSFCL and the detailed structure of a step-resistance RSFCL model were briefly introduced. In order to validate the current limiting performance of the SFCL

module, wind farm protection schemes were studied under three fault scenarios: the distribution grid fault, the customer grid fault and the transmission line fault. The main results of this chapter are summarized in the bar chart shown in Figure 3.22. This chart demonstrates a comparison between the wind power plant fault current reductions achieved by SFCLs at different locations (see Figure 3.15).

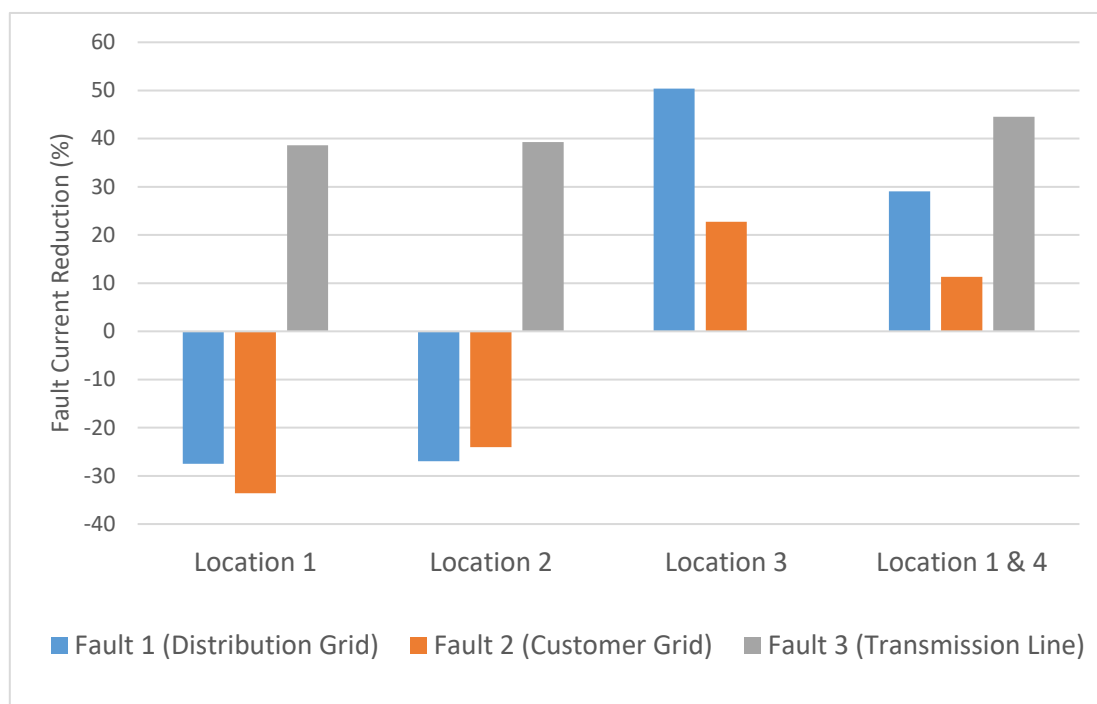


Figure 3.22: Reduction of fault current of wind farm achieved by SFCLs at different locations.

According to Figure 3.22, the following conclusions can be stated:

- i. Integration of a sole SFCL at Location 1 (Substation TR2) or Location 2 (Branch Network Feeder) will increase the wind farm fault current under Fault 1 and the Fault 2. Therefore, this strategy only qualifies to protect the wind power plant when the short-circuit fault occurs at the transmission line.
- ii. Installing a sole SFCL at Location 3 (Integrating Point) cannot provide protection to the wind power plant during the transmission line fault. However,

limitation of the wind farm fault current under the other two kinds of failures can be achieved.

- iii. When two SFCLs operate simultaneously, one installed at Location 1 (substation TR2) and Location 4 (Wind Farm side), the lowest wind farm fault current is achieved under the transmission line fault. However, the fault current reduction for the wind farm output in cases of the other two faults is not as good as the one obtained with an SFCL at Location 3.

Therefore, from the economic point of view, the optimal allocating strategy of SFCLs for the studied power grid model is the integration of one SFCL at Location 3, since the fault currents can be effectively limited, and the DG source is not negatively affected. However, from the technical point of view, installing two SFCLs at Location 1 and Location 4 is the optimal strategy for the studied grid model. With this arrangement, the system is well protected under all fault scenarios.

Chapter 4

Real-Time RSFCL Model and its Optimal Allocation Strategies in Power Systems

Previous studies conducted by other researchers about modelling of RSFCLs in power systems are mostly rely on the insertion of a predefined step or exponential resistance. In this chapter, we improved the step-resistance model developed in Chapter 3 by considering the actual behaviour of an SFCL, such as the mutual influence between the electrical field and the current density, and the temperature characteristics of HTS materials. This real-time RSFCL model, the step-resistance model and the exponential-resistance model were integrated into two power system models, in order to study the differences in simulating results that brought by different RSFCL modelling methods. The conclusion of this chapter is valuable for power system operators, as it can establish a maximum investment threshold which can facilitate making decisions regarding the deployment of SFCL technologies.

4.1 Conventional Modelling Methods of RSFCLs for Power System Protection

With the persistent increase of conventional system generation and distributed generations (DGs), such as photovoltaic plants, concentrating solar power plants, and wind farms, the likelihood of fault events capable of causing great and irreparable damage to a large set of electrical devices, or even system blackouts, has been rapidly rising [129, 130]. As stated in Chapter 3, various strategies for mitigating fault current levels have been implemented in the power industry, such as construction of new substations, splitting existing substation buses, upgrading of multiple circuit breakers,

and the installation of high impedance transformers. Nevertheless, all these operational practices involve a non-negligible degradation of the systems stability and performance, which ultimately means the occurrence of significant economic losses and further investment [131]. Series reactors and solid state fault current limiters are also widely used, although these insert a high impedance causing a continuous voltage drop and power losses during normal operation [132]. However, superconducting fault current limiting technology can stand up to all these difficulties, preserving the stability and reliability of the power system with minimum losses under normal conditions [133], although a comparison of different fault protection approaches is out of the scope of this manuscript. An exhaustive review on successful field tests and different existing numerical models of SFCLs can be found in Ref. [134].

Two simplified SFCL models have been identified as in common use for simulating the performance of SFCLs installed in real power grids. The first approach is to model the SFCL as a step-resistance with a pre-defined triggering current, quench time, and recovery time, as has been thoroughly demonstrated in the last chapter. This approach allows us to consider a simplified scenario where no energy loss occurs during the superconducting state and a high impedance in normal state, by assuming that the SFCL responds to faults instantaneously. However, this may lead to significant inaccuracies, since the quenching and recovery characteristics depend on the thermal and electrical properties of the superconductors, which are both neglected in this simplified model. Modelling of a resistive type SFCL can also be simplified by using an exponential function for the dynamic resistance of the SFCL device, in which the quenching action of the superconducting material is solely determined by time. This method has been previously implemented in Refs. [135] and [136], in order to study the optimal locations and associated resistive values of SFCLs for a schematic power grid with an interconnected wind-turbine generation system, which found that the installation of SFCLs cannot only reduce the short-circuit current level, but also dramatically enhance

the reliability of the wind farm. Compared to the previous approach, this exponential resistance curve fits better with the real performance of an SFCL and furthermore provides aggregated computational benefits in terms of numerical convergence. Nevertheless, SFCL characteristics, including triggering current, quenching, and recovery time, must also be set before initializing the simulation. Therefore, under this scenario the physical properties of the superconductors are ignored as well. A more advanced model for a resistive-type SFCL was presented in Ref. [137], in which both the physical properties and the real dimensions of superconductors were considered. A similar model was then built by D. Colangelo et al., [138] to simulate the behavior of the SFCL designed in the ECCOFLOW project. Using this model, the quenching action of the SFCL is no longer pre-defined. However, the computational complexity of these models is significantly increased, especially during large scale power network simulations. Hence, during a performance simulation of SFCLs installed in power systems, it is important to study the necessity of considering the thermal and electrical properties of superconducting materials, in order to be able to choose a better trade-off between computational complexity and model accuracy. For any of the adopted strategies, the research must ultimately address the process of finding of the optimal locations for multiple SFCLs inside a power network, which, according to our knowledge, has yet only considered a maximum of just two SFCLs. This means that the cooperation between prospective need for more SFCLs remains an open issue.

In this chapter, we present a comprehensive study of the performance and optimal location analysis of resistive type SFCLs in realistic power systems. We have simulated the performance of SFCLs described by two different models: (i) as a non-linear resistance depending on time, and (ii) as a dynamic temperature-dependent model consisting of the actual E-J characteristics of the superconducting material. The applied power grid model which includes interconnected dispersed energy resources was built based on the UK network standard. Through simulation of the system behaviors under

three fault conditions (two distribution network faults in different branches, and one transmission system fault), the optimum SFCL installation schemes were found from all the feasible combinations of SFCLs. In addition, a detailed comparison between the figures obtained for each of the above cases was performed. The comparison showed that the non-linear resistor model is insufficient for accurate estimation of the reliability and optimal location of an SFCL, as the complex thermal and electrical behaviors of the superconducting material during its transition to the normal state cannot be simplified to a single step-resistance.

4.2 Topology of the Power System and the RSFCL Models

4.2.1 Modelling of the power system based on the UK network standards

The topology of the modelled power system depicted in Figure 4.1 was built based on the UK network standards [139]. The power system has a 120 MVA conventional power plant emulated by a three-phase synchronous machine, which is additionally connected to a local industrial load of 40 MW located 5 km away from the main power plant. Afterwards, the voltage level is boosted from 23 kV to 275 kV by a step-up transformer (TR1), from which the conventional power plant is connected to an upstream power grid rated with a short circuit level of 2 GW through a 130 km distributed-parameters transmission line. Then, the 275 kV high-voltage transmission system is split into two distribution networks. First, after the voltage level being stepped down to 33 kV by substations TR2 and TR4, the upper branch (industrial branch) supplies power to three industrial loads with a rated power of 55 MW, 15 MW, and 10 MW, separately. Likewise, the lower branch (domestic branch) is also connected to two step-down substations TR3 and TR7, with 70 km distance between them. The role of these two substations is reduce the voltage of the lower sub-grid to 33 kV, as it is the same voltage level rated by the interconnected 90 MVA wind power plant. The module

of wind farm emulates the Rhyl Flats offshore wind farm located in North Wales, after being boosted by the step-up substation TR10. This offshore wind power plant is composed of twenty-five fixed-speed induction-type wind turbines each having a rating of 3.6 MVA, and is located 30 km away from its connecting point with the lower distribution network [140]. After integration, the lower branch and the wind farm together provide electric energy to four domestic loads with a rated power of 50 MW, 15 MW, 12 MW and 10 MW, separately. Finally, the industrial branch and the domestic branch are connected through a bus-bar coupler, and the power system is balanced in a way that the current flowing through the bus-tie is only a few amperes during normal operation.

It is generally accepted that a three-phase short-circuit fault provokes the highest fault current among all possible faults, since it will cause the most drastic decrease of the system impedance. In order to ensure safe operation, the maximum current and electrodynamic withstand capabilities of electrical equipment are primarily designed according to this situation. Therefore, it is essential to simulate the behaviour of the power system under three-phase short-circuit fault. The symmetric faults were initialised at three potential locations marked as Fault 1 (132 kV), Fault 2 (33 kV) and Fault 3 (275 kV), which represent prospective faults occurring at the industrial branch, the domestic branch, and the transmission system, respectively (see Figure 4.1). Five positions for the installation of SFCLs were proposed as shown in Figure 4.1, namely at: (i) the integrating point between the conventional power plant and the upstream power grid (Location 1), (ii) the interconnection between the wind farm and the port of domestic branch (Location 2), (iii) the industrial loads branch (Location 3), (iv) the domestic loads branch (Location 4), and (v) the bus-tie coupling the two distribution networks (Location 5).

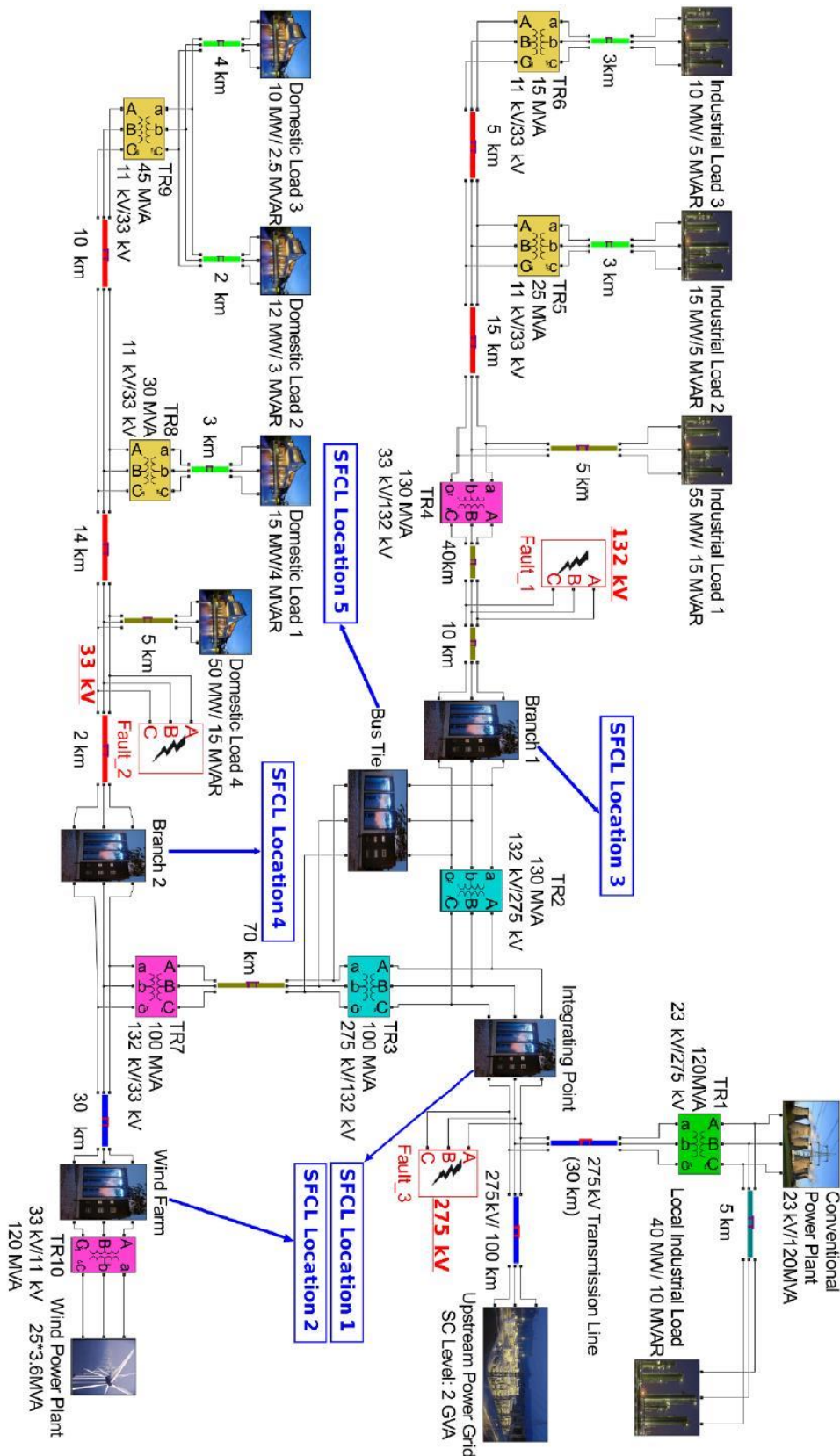


Figure 4.1: The power system model built based on the UK grid standard. Three prospective fault positions and five potential SFCL locations are illustrated.

4.2.2 The step-resistance RSFCL model

As developed and explained in Chapter 3, identical single phase SFCLs were implemented for each one of the three phases of the system, as each phase of the SFCL is only triggered by the current flowing through its own phase. The current limiting performance of the developed step resistance SFCL model is dominated by five predefined parameters: (i) triggering current; (ii) quenching resistance; (iii) quenching time, which has been assumed to be equal to 1 ms in accordance with Refs. [141] and [142]; (iv) a normal operating resistance of 0.01Ω ; and (v) a recovery time of 1 s. The values of the triggering current and quenching resistance are not provided in this section since they vary with the location of the SFCL. The structure of the step resistance model is illustrated in Figure 3.12.

The operating principle of this model has been demonstrated in Section 3.3.2 and can be summarised as follows: first, the SFCL model calculates both the absolute and the RMS values of the flowing current. If both values are lower than the triggering current, the model will consider the SFCL in the superconducting state and insert a normal operating resistance (0.01Ω) into the grid. Otherwise, if either the absolute value or the RMS value of a passing current exceeds the triggering current level, the output resistance will be increased to the quenching resistance after the predefined quenching time. Lastly, if the current flowing through the SFCL model falls below the triggering current due to the clearance of the fault, the SFCL will restore its superconducting state after the recovery time.

4.2.3 The real time E-J power law RSFCL model

In Section 1.5 it was illustrated that the sudden change in the SFCL resistance can be macroscopically simplified into the E-J power law, which can be divided into three sub-regions: the superconducting state defined by $E(T, t) < E_0$ and $T(t) < T_c$, the flux

flow state defined by $E(T, t) > E_0$ and $T(t) < T_c$, and the normal conducting state defined by $T(t) > T_c$, with T_c the critical temperature of the Bi2212 bar, and $E_0 = 1 \times 10^{-6} \text{V} \cdot \text{m}^{-1}$ [137, 143, 144]. All three sub-regions follow different power laws, the combination of which forms the E-J characteristics of the SFCL as follows:

$$E(T, t) = \begin{cases} E_c \left(\frac{J(t)}{J_c(T(t))} \right)^n, & \text{for } E(T, t) < E_0 \text{ and } T(t) < T_c \\ E_0 \left(\frac{E_c}{E_0} \right)^{\frac{m}{n}} \left(\frac{J_c(77\text{K})}{J_c(T(t))} \right) \left(\frac{J(t)}{J_c(77\text{K})} \right)^m, & \text{for } E(T, t) > E_0 \text{ and } T(t) < T_c \\ \rho(T_c) \frac{T(t)}{T_c} J(t), & \text{for } T(t) > T_c \end{cases} \quad (4.1)$$

where

$$J_c(T(t)) = J_c(77\text{K}) \frac{T_c - T(t)}{T_c - 77\text{K}}, \quad \text{for } J > J_c \quad (4.2)$$

When modelling the SC state, we used $n = 9$ in accordance with Refs. [145-148] and $m = 3$ for the flux flow state in good agreement with the experimental data reported in Refs. [149] and [84]. In addition, we have assumed that the normal conducting state resistivity is a linear function of temperature when $T(t) > T_c$, with $\rho(T_c) = 7 \times 10^{-6} \Omega$ for Bi2212 bars [150]. Furthermore, the relationship between the critical current density and the temperature was also set to be linear, as in Equation 4.2, as this has been proven by S. Kozak et al. for the specific case of Bi2212 compounds [151]. To complete the SFCL model, a CuNi alloy ($\rho = 40 \mu\Omega \cdot \text{m}$) resistor was connected in parallel with the superconductor on the basis of the project disclosed in Ref. [152]. This shunt resistance can protect the superconducting material from being damaged by hot spots that develop under limiting conditions, and furthermore prevents over-voltages that may possibly appear if the quench occurs too rapidly [34, 66]. Finally, by assuming that the SC composite is homogeneous, the thermal modelling of the SFCL

considers the first order approximation of the heat transfer between the superconductor and the liquid nitrogen bath is as follows:

$$R_{sc} = \frac{1}{2\kappa\pi d_{sc} l_{sc}}, \quad (4.3)$$

$$C_{sc} = \frac{\pi d_{sc}^2}{4} l_{sc} c_v, \quad (4.4)$$

$$Q_{generation}(t) = I(t)^2 \times R_{SFCL}(t), \quad (4.5)$$

$$Q_{cooling}(t) = \frac{T(t) - 77}{R_{sc}}, \quad (4.6)$$

where R_{sc} stands for the thermal resistance from the SC material to its surrounding coolant, C_{sc} is the specific heat of Bi2212 [153], $c_v = 0.7 \times 10^{-6} J/(m^3 \cdot K)$, and

$$T(t) = 77 + \frac{1}{C_{sc}} \int_0^t [Q_{generation}(t) - Q_{cooling}(t)] dt \quad (4.7)$$

The SC is modelled as a cylindrical wire of length l_{sc} , which is adjusted at each installing location in order to limit the prospective fault current to the desired level. Likewise, the diameter d_{sc} is regulated to ensure that the SFCL not only remains into the superconducting state during normal operation, but also quenches within a few milliseconds once a short-circuit fault occurs at some location on the grid. In practice, although the wire diameter cannot be modified after fabrication, one can connect several wires in parallel to achieve the expected current limiting performance [154], which allows us to use the previous approaches.

4.3 Network Stability, Current Limiting Performance and Recovery Characteristics

In order to compare the fault current limitation properties of the two SFCL models, in Figure 4.2 we present the results for a three-phase to ground fault with negligible fault resistance when it is initialised at the domestic network (Fault 2), and a single SFCL is installed next to the fault position (Location 4). Figure 4.2(a) illustrates that the step resistance model and the E-J power law based model both respond almost simultaneously to the occurrence of a short-circuit fault. However, as the SFCL needs 2 ms to fully quench due to its E-J characteristic and dynamic temperature (Figure 4.2(d)), the first peak reduction gained onto the step resistance model is overestimated by 11 % (7.6 kA and 6.5 kA for the two SFCL models, respectively. 10 kA without SFCL), as shown in Figure 4.2(b). Moreover, since the resistance of the E-J power law model grew with the rise of superconductor temperature, the reduction of fault current achieved by the two RSFCL models gradually became closer. In addition, the shunt resistor diverts the major portion of the fault current after the superconductor develops its normal state (Figure 4.2 (c)). Therefore, the shunt resistance effectively lowers the thermal stress on the HTS wire, simultaneously preventing damages by overheating, whilst the recovery time is reduced [155].

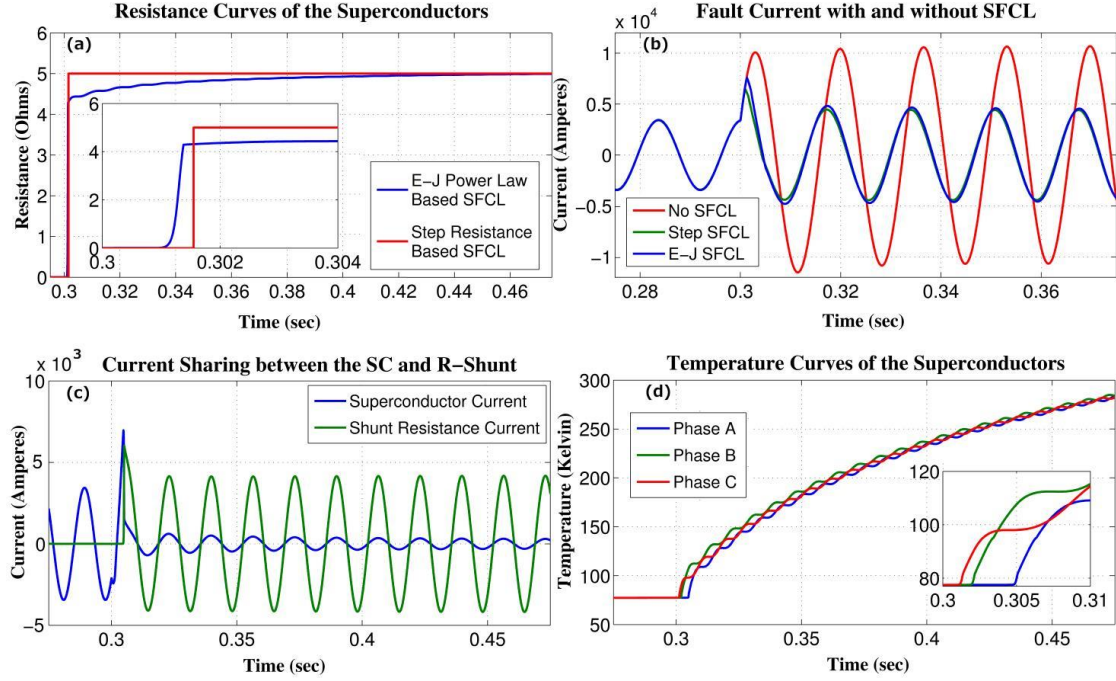


Figure 4.2: Performance comparison between the step SFCL model and the E – J power law based SFCL model: (a) resistance growth, (b) fault current characteristics, (c) current distribution in the SFCL, (d) temperature curves of each phase. The displayed insets in subplots (a) and (d) are measured in the corresponding units of the main plot.

Initial tests without integration of the SFCL model have confirmed that the power system operates at the rated state during normal operation. Then, under occurrence of three-phase to ground faults at Fault-1, Fault-2 and Fault-3 (see Figure 4.1), the short-circuit currents were measured at the integrating point (Location 1), wind farm (Location 2), branch 1 (Location 3) and branch 2 (Location 4). According to analysis given in Section 3.2.2, the instantaneous fault current can be described by:

$$i_k = \underbrace{I_{pm} \sin(\omega t + \alpha - \beta_{kl})}_{\text{periodic component}} + \underbrace{[I_m \sin(\alpha - \beta) - I_{pm} \sin(\alpha - \beta_{kl})] e^{-\frac{t}{\tau_k}}}_{\text{aperiodic component}} \quad (4.8)$$

where I_m is the amplitude of the rated current of the power grid, β and β_{kl} represent the impedance angles before and after the fault, respectively, α defines the fault inception angle, I_{pm} states the magnitude of the periodic component of the short-circuit current, and τ_k stands for the time constant of the circuit. Hence, the fault

currents achieve their maximum values when $\alpha - \beta = \frac{(n+1)\pi}{2}$ with $n \in \mathbb{Z}$. This condition was implemented all through our study in order to consider the most hazardous fault scenarios, and the impact of the SFCLs on the generation side and the voltage stability of the grid. For instance, the response of the output electrical power, rotor speed, and terminal voltage for the conventional power plant (23 kV/ 120 MVA), and the voltage output at the domestic branch (Branch 2) for a scenario in which when a 200 ms three-phase to ground fault is applied at the industrial branch (Fault-1), after 1.2 s within normal operating conditions, as shown in Figure 4.3.

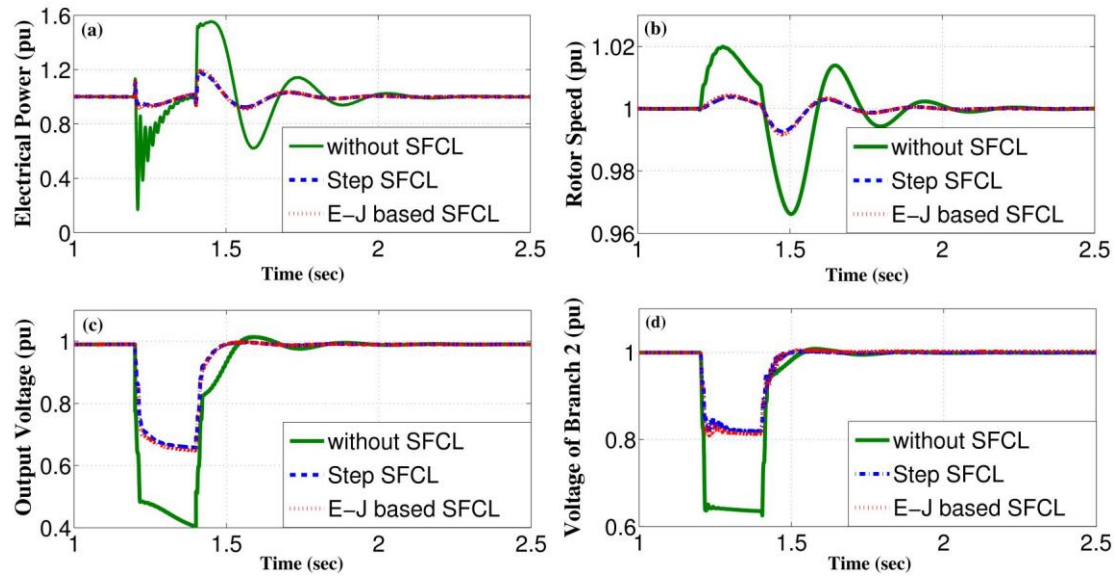


Figure 4.3: Generator parameters and voltages of branch 2 in response to a 200 ms three-phase to ground fault at branch 1.

Initially we have to consider the power system operation without the insertion of SFCLs. Under this scenario, the output electrical power drops sharply to 0.15 pu just after the fault incident (Figure 4.3(a)), whilst the governors of the power plant, such as steam and hydro, still contribute with the same mechanical power to the rotors. Thus, a rapid acceleration of the rotors occurs due to this power imbalance, as shown in Figure 4.3 (b). However, when an SFCL is installed at Branch 1 (Location 1), its high resistance state facilitates the SFCL to dissipate the excess generator power during the fault condition, hence improving the energy balance of the system and effectively

reducing the variation of the rotor speed. Furthermore, considering the conventional equal-area criterion for stability issues [141, 156], the SFCL could improve the damping characteristics of generator speed and system frequency, as well as the system current, because the insertion of high resistance into the grid would significantly increase the damping ratio. Moreover, due to the short-circuit fault of Branch 1, a sharp voltage drop (Figure 4.3 (c) - (d)) can be seen at both the power plant terminal (0.5 pu) and the non-faulted Branch 2 (0.35 pu). Then, by introducing the SFCL, which acts as a voltage booster, the observed voltage dips are mitigated by 40 % and 50 %, respectively. This improvement allows the healthy parts of the system (without the fault inception) to be less affected, and makes integration of an SFCL a reliable fault ride-through scheme.

Without the protection of the SFCL, a 200 ms short-circuit fault was initiated in Branch 1 (Fault 1) in order to study the relationship between the current limiting performance of an SFCL and the maximum normal resistance. First, without the protection of the SFCL, simulation results have shown that the first peak of the current flowing into Branch 1 reached ~ 3.8 kA, which is ~ 6.8 times higher than the rated value (560 A). Then, after installation of the SFCL, a considerable reduction of the fault current was observed as shown in Figure 4.4. The insets (a) and (b) on this figure illustrate the variation of the limited current when the two SFCL models (step resistance, and E-J-T power law) were integrated at Branch 1 (Location 3).

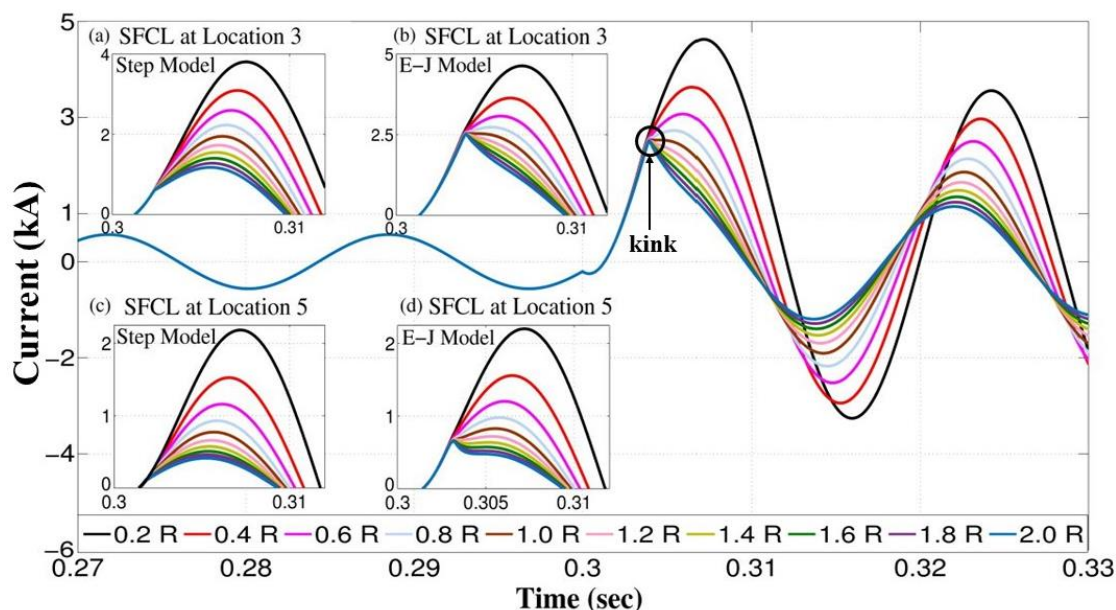


Figure 4.4: Current curves of phase A under a branch 1 fault (Fault 1) when the SFCL resistance increases from 0.2 R to 2.0 R.

For the step-resistance model, with the SFCL resistance increasing from 0.2 R to 2 R ($R = 30 \Omega$) during the quenched state, the peak value of the fault current gradually decreased from ~ 3.8 kA to ~ 1.2 kA, showing a small displacement of the peak values. However, in the case of the E-J-T power law model, a noticeable *kink* appeared at 2.5 kA, when the maximum resistance of the SFCL was greater than 1 R. Remarkably, this distinctive *kink* can be interpreted as the threshold value for the maximum reduction of the fault current for an SFCL which cannot be determined with any other model, to the best of the knowledge of the authors. To illustrate the difference, the step-model resistance predicts a continuous decrease on the first peak of the fault current as R increases (Figure 4.4 (a) & (c)), contrary to what is observed with the more realistic E-J-T model (Figure 4.4 (b) & (d)), which predicts that no matter the increment of the SFCL resistance, after a certain value it can only limit the first peak of the fault current to a well-defined threshold. For instance, for the case illustrated in Figure 4.4, we have determined that on the instant that the *kink* appears, the current curves overlap at about 2.5 kA, defining hence, the maximum peak reduction of the fault current at this location (Location 3), and therefore an optimal SFCL resistance. It

is worth mentioning that the characteristic kink is also observed when the SFCL is located at any other position, e.g., at the bus-tie (Figure 4.4(c) & (d)), which validates the generality of our statement. Thus, in terms of economic considerations, it represents a very valuable result for distribution operators as it allows to state a maximum threshold on the required size for the capacity of the SFCL, minimizing material investments for specific locations as beyond this threshold no further reduction of the first peak of the fault currents can be achieved.

Although the passive transition of the SC material and the high normal resistance enables the SFCL to limit the fault current before attaining its first peak, in some cases the recovery characteristics of the SFCL need to be improved because the SC may need several minutes to restore its superconducting state under load conditions. For instance, if a fault event quenches a single SFCL located at the domestic branch, it may take more than 300 seconds to recover once the fault current has been cleared.

Therefore, in order to decrease the recovery time of the SFCL we have connected a bypass switch parallel to both the SC and the shunt resistance [157]. Thus, when the SFCL can quickly recover the superconducting state under load conditions, the switch $S1$ remains closed after the fault is cleared. However, if the SFCL cannot be automatically recovered within a few seconds, then switch $S2$ can be closed and switch $S1$ instantaneously opens to quickly disconnect the SC from the system. This allows the SC to undergo its recovery process without further accumulation of heat, as shown in Figure 4.5 for an SFCL installed at Location 2 after encountering a 0.2 s three-phase to ground fault at the domestic branch (Fault 2).

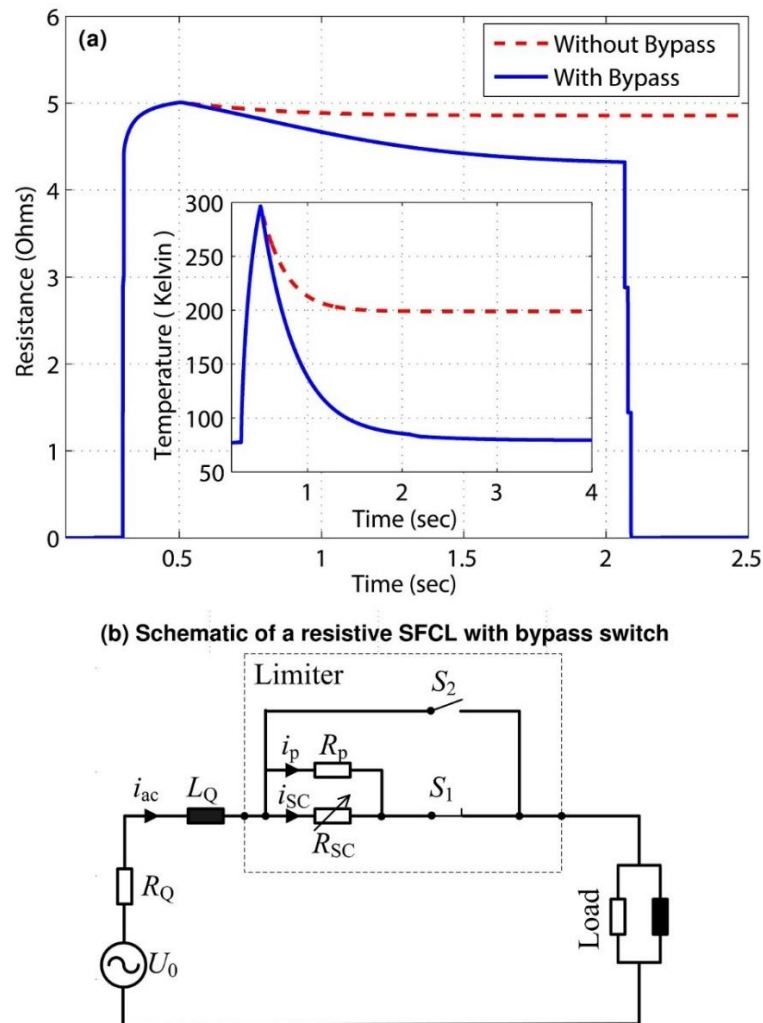


Figure 4.5: SFCL resistance and temperature dynamics with and without the assistance of the Bypass switch strategy shown in the bottom of the figure.

For this case, and without applying the bypass switch strategy, a certain amount of current will continue passing through the SFCL after the clearance of the fault. This flow of current keeps continuous to generate heat inside of the superconductor, which significantly slows down the decrease of temperature, and hence delays the recovery of the SFCL by over five minutes. However, with a properly designed control scheme, the E-J-T model can open the switch S_1 and close the switch S_2 at the moment that the fault ends, thus transferring the current to the S_2 branch. In fact, by using this method we have determined that the recovery time can be reduced to less than 1.6 s without affecting the normal operation of the power grid. After the SC is restored to its

superconducting state, the switches $S1$ and $S2$ act again to prepare the SFCL for the next fault. However, as it is not possible to foresee the location of a fault event, the optimal location for the installation of one or more SFCLs has to be assessed, being this the purpose of the following section.

4.4 Identification of the Optimal Location

In order to attain an accurate estimation of the optimal location for the installation of one or more SFCLs, all possible SFCL combinations according to the five proposed locations depicted in Figure 4.1, were analysed for the three different fault points. This resulted in a total of 31 allocation strategies, including five different schemes for the integration of a single SFCL (Locations 1 to 5), 10 dual combinations of SFCLs, 10 further combinations of three SFCLs, five combinations of four SFCLs, and finally the cooperation between all five SFCLs.

The current signals at both the wind farm terminal (Location 2) and the integrating point of the conventional power plant and the upstream power grid (Location 1) were measured for all three fault conditions (Figure 4.1). We also analysed the current injection of the industrial branch (Location 3) and the domestic branch (Location 4) when faults happen at the two networks: Fault 1 and Fault 2, respectively. For the sake of brevity, we do not present the results for the measured current at the industrial branch when Fault 2 or Fault 3 occurs, because based on the analysis of the system impedance change, the magnitude of the current flowing into the industrial branch is actually reduced by the two faults to levels lower than the normal current, i.e., at this point the SFCL does not need to be triggered to protect this branch. The same argument applies to the domestic branch under Fault 1 and Fault 3 conditions. Our results are presented below in terms of the single or multiple SFCL strategies. The optimal SFCL installation scheme was found by following the algorithm shown in Figure 4.6.

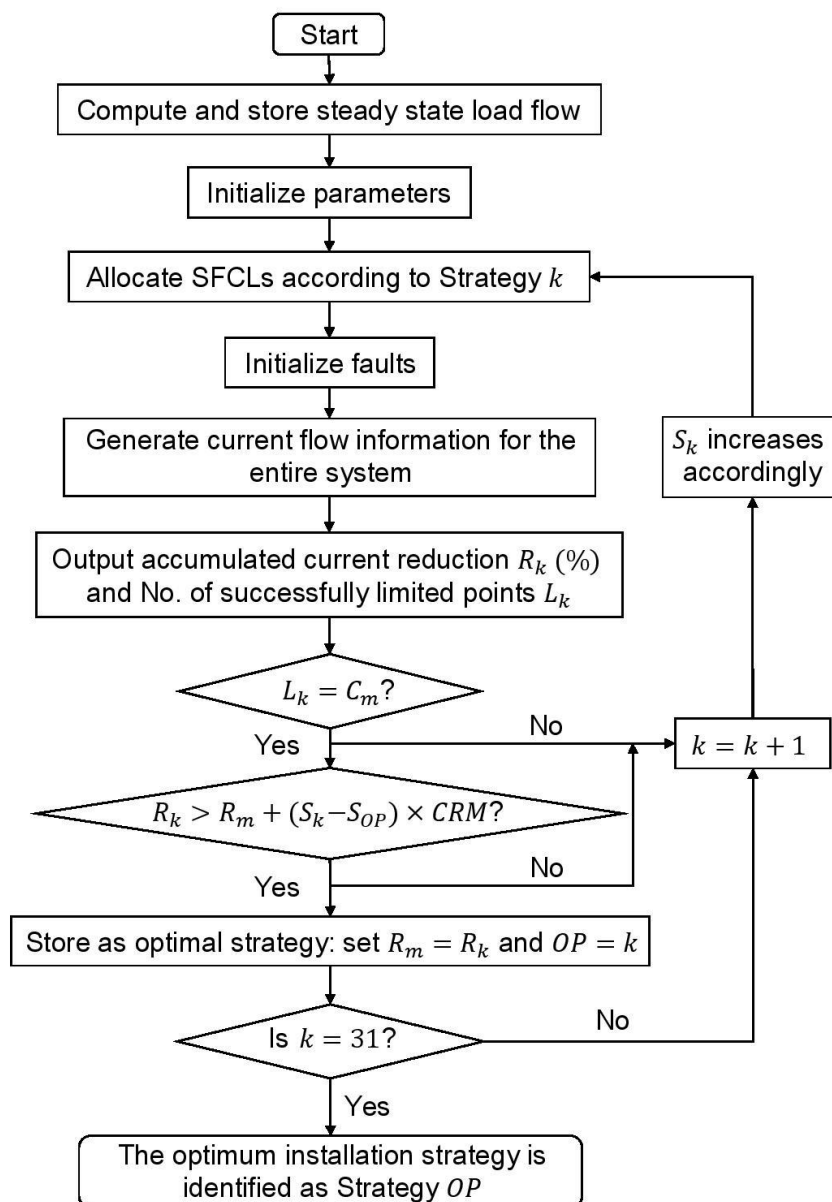


Figure 4.6: Flowchart of the algorithm for determining optimal installation strategy of SFCLs. Parameters being initialized during the third step: number of $k = 1$; number of installed SFCL $S_k = 1$; maximal current reduction $R_m = 0$; current reduction margin of one additional $SFCL = CRM$; number of measured points C_m ; optimal strategy $OP = 0$.

4.4.1 Single SFCL installation

Figure 4.7 shows the reduction in the fault current under the three fault conditions illustrated in Figure 4.1 when a single SFCL is installed at the referred locations

(Locations 1 to 5). In Figure 4.7 and the following three figures, the meaning of the abbreviations in the legends is summarized in Table 4.1.

Table 4.1 Legend meanings for Figure 4.7 to Figure 4.10.

F1-WF/ F2-WF/ F3-WF	Reduction in first peaks measured at the wind farm under Fault-1/ Fault-2/ Fault-3.
F1-IP/ F2-IP/ F3-IP	Reduction in first peaks measured at the integrating point under Fault-1/ Fault-2/ Fault-3.
F1-B1	Reduction in first peaks measured at the Branch 1 (industrial branch) under Fault-1.
F2-B2	Reduction in first peaks measured at the Branch 2 (domestic branch) under Fault-2.

For the sake of comparison, the size of the superconductor which has to be defined into the E-J-T power law model, was systematically adjusted so that it defined the same maximum resistance as the one used with the step resistance model. Thus, when the step resistance model was considered, the maximum reduction of the fault current was overestimated in comparison with the more realistic E-J-T model. For all five SFCL locations, the first peak of the fault current was always found to be lower in the first case. The reason for this difference is that, once the current exceeds the critical value of the SC, the SFCL described by the step resistance model directly jumps to the maximum resistance after the pre-defined response time, whilst in the E-J-T model the dynamic increase of the resistance depends not only on the passing current, but also on the temperature of the superconductor. Therefore, under the E-J-T model the SFCL cannot gain its maximum rated resistance before the first fault peak is reached, which leads to a relatively lower reduction of the fault current (~20%).

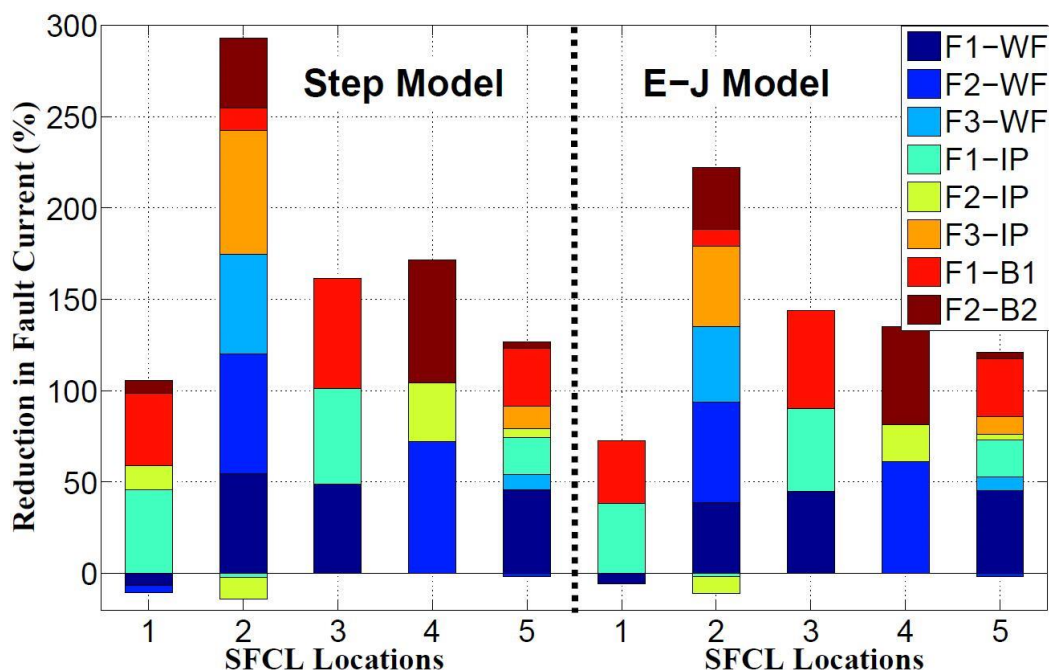


Figure 4.7: Reduction in first peaks of fault currents achieved by single SFCL installed at different locations of the power system.

Based on both the SFCL models tested, the simulations performed generally showed a negative impact on the reduction of the fault peak at certain integration points when the SFCL was installed at Location 1 or Location 2. In these cases, the fault current was actually increased by the insertion of a SFCL. In more detail, when the SFCL was installed beside the wind farm (Location 2), the sudden increase in the fault current flowing through the integrating point under Fault 2 (at the domestic branch) was caused by the abrupt change of the impedance of the power system. This SFCL entered the normal state, reducing the current output of the wind farm due to its rapid rise in resistance and hence, the conventional power plant and the upstream power grid were forced to supply a higher current to the faulted branch. Similar behavior was obtained under the fault conditions F1 and F2 when the SFCL was installed at Location 2, and the current was measured at the integrating point (see Figure 4.7 & Figure 4.1). Furthermore, when a single SFCL was installed at Location 1 (integrating point), following the E-J-T model the SFCL can only limit the fault current in two cases, whilst with the simplified step-resistance the benefits of the SFCL can be overrated as it leads

to a positive balance in up to four different fault conditions. This highlights the importance of finding a suitable optimal allocation strategy for the SFCLs under a wide number of fault conditions, and the need for considering adequate physical properties for the electro-thermal dynamics of the SC materials. It ultimately tries to fill the gap between the acquired scientific knowledge and the demand for more reliable information from the standpoint of the power distribution companies. Thus, the final decision for an optimal location has to be made under the circumstance of having a twofold conclusion.

Firstly, the decision can be made according to the highest total reduction on the fault current passing through different points and under different fault circumstances as shown in Figure 4.7. There, it can be observed that for the eight most important cases combining the occurrence of a fault at certain positions and the measuring point for the current reduction, the SFCL installed at the port of the wind farm (Location 2) appears to be the best option, as in this case the fault current can be reduced in six of the eight different scenarios with an accumulated reduction of 290% from the step resistance model, and 220% from the E-J-T power law model, respectively. Nevertheless, this strategy has also an adverse impact on the remaining two other scenarios (F1-IP & F2-IP). Secondly, a decision can be made in terms of the overall performance for achieving positive impacts under the scope of any of prospective circumstances. In this sense, we have determined that placing the SFCL at Location 5, at the bus-tie between the industrial and domestic branches, is the most reliable option. An SFCL installed at the bus-tie is capable of reducing the harmonics and voltage dips, doubling the short-circuit power, and ensuring even loading of parallel transformers [158]. Moreover, the recovery characteristics of the SFCL can also see benefit from this arrangement as after a quench of the SFCL, the bus-tie can be switched open for a short time (few seconds) to help the SFCL restore the superconducting state. However, a drawback of this

switching strategy is that this measure may temporarily reduce the quality of the power supply, but a strong impact on the normal operation of the power system is not foreseen.

4.4.2 Multiple installation of SFCLs

Firstly, a double protection strategy, the installation of two SFCLs in different grid positions, was assessed. According to both the step resistance model and the E-J power law based model, the highest fault current reduction was always achieved when the SFCLs were installed at Location 2 (wind farm) and Location 3 (industrial branch) simultaneously, accomplishing a 400% and 330% total fault limitation, respectively, as shown in Figure 4.8.

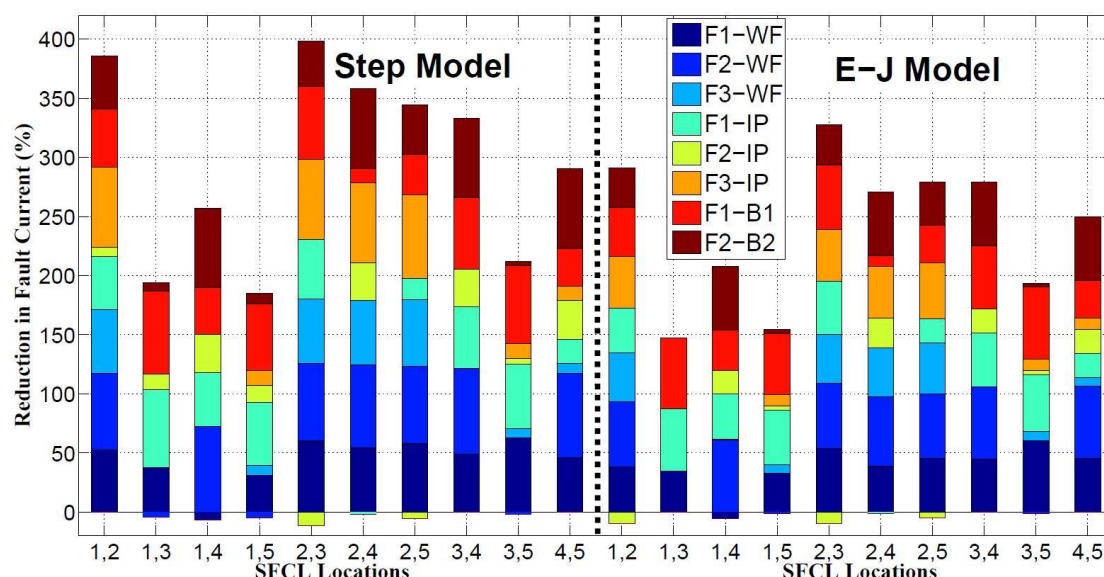


Figure 4.8: Reduction in first peaks of fault currents achieved by different combinations of dual SFCLs.

Indeed, this arrangement can be considered a much better strategy in comparison to the results obtained when just a single SFCL was considered, as the total current limitation is improved by around 110%. Furthermore, contrary to the previous case, the current flowing through the integrating point when the fault occurs at the industrial branch (Fault 2) significantly decreased rather than having an adverse effect on the

power system. Moreover, unlike the results obtained by installation of a sole SFCL, with this dual strategy the measured current reduction showed a balanced performance on all the different analysed cases.

If system operators measure the optimal strategy for the installation of two SFCLs in terms of the number of limited cases, different conclusions can be obtained under the framework of different physical models, e.g., when the step-resistance or the E-J-T power law model is considered. According to the step resistance model, installing the two SFCLs at either Locations 1 & 2 or Locations 4 & 5 produced a positive response to all eight measured fault conditions. When the SFCLs were installed at Locations 1 & 2, a better performance was obtained as the total reduction in the fault current (330%) was 40% greater than the performance obtained by SFCLs installed at Locations 4 & 5 (290%). However, when the E-J-T model was used, installing the SFCLs at Locations 1 & 2 increased the magnitude of the current at the integrating point under the occurrence of a fault in the domestic branch (Fault 2). This was due to the unsuccessful triggering of the SFCL at Location 1, as explained in the previous subsection. Therefore, from the point of view of the system operators, Locations 4 & 5 can be considered as the most reliable solution as it is the only combination capable of limiting all fault conditions and for all the considered scenarios.

Secondly, we added an additional SFCL to the grid to assess the overall performance of this new system. Most of the installation strategies for three SFCLs produced a reduction of the fault current in all eight measured scenarios, as can be seen from Figure 4.9.

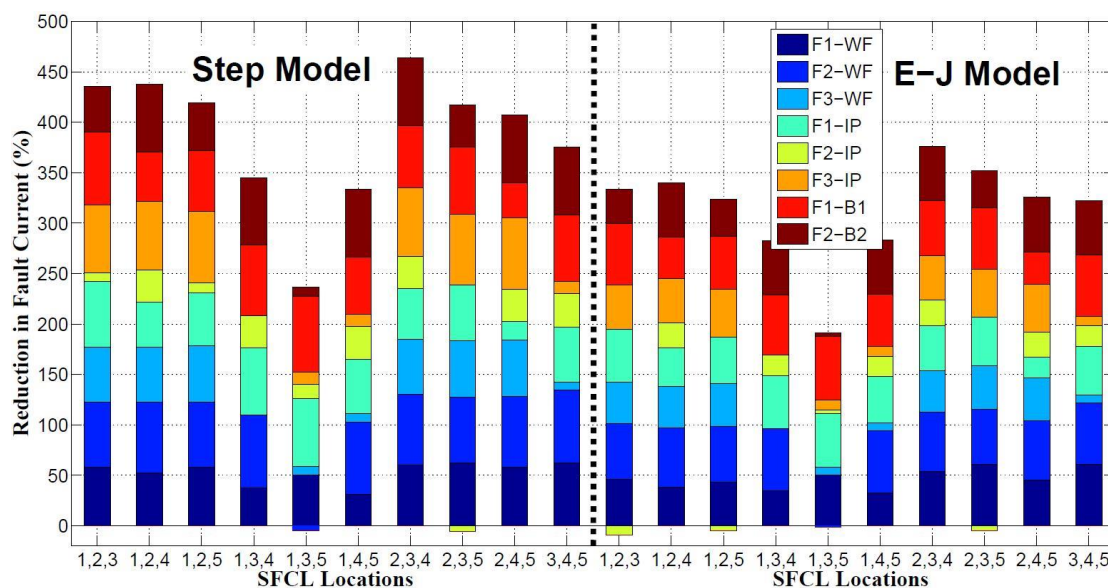


Figure 4.9: Total reduction in first peaks of fault currents achieved by different combinations of three SFCLs.

Both SFCL models agreed with the conclusion that the greatest reduction in the fault current was achieved when the SFCLs were installed simultaneously at the Locations 2, 3 and 4. This strategy showed a 470% total reduction using the step resistance model, and 375% using the E-J-T model, attaining a significant increase on the overall performance of the system by about 70% and 45%, respectively, in comparison with the best achieved performance when the dual SFCLs strategy was considered. Besides this huge improvement, the three SFCLs strategy could also respond positively to any fault conditions, which means installing three SFCLs can be considered the most reliable strategy for both overall fault current reduction and the number of cases exhibiting fault current reduction. Moreover, it was found that, under all fault conditions, the fault current levels of all measured points can be reduced to lower than the safety thresholds, which was set as three times of the normal current according to common practice. Until a significant reduction of the overall price of a SFCL is achieved, distribution network operators may not consider this strategy to be cost-effective in terms of the initial investment, but given the expected reduction on the price of the second generation of high temperature superconducting wires, this decision can

be seen as the most profitable strategy in terms of grid safety and reliability. However, a limit for the maximum number of the SFCLs required must also be established in order to guarantee the maximum benefits at minimum cost.

Thus, in Figure 4.10 we show the performance comparison among five different scenarios when four SFCLs were installed into the power system. With four SFCLs working together, all of the combinations effectively limited the fault current for all eight studied cases, except for when the SFCLs were described using the E-J-T model and installed at Locations 1, 2, 3, and 5. Under this scheme the measured fault current increased when the fault was initialised at the domestic branch (Fault 2), due to the lack of action from the SFCL installed at Location 1. When the step resistance model was considered, the accumulated maximum reduction on the fault current was again overestimated, achieving a 480% reduction when the SFCLs were installed at Locations 1,2,3 and 4 or at 2,3,4 and 5. In comparison, Locations 2,3,4 and 5 produced a prospective reduction of 395% when the more realistic E-J-T model was considered. The maximum accumulated reduction of the fault current achieved by any of the strategies using four SFCLs was just over 10% more than the most effective of the strategies using three SFCLs. This enables us to define an upper limit for the number of SFCLs needed.

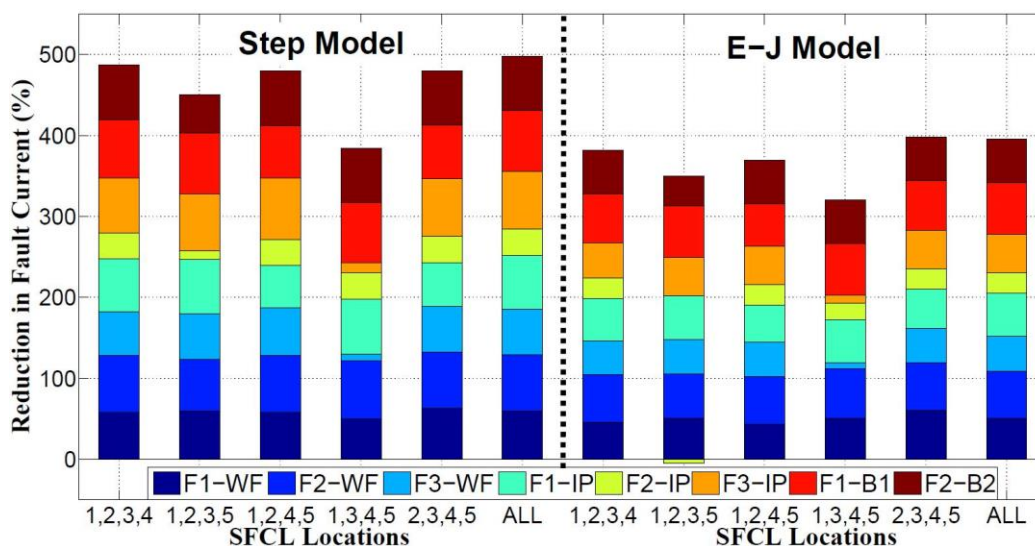


Figure 4.10: Total reduction in first peaks of fault currents achieved by different combinations of four and five SFCLs.

In order to verify our previous statement, we also studied the result of considering even one more SFCL, as there are five prospective locations for SFCL installations in the power grid displayed in Figure 4.1. Compared to the last analysed case (4 SFCLs), the accumulated maximum reduction of the fault current reached a 15% greater reduction when the SFCLs were simulated using the step resistance model, but surprisingly no further improvement was obtained when the more realistic E-J-T model was incorporated. This important result can be understood as a consequence of the mutual influence between the integrated SFCLs, i.e., when the fault current passing through one SFCL is substantially decreased by the influence of the others, the rate of heat accumulation reduces accordingly, slowing down the rate of the temperature rise and hence reducing the resistance that the SFCL can develop before reaching the first peak of the fault.

Table 4.2 summarizes the optimal allocation strategies and the corresponding performances of the SFCLs modelled during our study. The preferable locations for the installation of the SFCLs have been determined in terms of the two identified standards: (i) the maximum accumulated fault current reduction, and (ii) the maximum number of

measuring conditions that could be limited. The results in the table are categorised by the number of SFCLs required by each strategy, and also the physical models used to emulate the characteristics of the SFCLs. In all the cases, the step resistance model led to an overestimation of the actual performance figures achievable by the SFCLs when more realistic physical properties were considered. Finally, when the strategy is to maximize the benefits from installing only one or two SFCLs, a compromise must be made between increasing the fault current reduction, and maximizing the actual number of measuring conditions where the fault current can be limited. Therefore, based upon the comprehensive study presented in this paper, we conclude that the optimal installation strategy is the installation of a maximum of three SFCLs at Locations 2, 3, and 4, as this strategy produced the maximum reduction of the fault current for all fault conditions, and the addition of further SFCLs did not represent a significant enough improvement to justify the increased cost.

Table 4.2: Optimal installation strategies for SFCLs according to the step-resistance and E – J power law models.

Step-Resistance Model					
<i>Maximum Accumulated Fault Current Reduction (%)</i>	290	400	470	480	495
No. of measuring conditions with/without FCR	6/2	7/1	8/0	8/0	8/0
Number of installed SFCLs	1	2	3	4	5
SFCLs' Locations	2	2,3	2,3,4	1,2,3,4 ^a	1,2,3,4,5
<i>No. of measuring conditions with/without FCR</i>	7/1	8/0	8/0	8/0	8/0
Accumulated FCR (%) for Max. No. of measurements	130	330	470	480	495
Number of installed SFCLs	1	2	3	4	5
SFCLs' Locations	5	1,2	2,3,4	1,2,3,4	1,2,3,4,5
E-J Power Law Model					
<i>Maximum Accumulated Fault Current Reduction (%)</i>	220	330	375	395	395
No. of measuring conditions with/without FCR	6/2	7/1	8/0	8/0	8/0
Number of installed SFCLs	1	2	3	4	5
SFCLs' Locations	2	2,3	2,3,4	2,3,4,5	1,2,3,4,5
<i>No. of measuring conditions with/without FCR</i>	7/1	8/0	8/0	8/0	8/0
Accumulated FCR (%) for Max. No. of measurements	120	250	375	395	395
Number of installed SFCLs	1	2	3	4	5
SFCLs' Locations	5	4,5	2,3,4	2,3,4,5	1,2,3,4,5

The maximum Fault Current Reduction (FCR) value (per case) has been calculated as the sum of the percentage reductions of the fault current measured at the wind farm output, the integrated point, and branches 1 and 2, for the three fault conditions shown in Figure 4.1. The fault current was not reduced at all measuring locations, as shown in Figures 4.7 to 4.10. Therefore, the table also shows the values for the accumulated fault current reduction when the fault current was reduced for the greatest number of measuring conditions.

^a Same performance is achieved when the four SFCLs are located at the positions 2, 3, 4 and 5.

4.5 Comparison between Behaviours of the Exponential-Resistance and E-J Power Law RSFCL Models

In Sections 4.2 to 4.4, modelling of the real-time RSFCL behaviour based on E-J power law was introduced, and the performance comparison between the step-resistance model and E-J power law model was simulated and presented. Moreover, the optimal locations of RSFCLs for the studied power system model were determined according to two different standards: the maximum percentages of fault current reduction, and the maximum number of protected positions. The simulation results showed that, using a predefined step resistance to describe the RSFCL characteristics is preferable for demonstration of current limiting function of the RSFCL, or performance simulation in simple power system models. But with the increase of system complexity, the drawbacks of this simplification can be magnified and lead to wrong conclusions.

It was mentioned in Section 4.1 that two simplified models were frequently used in simulations of RSFCLs, the step-resistance model and the exponential descriptive equation model. Intuitively, we would assume the exponential model shares the same inaccuracy with the step model since it also relies on predefined parameters such as quench time, quench current and normal resistance. However, this hypothesis needs to be confirmed. In addition, there is another widely used safety criterion of the power system which remained to be applied for the determination of the optimal allocation strategy of RSFCLs. The safety criterion refers to three times of the nominal current [158]: the system is considered under control if the fault current across the entire grid can be limited below this threshold by RSFCLs.

In this section, a brief performance comparison between the exponential descriptive equation model and the E-J power law RSFCL model is conducted in a different power

grid model. Moreover, a new approach for determining optimal locations of RSFCLs is demonstrated. Development of various methods for identifying optimal locations of RSFCLs is in the favour of power system operators, since they can choose the right strategy according to their practical demands.

4.5.1 The power system and RSFCL models

Similar to the previously studied power grid (see Figure 4.1), the simulated system in this section is also designed according to the UK network standards [139], and is represented by the single-line diagram, as shown in Figure 4.11. The power system includes a 200 MVA conventional power plant connected to a 2 GVA short circuit rated upstream power grid which supplies an interconnected 80MW industrial load (IL1). Then, the power flow continues downwards to feed domestic and industrial networks, characterised by three domestic loads (DL1–DL3) and four industrial loads (IL2–IL5) (see also Table 4.3). Distributed renewable energy systems such as onshore wind power plants have also been considered under the scope of the simulated power system. For the case study presented in this manuscript, the wind power plant has been simulated in accordance with the power specifications provided by the Phase II Crystal Rig wind farm in East Lothian, Scotland, giving a nameplate capacity of 138MW (60 Siemens 2.3MW turbines).

Table 4.3: Parameters of the loads, transformers and transmission lines.

Loads (MW)		Transformers (MVA)		Transmission lines (km)			
DL1	20	TR1&2	250	L1&8	4	L11	12
DL2	30	TR3&5	220	L2	70	L12	2
DL3	50	TR4&6	200	L3&4	20	L13	1
IL1	80	TR7	120	L5	30	L14	6
IL2	70	TR8	180	L6	80	L15	5
IL3	55	TR9	40	L7	10	L16	15
IL4	30	TR10	60	L8	1	L17	4
IL5	30	TR11	90	L9	10	L18	2

By considering the most hazardous scenarios for the operation of the system, three prospective locations were simulated for three-phase to ground short circuit events representing contingencies at the domestic network (Fault 1), the industrial network (Fault 2), and the high voltage transmission lines (Fault 3). For protecting the system under the three fault conditions, following five locations have been assumed to be the most suitable integration points for the installation of an SFCL: the outgoing feeder of the conventional power plant (SFCL 1), the outgoing feeder of the wind farm (SFCL 2), the ports of the domestic (SFCL 3) and industrial (SFCL 4) branches, and the bus-tie coupling the domestic and industrial networks (SFCL 5).

sections 4.2.3, which left the exponential RSFCL model to be explained. Once the exponential SFCL model detects the occurrence of a fault event, its nominal resistance $R(t)$ swiftly increases towards the maximum resistance of the quenched material until the clearance of the fault is achieved, i.e.

$$R(t) = R_m \left[1 - \exp\left(-\frac{t - t_f}{t_{sc}}\right) \right], \in \text{Fault time} \quad (4.9)$$

where R_m stands for the maximum resistance of the SFCL, t_f represents the moment of the fault occurrence, and t_{sc} defines the minimum quench time required by the propagation of the normal zone over the entire superconductor (~ 1 ms).

4.5.2 Performance analysis of the RSFCL models

The differences in current limiting performance of the three RSFCL models can be seen from Figure 4.12, which illustrates the current responses to a 200 ms domestic branch fault (Fault-1 in Figure 4.11) when the system was equipped with an RSFCL at location SFCL-3. After fault initialized at $t_f = 0.5$ s, the first peak of the prospective fault current 6 kA is effectively limited to 2.7 kA when the exponential model is considered, i.e., attaining a 55% reduction on the first peak of the fault current, whilst only about a 35% current reduction is achieved with the temperature-dependent E-J power law. This result indicates that although the simplified exponential resistance model can overestimate the rate of change for the resistance curve of the SFCL, the minimum rated resistance for fault protection, R_m , can be estimated based on the exponential model if the minimum percentage of current reduction is defined. This value can therefore be used as a control asset for defining the actual impact of the SFCL protection scheme when considering more sophisticated models like the temperature dependent E-J power law.

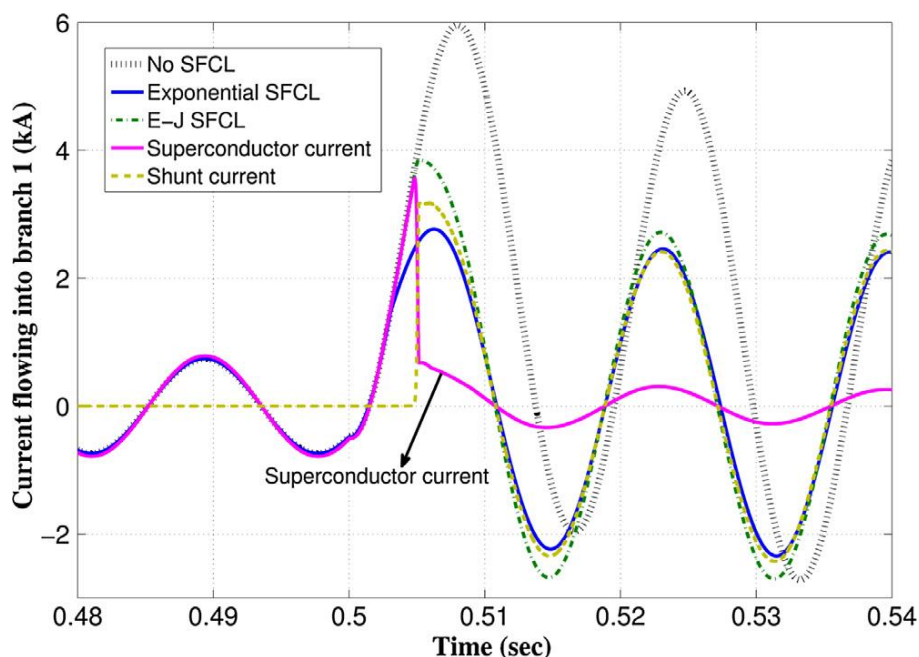


Figure 4.12: Fault-current limiting dynamics of SFCL-3 responding to Fault-1. The current sharing profile between the SC and the shunt resistance of the E-J power law SFCL model is also displayed.

After the full clearance of a fault event lasting a few tens of milliseconds, the SFCL may require several minutes to recover its SC properties. This feature compromises the deployment and reliability of the SFCL protection scheme. However, as stated in Section 4.3, by connecting a bypass switch (BS) parallel to the terminals of the SFCL, the recovery time of the SFCL can be decreased to less than 3 s regardless of the SFCL position and the fault location. The BS enables the electrical isolation of the SFCL from the power grid after the clearance of faults, hence reducing the Joule heating on the SC material and therefore its recovery time t_r . Another advantage of the BS scheme is that it allows the automatic reconnection of the SFCL to the live power grid once the SC state is recovered. The comparison of recovery time of RSFCLs with and without bypass switches is shown in Table 4.4.

Table 4.4: Calculated recovery time t_r of the SFCLs depicted in Figure 4.11 without (-) and with (*) the assistance of bypass switches.

	Fault 1(-)	Fault 1(*)	Fault 2(-)	Fault 2(*)	Fault 3(-)	Fault 3(*)
SFCL 1	329s	0.71s	N/A	1.55s	370s	0.73s
SFCL 2	482s	1.34s	529s	N/A	559s	1.63s
SFCL 3	320s	0.87s	N/A	2.11s	N/A	N/A
SFCL 4	N/A	N/A	729s	0.80s	N/A	N/A
SFCL 5	1.01s	0.87s	0.82s	N/A	0.79s	0.77s

4.5.3 Optimal installation strategies of the RSFCLs

After the analysis of current limiting performance and the simulation of BS-assisted recovery characteristics, the reliability analysis for the overall protection of the power grid lies in the accurate assessment of the optimal number and locations for SFCLs. Therefore, in order to determine the optimal installation strategy, and thereby ensure the overall protection of the power grid under diverse fault conditions, a set of five installation points were chosen after analyzing the capability of each individual SFCL by limiting the fault current to within the rating of existing switchgears. The optimal SFCL protection scheme is determined from the power flow analysis of the 31 possible strategies, s , that combine the five SFCL locations (see Table 4.5). Each strategy was assessed under all three fault conditions illustrated in Figure 4.11, resulting in the study of 93 different cases.

By scrutiny of the most hazardous fault events in each of the aforementioned 93 cases, Figure 4.13 shows the obtained results for the reduction of the first peak of the fault current from the analysis of the 31 protection strategies. In particular, we refer to the measuring points located at (see Figure 4.11): (a) the integration point (IP) with a fault event at the domestic network (Fault 1), (b) the IP with a fault event at the high voltage transmission line (Fault 3), (c) the domestic branch connection (DBC) with a fault event

in the domestic network (Fault 1), and (d) the industrial branch connection (IBC) with a fault event in the industrial network (Fault 2).

Table 4.5: Table of protection strategies, s , accounting for the deployment of up to five SFCLs.

s	SFCLs	s	SFCLs	s	SFCLs
1	1	11	2, 4	21	1, 4, 5
2	2	12	2, 5	22	2, 3, 4
3	3	13	3, 4	23	2, 3, 5
4	4	14	3, 5	24	2, 4, 5
5	5	15	4, 5	25	3, 4, 5
6	1, 2	16	1, 2, 3	26	1, 2, 3, 4
7	1, 3	17	1, 2, 4	27	1, 2, 3, 5
8	1, 4	18	1, 2, 5	28	1, 2, 4, 5
9	1, 5	19	1, 3, 4	29	1, 3, 4, 5
10	2, 3	20	1, 3, 5	30	2, 3, 4, 5
				31	1, 23, 4, 5

The extensive set of results derived from this study can be simplified by calculating the operational safety margin (OSM) for each one of the 31 protection strategies, i.e., $OSM = (I_{sr} - I_l)/I_{sr} \times 100\%$, with I_l being the magnitude of the first peak of the limited current, and the safety threshold $I_{sr} = 3I_n$ (see Figure 4.13). Thus, when the protection strategy produces a positive impact on all the measuring points, the strategy is considered to be highly suitable, and eventually it can be considered optimal depending on the specific demands of the power industry. In the presented case, if the effectiveness of a protection strategy that assumes a k -number of SFCLs is within 10% of the effectiveness of any of the other protection schemes with $k - 1$ SFCLs, the last is considered to be the optimal protection scheme. The overall algorithm for identification of the optimal protection scheme is illustrated in Figure 4.14.

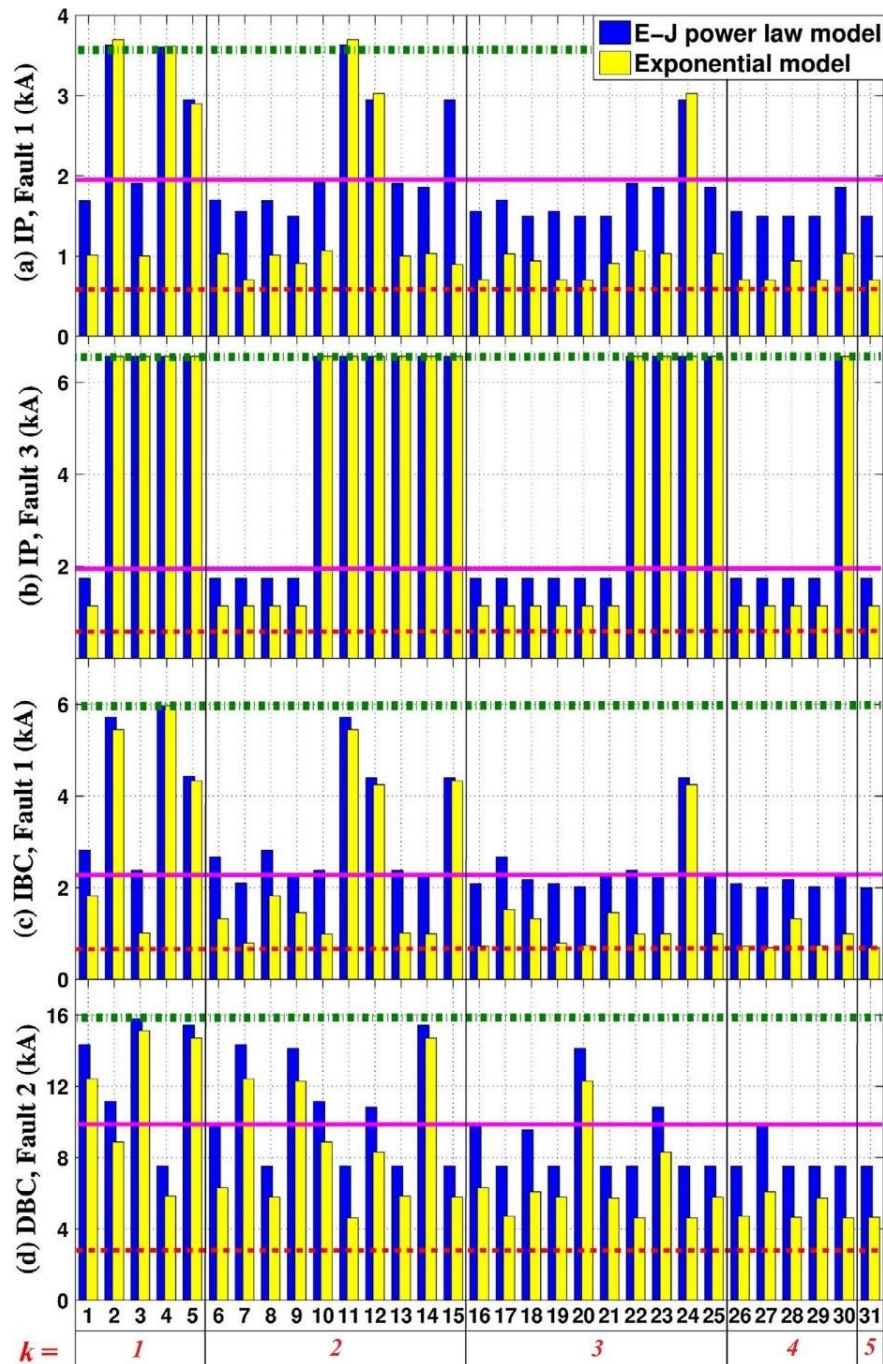


Figure 4.13: First peak limiting performance of the 31 installation strategies. Results are shown only for the most hazardous measurement conditions identified during the analysis. The green dash-dotted lines show the prospective fault current levels without the SFCLs. The red dashed lines represent the current levels for the normal operation of the power grid (I_n), and the threshold value for safety regulation (I_{sr}) is defined as three times this value (purple solid lines) as common practice.

In all cases, the fault has been initiated after 25 cycles of normal operation ($t_f = 0.5s$), with a duration of 10 cycles ($t_{fc} = 0.5s$), and the computation has been carried

up to $t = 4s$ which is generally greater than $t_{fc} + t_f$ when the BS has been included. For the installation of only one SFCL $k = 1$, the mean computing time for the subset of strategies $s \in [1:5]$ is $\sim 58 \pm 5s$ regardless of the location of the fault, with an average increment of $\sim 18s$ for each strategy with an added SFCL ($k + 1$). The actual total computing time for the 93 studied cases is of 8073.51s.

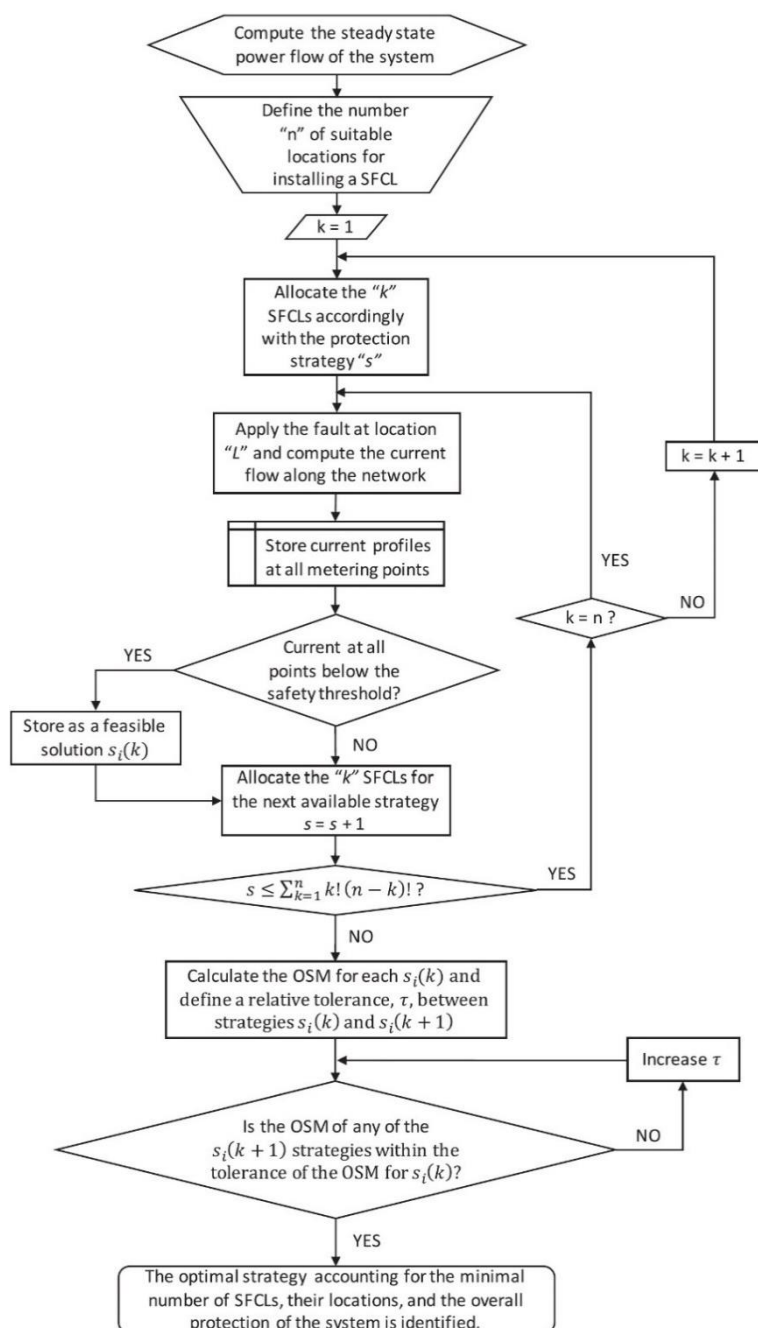


Figure 4.14: Flowchart of the algorithm for the identification of the optimal SFCL strategy.

We have therefore determined that in order to protect the overall grid from any of the fault events hereby considered, the installation of three SFCLs is enough within the established safety thresholds (see Figure 4.13). In particular, only two different arrangements made of up to three SFCLs have accomplished the desired conditions (see Table 4.6), i.e., the strategies $s = 18$ and $s = 19$, with the SFCLs installed at locations 1,2,5, and 1,3,4, respectively. It is to be noted that although strategy 19, which involves installing the SFCLs at the outgoing feeder of the power plant and the feeding ports of the domestic and industrial networks, offers a significant improvement when the fault occurs at the domestic branches, it is necessary to consider the needs of expansion of the power grid when making decisions. Thus, we conclude that strategy 18 which refers to installing SFCLs at locations 1,2,5 is the optimal scheme for the deployment of the SFCLs. The SFCL at location 2 protects the wind power plant directly and therefore preventing potential islanding problems [161]. Moreover, introducing a SFCL at the bus-tie (SFCL 5) would enable the transformers TR3 and TR4 to work in parallel, leading to a doubled short circuit capacity and lower transformer losses [81], which in turn results in lower voltage drops, improved stability, and savings in load connection expenses [34].

Table 4.6: Operational safety margin (OSM) for the s protection strategies, which consider the installation of up to 3 RSFCLs.

s	IP-Fault 1	IP-Fault 3	IBC-Fault 1	DBC-Fault 2
16	16%	10%	9%	-1%
17	8%	10%	-15%	24%
18	18%	10%	4%	3%
19	16%	10%	9%	24%
20	18%	10%	13%	-41%
21	18%	10%	-2%	24%
22	3%	-233%	-4%	24%
23	5%	-233%	2%	5%
24	-53%	-233%	-48%	24%
25	5%	-233%	-2%	24%

4.6 Conclusions

This chapter presents a comprehensive study on the performance and the optimal allocation analysis of RSFCLs inside two power system models built based on the UK network standard. In order to assess the impact of incorporating SC material properties on the performance of SFCLs, three different models were used throughout the study. First, the active operation of an SFCL was modelled using a Heaviside function. Second, the rise of SFCL resistance was described using an exponential descriptive equation. Third, a more realistic model was used to simulate the operation of an SFCL, taking into consideration the proper $E - J$ characteristics of the superconducting material and dynamic temperature evolution. Independently of the model used, we have proven that SFCLs can effectively improve the damping characteristics of the generation system, and can mitigate voltage dips at the grid. However, we have shown that although computing time can be reduced when step-resistance and exponential equation models are used, such simplifications lead to strong overestimations of the actual prospective performance of the SFCL, in terms of the maximum reduction on the fault current, its

correlated normal resistance, and also may result in wrong conclusion of optimal locations for SFCLs. Thus, this comparison led us to the conclusion that adequate physical properties for the electro-thermal dynamics of the SC materials has to be considered in order to accurately predict behavior of SFCLs inside a power system.

Systematic studies were then performed using the prospective strategies for the installation of one or more SFCLs. We have proven that installing more SFCLs does not necessarily mean better overall performance. For both power system models, the simultaneous use of three SFCLs is the best protection strategy in terms of the performance, economic efficiency and the reliability of the overall grid. In order to draw this conclusion, all the potential combinations of two, three, four, and five SFCLs were studied under a wide number of fault scenarios and measuring strategies.

Chapter 5

General Approach for Determining the Magnetic Field-Angular Dependence of Critical Current of YBCO Tapes for RSFCLs

In previous chapters, the current limiting behaviours of RSFCLs were simulated by considering the E-J power law and the temperature characteristics of HTS materials. Through performance comparison among the E-J power law, exponential and step-resistance RSFCL models, it was proved that the latter two methods were inaccurate due to over-simplification of the physical properties of superconductors. The E-J power law model can provide relatively precise results because the critical current dependence on the electrical field and temperature is taken into consideration, however, it should be noticed that the influence of magnetic field is still neglected. Studying the magnetic field-angular dependence of critical current is of great importance, especially for simulations of RSFCLs, since the magnetic field generated by fault current with high magnitude can be considerable. More importantly, in this chapter, a general approach for determining a unified function $I_c(B, \theta)$ which capable of describing the magneto-angular dependence of the critical current of 2G HTS tapes is presented.

5.1 Introduction

It is expected that the steady progress in the deposition techniques and fabrication of YBCO coated conductors or 2G-HTS tapes will lead to more competitive prices and improved efficiencies in comparison to resistive conductors such as copper, and the progressive development of superconductors can boost the application of resistive superconducting fault current limiters. However, in order to design and optimize the

structure of RSFCLs, ideally it is necessary to know in advance what is the value of the critical current density of the used tape when it is affected by internal and external magnetic fields, also called the in-field critical current density $J_c(B, \theta)$ [162].

The critical current density of YBCO coated conductors displays a complex anisotropic behaviour for in-plane and out-of-plane applied magnetic fields, even when the field is only applied in perpendicular direction with the flow of the electric current, and the complex interaction between shielding and transport currents is confined to two dimensions. The essential physics behind the collected vast phenomenology has been well known for decades [163, 164] and it may be analysed in terms of interactions between the flux lines themselves (lattice elasticity and line cutting) and interactions with the underlying crystal structure (flux pinning). However, if J is locally perpendicular to B , it is easy to demonstrate that the flux lines are always parallel to each other [165] and therefore, the anisotropy of the in-field critical current density $J_c(B, \theta)$ may have its main origin in the crystal structure and fabrication of the YBCO layer. It is this dependence on the fabrication process what hinders the assertion of the existence of a general function that might describe the in-field dependence of the critical current density of commercial 2G-HTS tapes, regardless of their manufacturer.

We have experimentally measured the $J_c(B, \theta)$ function of different batches of superconducting tapes fabricated by four different companies, namely SuperPower Inc. (SP), American Superconductor (AMSC), Shanghai Superconductor Technology Co., Ltd. (SHSC), and SuperOx (SO). The experiments were conducted under the same experimental conditions, in order to explore the possibility of unifying their physical behaviour in a general $J_c(B, \theta)$ function. The critical current density profiles of the tested tapes are measured under the action of a homogeneous external magnetic field of intensities ranging from 50 to 400 mT, in all cases. The experiment has been performed such that the angular dependence on the magnetic field can be studied in increments of 2° from the in-plane field approach, i.e., with the field parallel to the

wider surface of the SC tape and with $J \perp B$. It covers the peak width of the critical current density which spans towards the out-of-plane field directions ($\theta = \pm 90^\circ$), with the maximum centred when the magnetic field is applied parallel to the wider surface of the SC tape. Thus, later it is shown that regardless of the manufacturer and width of superconducting tape, a simplified function of the infield critical current density $J_c(B, \theta)$ can be constructed, by extending the scope of the Kim's model $J_c(B)$ for the out-of-plane approach, and assessing the magneto-angular dependence of the fitting parameters therein assumed [21].

5.2 Experimental Setup

A 600 mT electromagnet of $\sim 204 \text{ mm}$ pole face diameter was employed for the angle-resolved critical current density measurements. The magnetic field was measured with a HZ-11C hall-probe aligned with the pole face centre of the electromagnet. The longitudinal axis of the YBCO coated conductor, which was mounted over a tufnol support board, is coaxially aligned with the rotation axis of a high precision rotation stage as shown in Figure 5.1 and Figure 5.2. The two main parts were coaxially connected by a stainless-steel rod. The shape of the tufnol board was carefully calculated and designed with a neck offset to ensure a coaxial relationship between the test sample and the rotation stage in all field orientations (see Figure 5.1). This configuration enabled rotation of the sample holder, to obtain certain external magnetic field orientations. Two small copper plates for clamping was also annexed to the main part.

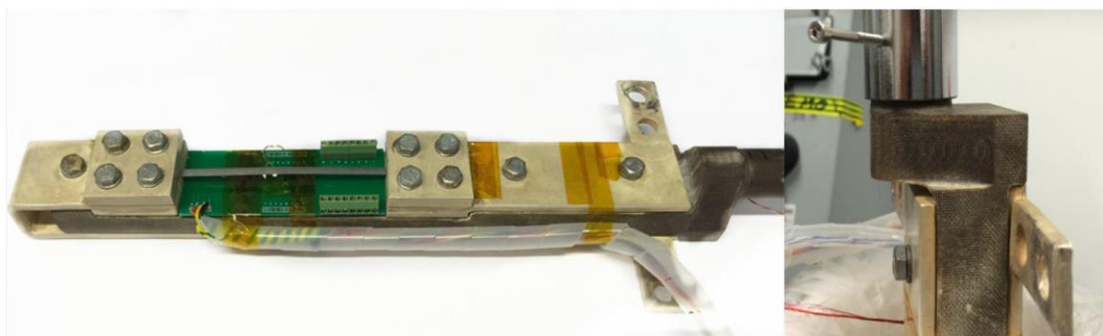


Figure 5.1: Picture of the sample holder and the neck offset for coaxial configuration.

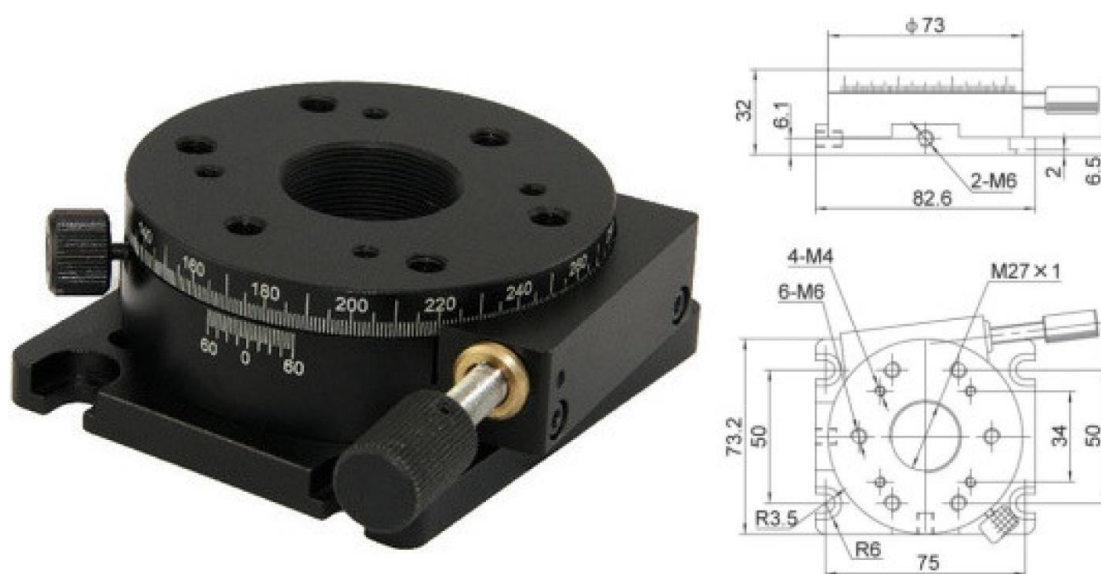


Figure 5.2: Picture and dimensional drawing of the rotation stage. The high precision manual rotation stage had a graduation of 1° and vernier of 5.

The current return path has been aligned parallel with the length of the sample at a distance of 10 cm, such that the maximum magnetic field produced by the current return path over the surface of the sample (~ 1 mT at 533 A), and its influence on the measurement of the critical current for applied magnetic fields ranging from 50 to 400 mT can be neglected. The transport current for the superconductor was provided by an Agilent 6680A Series Single-Output, 5000 W DC Power Supply (see Figure 4.8). The maximum available output voltage and current were 5 V and 875 A, respectively. During the quench experiments, the power supply was operated in the constant current mode and was controlled by the standard commands for programmable

instruments (SCPI) over an IEEE 488 bus. The programming resolution for controlling the current was 0.1%.



Figure 5.3: Picture of the Agilent 6680A 5000-Watt system power supply, 5V, 875A.

Low temperature solder (melting point 470 K) was used to attach the voltage taps on the nameplate side of the YBCO coated conductor. However, depending on the characteristics of the stabilizer layer. The solder-flux used for adequate soldering of each of the voltage taps corresponded to the manufacturers' suggestions. For example, for copper or brass laminated tapes, zinc chloride flux (Baker's Soldering Fluid No.3) was applied to the sample surface where solder dots were to be made. For stainless steel laminated tapes, highly corrosive solder flux (Superflux, Castonlin Eutectic) was used to provide a better electrical connection.

The critical current of studied HTS tapes was measured while the samples were immersed in liquid nitrogen bath, with voltage criterion $E_0 = 1 \times 10^{-4} V \cdot m^{-1}$ applied. All measured samples are 160 mm length, and the end terminals were clamped by copper plates and copper bases with four M5 cap head screws. The contact length was 15 mm for HTS tapes 4–6 mm width, and 25 mm for HTS tapes 10–12 mm width, respectively. High purity indium was also applied to the interlayer of coppers for cold welding, and the contact resistance at room temperature was determined to be $0.8 m\Omega$ for 4–6 mm width tapes, and $0.2 m\Omega$ for 10–12 mm width tapes, respectively. Finally,

the differential of voltage between the taps was measured with a Keithley 2182A nano-voltmeter. All the instruments were connected via an IEEE-488 GPIB bus with in-house built LabVIEW controllers.

The mounted sample was placed in a non-magnetic thermal ask in the presence of external electromagnetic fields, in which the gap between the adjustable magnetic poles was minimized. Thereby, a more homogeneous field could be established in the central area where the test sample was located (see Figure 5.4).

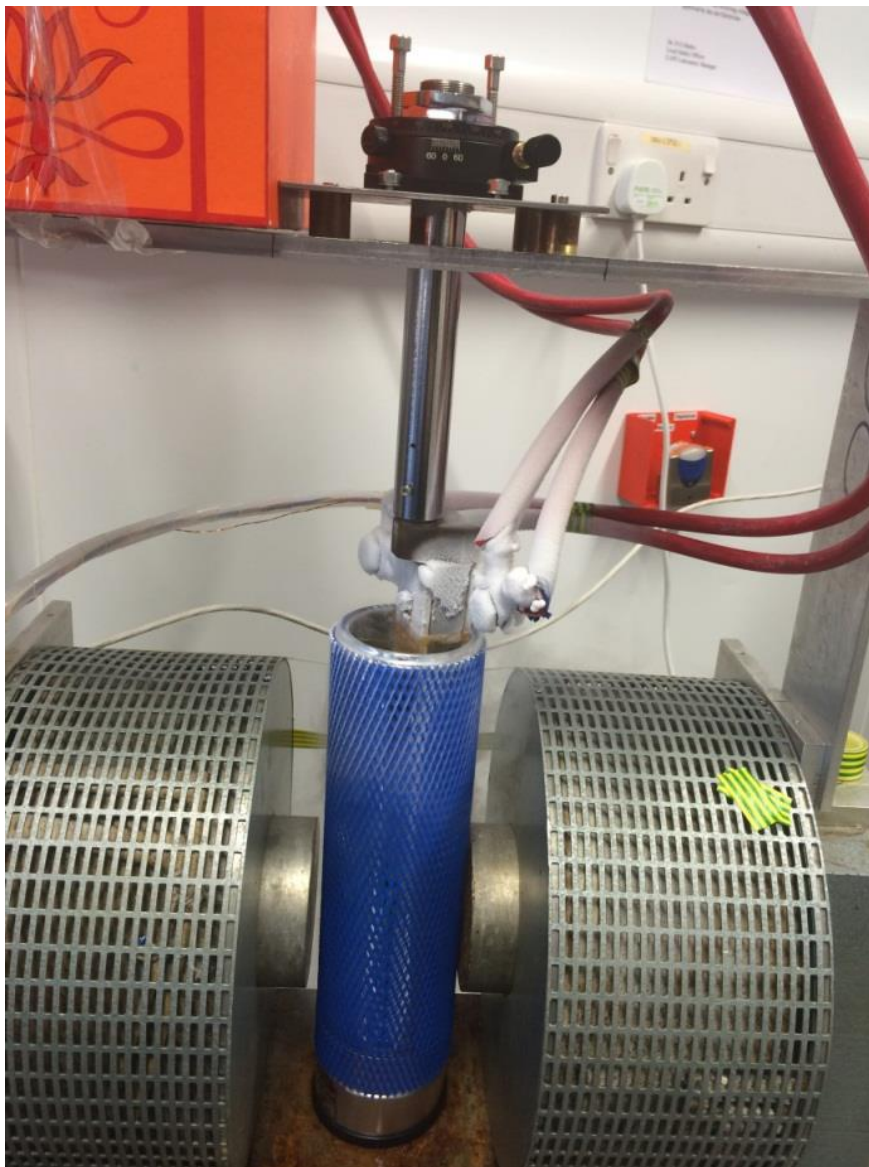


Figure 5.4: Picture of the experimental apparatus.

5.3 Measured YBCO Coated Conductors

Ten different YBCO coated conductors from three different manufacturers have been considered. For the sake of clarity, the ten samples were divided into two groups, each group containing five 2G HTS tapes.

For the first group, two different types of SP tapes have been tested, namely, 4 mm width SCS4050 tapes with top and bottom Cu stabilizer layers of ~ 0.02 mm thickness, and the 12 mm width stabilizer free SF12100 tapes [101]. In both cases, the YBCO layers are fabricated by metal organic chemical vapor deposition (MOCVD) over a buffer of heteroepitaxial layers deposited by sputtering, on a Hastelloy C-276 substrate of 0.1 mm thickness for the SF12100 tape, and 0.05 mm thickness for the SCS4050 tape, respectively. The YBCO layers (~ 1 mm thick) are then coated by a thin Ag layer of about ~ 2 mm thick to provide electrical contact. For the AMSC samples [166], we have chosen the 4.4 mm width single YBCO layer tape or AMSC8700 tape with brass stabilizing layers of 0.15 mm thickness and also, the 12 mm width double layer YBCO tape or AMSC8612 tape with stainless-steel stabilizing layers of 0.07 mm thickness. In both AMSC tapes, the YBCO layers are deposited by MOCVD over a similar stack of heteroepitaxial layers (buffer) grown on a 0.075 mm thickness NiW alloy substrate. However, it is worth emphasizing that the AMSC8612 is a double layered HTS tape, i.e., the tape is composed by two stacks of YBCO/Buffer/NiW layers placed back-to-back in a single laminated package with the YBCO films coated by a ~ 3 mm thick layer of Ag. Finally, the last of our five samples corresponds to the 5.8 mm width, 0.220 mm thickness, 2G-HTS tape provided by Shanghai Superconductor (SHSC), also called ST-06-L tape [93], with similar substrate and buffer layer characteristics to the SP tapes, although with the YBCO layer deposited over a MgO template (buffer) by pulsed laser deposition (PVD) rather than MOCVD. A brief comparison of the technical features of the five 2G-HTS tapes aforementioned, is presented in table for the ease of the reader.

Table 5.1: Technical parameters of the first group of 2G-HTS tapes.

2G-HTS tape	No. YBCO layers	Total thickness (mm)	Width (mm)	Ic Max. (A)	n value
SCS4050	1	0.055	4	114	30.5
SF12100	1	0.105	12	388	30.1
AMSC8700	1	0.150	4.4	98.2	36
AMSC8612	2	0.330	12.2 ^(a)	533	52.2
ST-06-L	1	0.220	5.8	167	42.14

^(a) The 12.2 mm width of the AMSC8612 sample includes the solder fillet layers at each side of the tape (1.1 mm), i.e. with an effective YBCO layer of 10 mm width.

The five YBCO samples of the second group were also produced by three different manufacturers: SuperPower Inc. (SP), Shanghai Superconductor Technology Co. Ltd. (SHSC) and SuperOx (SO). To be more specific, two types of 2G-HTS tapes from SP were tested: surround copper stabilizer tapes of 2 mm width (SCS2050) and 6 mm (SCS6050), respectively. The tapes are made by Metal Organic Chemical Vapour Deposition (MOCVD) on an ion beam assisted deposition made MgO template. The YBCO layer of the two tapes is 1 μm thick, and the substrate of both samples is non-magnetic commercial compound Hastelloy C-276, with thickness of 50 μm . Two 2 μm silver layers made by the sputtering technique are coated outside the YBCO layer and the substrate, providing outstanding electrical contacts [167]. The third and fourth samples come from SHSC, with widths of 4 mm (ST-04-E) and 4.8 mm (ST-05-L), respectively. Both tapes have non-magnetic commercial compound Hastelloy substrate and metal organic deposited YBCO layer. However, it is worth mentioning that ST-04-E is electroplated with brass, while ST-05-L has a stainless steel lamination [168]. The last sample refers to the 12 mm wide, 0.12 mm thick YBCO tape that manufactured by SuperOx, also called SO-12. This tape has a cold-rolled and electro-polished Hastelloy C-276 substrate with width of 60 μm . The YBCO layer is fabricated by pulsed laser deposition (PLD) over a buffer of heteroepitaxial layers deposited by sputtering on the substrate. Moreover, outside the silver and copper electroplating, the tape is covered by

5 μm thick surround polyimide coating [169]. Further information about the technical specifications of the five tested tapes is gathered in Table 5.2.

Table 5.2: Technical parameters of the second group of 2G-HTS tapes.

2G-HTS tape	Total thickness (mm)	width (mm)	Ic Max. (A)	n value
SCS2050	0.095	2	58.8	32.5
SCS6050	0.095	6	166.6	31.9
ST-04-E	0.130	4	112	38.2
ST-05-L	0.350	4.8	175.3	45.1
SO-12	0.120	12	301.4	34.4

5.4 Generalizing the magnetic field-angular function

$$I_c(B, \theta)$$

For the selection of different 2G-HTS tapes shown in Table 5.1, we have measured the profile of critical current I_c as a function of the applied magnetic field, B , and its orientation, θ , in the maximum Lorentz force configuration, i.e., with the magnetic field applied perpendicular to the direction of the transport current. Therefore, the field angle θ is defined as 0° when the external magnetic field is parallel to the ab -plane of the YBCO tapes, as illustrated in figure 2. Therein, similar qualitative features of the in-field $I_c(B, \theta)$ function can be observed for the different 2G-HTS tapes that have been studied. In more detail, the maximum critical current at self-field, $I_c(0, \theta)$, i.e., without the influence of an external magnetic field has been measured for all samples and then, the magneto-angular study has been conducted for external magnetic fields of intensities $B = 50 \text{ mT}, 100 \text{ mT}, 200 \text{ mT}, 300 \text{ mT}$ and 400 mT , respectively. For the sake of comparison the results obtained at $\theta = 0^\circ$ ($B // ab - \text{plane}, B \perp I$) and $\theta = \pm 90^\circ$ ($B // c - \text{axis}, B \perp I$) are shown in Table 5.3.

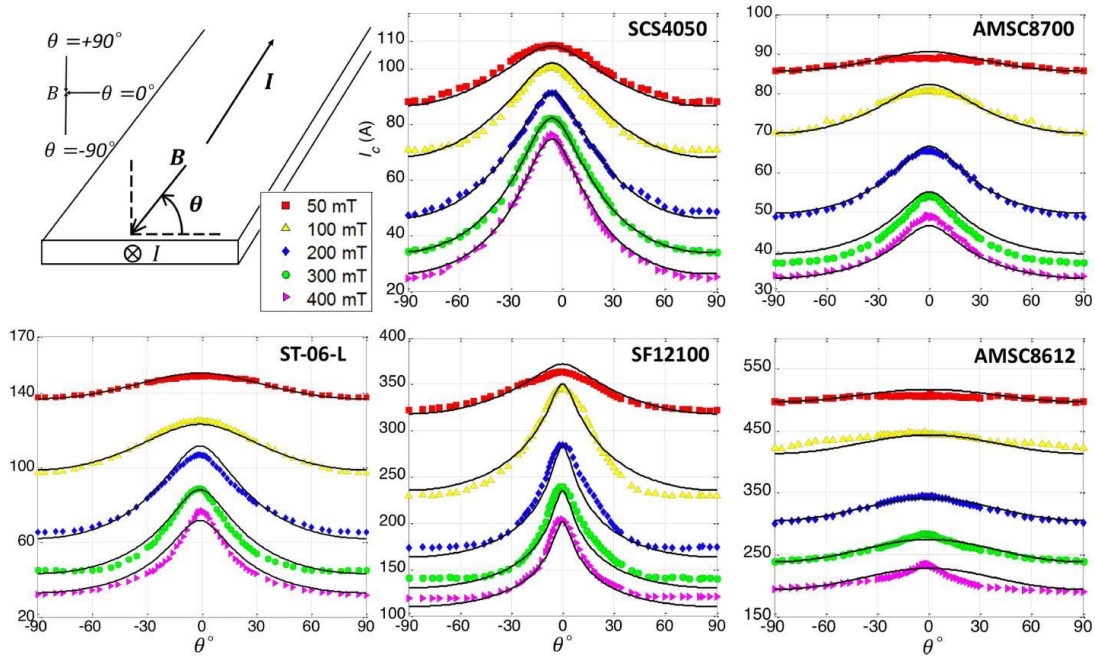


Figure 5.5: In-field magneto-angular dependence of the critical current I_c for the 2G-HTS tapes summarized in Table 5.1. Solid symbols correspond to the experimental data acquired for an external magnetic field of 50 mT (red-squares), 100 mT (yellow-triangles), 200 mT (blue-diamonds), 300 mT (green-circles), and 400 mT (purple-triangles), respectively. Solid lines, correspond to the results obtained from our extended version of the Kim's model. As greater the applied magnetic field is, the lower the critical current. The orientation of the field angle and the direction of the transport current for all cases is illustrated in the top-left pane of the figure.

In the case of the SP samples, SCS4050 and SF12100, a more acute drop of the critical current is observed when the applied magnetic field is tilted towards 90 from the ab-plane orientation of the HTS tape ($\theta = 0^\circ$), with a reduction of I_c of up to 67% at 400 mT for SCS4050, and 41% for SF12100, respectively. A similar drop pattern on the I_c is observed for the SHSC sample, ST-06-L, with a maximum reduction of the critical current of about 58% at 400 mT, and nearly the same percentage standard deviation when it is compared with the SCS4050 sample ($\Delta\sigma_{st} = 18.36(ST - 06 - L) - 18.04(SCS4050) = 0.32$). On the other hand, the AMSC samples show a more isotropic behavior on the angular dependence of the I_c , with a maximum drop of 31% at 400 mT for AMSC8700 ($\sigma_{st} = 10.88$), and only a 19% for the double layered HTS tape or AMSC8612 ($\sigma_{st} = 6.16$) sample. Nevertheless, although the magneto-angular

dependence of I_c on the AMSC samples is smaller than the observed one for the SP and SHSC samples, for comparable widths and structure, i.e., for the SCS4050 versus AMSC8700, a significant improvement of about 53% on the relative reduction of the I_c drop at moderately high fields (400 mT) is achieved. The SP samples at self-field conditions and for in-plane field ($\theta = 0^\circ$) attain greater critical current values. This is contrary to what happens when the external magnetic field is applied at $\theta = \pm 90^\circ$ and for intensities greater than 200 mT (see Table 5.3). It is worth mentioning that for the 12 mm double layered YBCO tape (AMSC8612) a straightforward comparison with the SF12100 sample cannot be achieved. This is because each one of the two layers of YBCO that compose the AMSC8012 tape is inherently affected by the magnetic field created by its reciprocal layer. Thus, although the total I_c measured for this tape is the greatest, it is expected that assuming equal sharing of current, the I_c per layer has to be smaller than the one observed for the SF12100.

Table 5.3: In-field magneto-angular dependence of the critical current I_c for the 2G-HTS tapes summarized in Table 5.1 for the external magnetic field intensities displayed in Figure 5.5, and for the angles $\theta = 0^\circ$ ($B//ab - plane, B \perp I$) and $\theta = \pm 90^\circ$ ($B//c - axis, B \perp I$)

2G-HTS tape	YBCO w (mm)	I_c ($0,0^\circ$)	I_c (50mT, 0°)	I_c (100mT, 0°)	I_c (200mT, 0°)	I_c (300mT, 0°)	I_c (400mT, 0°)
SCS4050	4	114	108.2	100	91.26	82.12	76.2
AMSC8700	4.4	98.2	89.04	80.58	65.39	54.11	49.12
ST-06-L	5.8	167	149.2	125.3	106.9	88.95	77
SF12100	12	388	363.2	345.8	284.6	239.6	204.77
AMSC8612	12	533	509.5	448.2	344	283	235
2G-HTS tape	YBCO w (mm)	I_c ($0,\pm 90^\circ$)	I_c (50mT, \pm 90°)	I_c (100mT, \pm 90°)	I_c (200mT, $\pm 90^\circ$)	I_c (300mT, \pm 90°)	I_c (400mT, $\pm 90^\circ$)
SCS4050	4	114	88.19	71.04	48.66	33.91	25.17
AMSC8700	4.4	98.2	85.59	70.17	48.33	37.25	33.78
ST-06-L	5.8	167	137.7	97.33	65.34	44.99	31.86
SF12100	12	388	322	229.8	147.7	140.1	120.9
AMSC8612	12	533	496.7	422.3	301.2	238.6	190

In order to generalize the previous results and allow an accurate prediction of the critical current in the maximum Lorentz force configuration, I_c , independently of the intensity of the applied magnetic flux density, and the angle θ , we have assumed that the critical current has to be moderated by the ratio between the effective mass of the charge carriers along the c-axis and the ab-plane of the YBCO layer, i.e., the electron mass anisotropy ratio $\gamma = m_c^*/m_{ab}^*$, as it was suggested by Blatter et al, in [170]. This anisotropy is caused by imperfect alignment of the ab-plane of each YBCO grain and the small fraction of grains with their ab-planes exactly parallel to the tape surface, which contributes to a large inter-grain critical current in a magnetic field parallel to the tape, as it has been experimentally observed (see Figure 5.5, $\theta = 0^\circ$). Thereby, we have extended the conventional Kim's model [21] taking into account Blatter's angular anisotropy factor, ε_θ , as follows:

$$I_c(B, \theta) = I_{c0} \left(1 + \frac{\varepsilon_\theta B}{B_0(B)}\right)^{-\beta} \quad (5.1)$$

with

$$\varepsilon_\theta = \sqrt{\gamma^{-1} \sin^2(\theta) + \cos^2(\theta)} \quad (5.2)$$

In Equation 5.1, $I_{c0} = I_c(0, \theta)$, i.e., the self-field critical current, and the empirical parameters introduced by Kim, B_0 and β , take into account the thermally activated flux-creep processes into specific samples. In fact, as the mechanism of flux creep is a thermally activated motion of bundles of flux lines, aided by the Lorentz force $\mathbf{J} \times \mathbf{B}$, over free energy barriers coming from the pinning effect of inhomogeneities, dislocations, strains, or other physical defects [23], in a first instance we have assumed that the parameter B_0 can be a function of B for the different samples considered in this study. Thus, by assuming the minimum number of empirical parameters that have been formulated within the Kim [21] and Anderson [23] flux creep theory, we have

fixed the value of I_{c0} in Equation 5.1 accordingly with our experimental observations (see Table 5.1 or Table 5.3), and the parameters γ , $B_0(B)$, and β have been determined for the lowest mean absolute percentage deviation (MAPD) and analogously, for the lowest root-mean-square deviation (RMSD) of the experimental data, with the minimum order function for $B_0(B)$. The latter fact is important because multiple guesses of the parameters γ and $B_0(B)$ could lead to similar MAPD and RMSD outcomes on specific tapes. Nevertheless, what is possible is to find a suitable expression for the different SC tapes along the minimization of the MAPD and RMSD values, by introducing the smaller possible number of unknown variables.

Thus, initial estimates for each one of the three free parameters in Equation 5.1 have been assumed, and a similar iterative procedure to the one introduced in [171] has been used. We have reduced the ambiguity on the initial guesses by taking into consideration that the electron mass anisotropy ratio, γ , ranges between 1 for fully isotropic samples to about 25 for $YBa_2Cu_3O_{7-\delta}$ grains with highly anisotropic conductivity [172]. Also, it has been already reported that the flux creep exponent β for YBCO samples is commonly less than 2 [171, 173]. Then, for a determined number of estimates, (γ, B_0, β) , the MAPD and RMSD of Equation 5.1 with respect to the experimental measurements have been calculated for each one of these sets, and the overall number of resulting expressions minimized according to the following expressions:

$$\text{Min}[\xi_{MAPD}] = \text{Min} \left[\sum_{k=1}^{N_B \cdot N_\theta} \frac{1}{N_B \cdot N_\theta} \left(\frac{|I_c^{(\gamma, B_0, \beta)} - I_c^{(exp.)}|}{I_c^{(exp.)}} \right)_{(k)} \right] \quad (5.3)$$

and

$$\text{Min}[\xi_{RMSD}] = \text{Min} \left[\sqrt{\frac{\sum_{k=1}^{N_B \cdot N_\theta} (|I_c^{(\gamma, B_0, \beta)} - I_c^{(exp.)}|)_{(k)}^2}{N_B \cdot N_\theta}} \right] \quad (5.4)$$

where the sub-index (k) indicates the subset of data taken from the N_θ angular measurements at the N_B different values of applied magnetic field, and $I_c^{(\gamma, B_0, \beta)}$ is the numerical value obtained during the minimization for the best fitting to the experimental results $I_c^{(exp.)}$ by means of Equations 5.1 and 5.2.

The optimal minimization process for the fitting of the (γ, B_0, β) parameters depends therefore on the number of estimates allocated to each one of these parameters, separately. For instance, if 20 different values are considered for each one of the parameters, γ , B_0 , and β , respectively, the minimization runs over a total of 8000 possible combinations for each N_B curve, and the percent deviations of the MAPD (ξ_{MAPD}) and RMSD (ξ_{RMSD}) have to be constrained to a maximum threshold in order to accept the solution. Thus, we have constrained the solution of Equation 5.3 to satisfy the conditions $\xi_{MAPD} \leq \epsilon$ and $\xi_{RMSD} \leq \epsilon^2$ with $\epsilon = 3\%$ for all the N_B curves, simultaneously. As a result, less than 1% of the $8000 \times N_B$ suitable combinations for $I_c^{(\gamma, B_0, \beta)}$ survive for all N_θ measurements, and the results obtained for the minimum relative average between ξ_{MAPD} and ξ_{RMSD} are shown in Table 5.4. Nevertheless, a univocal value for the parameter B_0 was only obtained for the SCS4050 and AMSC8612 samples, this imposes an additional challenge for the determination of a singular $I_c(B, \theta)$ function for the 2G-HTS tapes: AMSC8700, SF12100, and ST-06-L. For instance, for the AMSC8700 sample, the lowest ξ_{MAPD} and ξ_{RMSD} values that have been obtained for a single definition of B_0 were 6.75 and 7.24, respectively, what does not satisfy the threshold condition for ξ_{MAPD} resulting in a deviation of more than 15% in the peak of current $I_c(B, 0^\circ)$.

Thus, in order to satisfy the tolerance conditions and reduce the deviation between the numerical results and the experimental observations, it is at this point that it is necessary to consider that the parameter B_0 depends on the magnitude of the applied magnetic field. Two essential conditions need to be satisfied during the derivation of

this equation: First, the resulting expression has to be as simple as possible, i.e., by introducing the minimum number of free parameters that may allow the reproduction of the experimental results in even different coated conductors. Secondly, the resulting equation has to be physically consistent with the units in Equation 5.1. The latter is important because the uncertainty on the physical nature of B_0 has led in the past to the formulation of cumbersome but yet accurate fitting expressions on specific batches of commercial tapes [173] that in some cases allows the adding of a significantly large number of physically unknown parameters with severe inconsistencies on the physical units [174]. However, we recognize that there is not a single way for finding this kind of expression, and different fitting equations can be obtained depending on the initial ansatz for the mathematical structure of $I_c(B, \theta)$. Therefore, finding a univocal solution for the function $I_c(B, \theta)$ is indeed cumbersome, and in general requires of the initial consideration of a larger number of variables during the minimization procedure.

However, returning to the root of the problem, Equation 5.1 can be rewritten in a more general way as:

$$I_c(f(B), \theta) = I_c(1 + \varepsilon_\theta f(B))^{-\beta} \quad (5.5)$$

with $f(B) = [(\zeta B + \delta)/B_0]^\alpha$, being the parameters ζ , δ , and α , new variables into the minimization procedure, such that in Equation 5.3 and Equation 5.4 the function of three variables $I_c^{(Y, B_0, \beta)} = I_c(B, \theta)$ in Equation 5.1 is replaced by $I_c(f(B), \theta)$, in a first approach. The parameter δ , which is the only one with physical units, has been introduced for mathematical convenience as it allows a faster minimization of the powers α and β by compensating the impact of the highly nonlinear terms. Moreover, the minimization of the objective functions is conditioned to progressively achieve a reduction of δ , i.e., to $\delta_{t+1} < \delta < d$, for $\delta_{t+1} > 0$ in order to avoid the occurrence of complex singularities in I_c . Also, it is possible to help further the minimization by imposing the conditions $\zeta \geq 1$, and $\alpha \geq 0$. Thereby, we have

found that the function $f(B)$ is strikingly reduced to a very simple and elegant expression:

$$f(B) = \left(\frac{B}{B_0}\right)^\alpha \quad (5.6)$$

with our final results presented in Table 5.4, and showing an excellent agreement with the experimental results displayed in Figure 5.5

Table 5.4: Fitting parameters found after the minimization procedure of Equation 5.5 is performed, it leading to Equation 5.6 and the matching of the experimental results displayed in Figure 5.5.

2G-HTS tape	B_0 (mT)	α	β	γ	ξ_{MAPD}	ξ_{RMSD}
SCS4050	240	1	1.5	5.02	1.57	1.21
SF12100	44.83	2.4	0.24	13.32	2.93	8.25
AMSC8700	72.75	2.4	0.25	4	1.89	1.64
AMSC8612	280	1	1.3	1.25	1.27	5.91
ST-06-L	91.03	1.7	0.58	4.17 ^b	2.91	2.51

Despite SCS4050 and AMSC8612 samples having different widths and consequently different self-field critical current densities [$I_c(0,0^\circ)$ in Table 5.3], they possess very close fitting parameters: B_0 , α and β . Therefore, the magneto-angular dependence of the SCS4050 and AMSC8612 samples are rather similar, although the electron mass anisotropy ratio of SCS4050 is about 4 times greater than in the AMSC8612 sample ($\gamma_{SCS4050}/\gamma_{AMSC8612} = 4.016$). This fact explains the high increase on the critical current density when the magnetic field in the Lorentz-force configuration is applied parallel to the surface of the ab-planes of the SCS4050 tape, i.e., $\theta = 0^\circ$ at figure 2, a

^b For applied magnetic fields lower than 200 mT, the obtained electron mass anisotropy ratio for the ST-06-L sample and under the same conditions displayed in this table corresponds to $\gamma = 2.08$. Thus, the theoretical curves shown in the ST-06-L pane of Figure 5.5 for $B_{ext} = 50$ and 100 mT are obtained with $\gamma = 2.08$, otherwise the results therein are for $\gamma = 4.17$.

phenomenon which is nearly unseen at 50 mT with the AMSC samples. A similar comparison can be made between the SF12100 and the AMSC8700 samples ($\gamma_{SF12100}/\gamma_{AMSC8700} = 3.33$). Thus, further to the general expression that we have found for the magneto-angular in-field function $I_c(B, \theta)$, from our previous analysis it is possible to conclude that the contribution due to the charge carriers along the c-axis of the YBCO tapes manufactured by SP is greater than in those manufactured by AMSC or SHSC, a phenomenon that is increased when the YBCO tape is not coated by Cu stabilizer layers. Nevertheless, the sample manufactured by SHSC (ST-06-L) has shown a stronger dependence of the mass anisotropy factor γ on the intensity of the applied magnetic field. In this case it was not possible to find a solution capable of satisfying the threshold values for ξ_{MAPD} and ξ_{RMSD} , simultaneously. Thus, although these threshold values can be adjusted, it is worth mentioning that for the best of the cases we have found that $\gamma \sim 4.35$ for $\xi_{MAPD} \sim 3.5\%$ and $\xi_{RMSD} \sim 4.2\%$. However, it produces an acute deviation of the peak values of the critical current density at $\theta = 0^\circ$, particularly noticeable at lower magnetic fields ($B \leq 100\text{mT}$), with the experimental results being overestimated by more than a 10% difference. It could be seen maybe as a small difference for the reader, but it has to be noticed from Table 5.3 that the percentage differences between the self-field critical current $I_c(0,0^\circ)$ and the peaks values of the critical current at 50 mT and 100 mT are of $\sim 10.7\%$ and $\sim 25\%$. Consequently, by accepting the aforementioned condition, the actual overestimation of the increase in the critical current density in the in-field configuration results in a deviation of more than 20% from the self-field critical current value. Thus, this simplified approach is not acceptable. Consequently, we conclude that there is a weaker influence of the charge carriers along the c-axis of the YBCO layer in the ST-06-L tape for magnetic fields lower than 200 mT, i.e., with $\gamma = 2.08$, than what is observed for greater magnetic fields where the minimum γ has been found to be double (see Table 5.4).

5.5 Validation of the Fitting Function $I_c(B, \theta)$ Using the second Group of YBCO Samples

Similarly, for the second group of 2G HTS tapes, the variation of critical current I_c with the applied magnetic field and its orientation are presented in Figure 5.6. The magnetic field was also applied in the direction perpendicular to the transport current, which is the maximum Lorentz force configuration. The field angle θ is defined as 0 degrees when the external magnetic field is parallel to the ab plane of HTS tapes, as illustrated in Figure 5.6 (a).

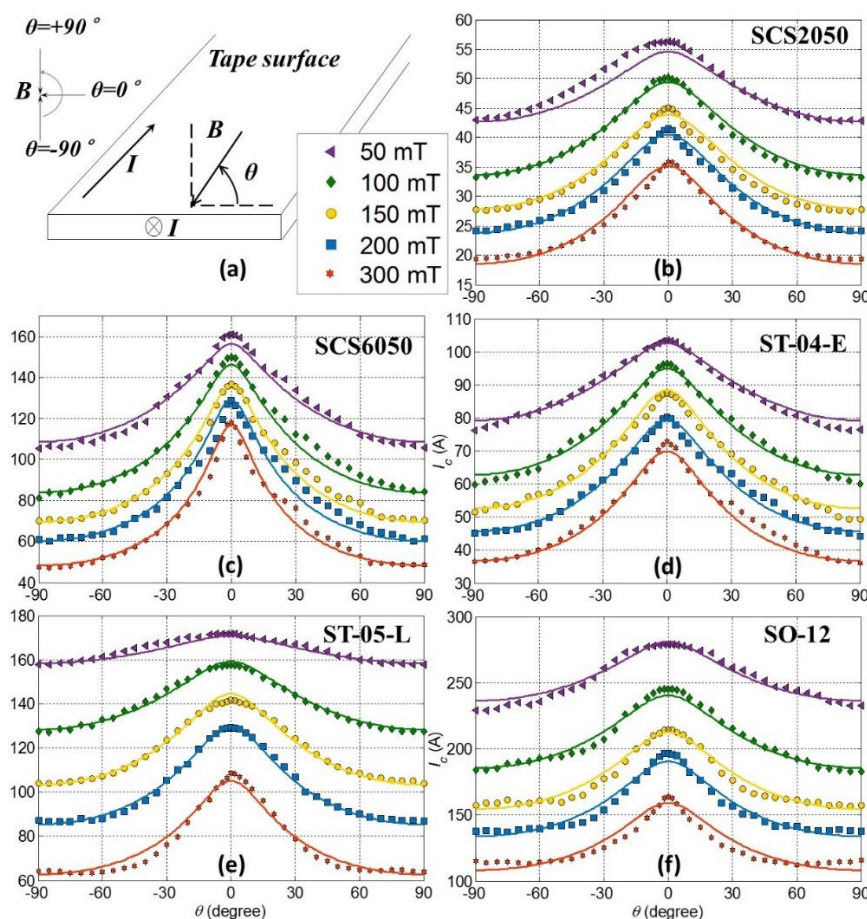


Figure 5.6: Magnetic field-angular dependence of measured commercial YBCO tapes: comparison between experimental data (symbols) and fitting curves (solid lines). Experimental measurement at less important angles was not plotted for clarity.

It can be seen from Figure 5.6 that the variation trends of critical current in samples from different commercial enterprises possess similar qualitative features, suggesting that the same pinning mechanisms might be at play. In general, all tapes exhibit noticeable peaks when the external magnetic field is parallel to the film surfaces ($B//ab$). However, it fails to show another peak centred at $B//c$, indicating that the effect of correlated pinning (or intrinsic pinning) is insignificant under moderate magnetic fields. Detailed information about percentage decline of magnetic field critical current ($B = 50 \text{ mT}$ or $B = 300 \text{ mT}$, $\theta = 0^\circ$ and $\theta = \pm 90^\circ$) relative to self-field critical current in measured YBCO commercial tapes has been calculated and gathered in Table 5.5.

Table 5.5: Percentage decline (P_d) of magnetic field-critical current (50 mT and 300 mT, 0° and $\pm 90^\circ$) with respect to self-field critical current for the studied 2G-HTS tapes

	Width (mm)	I_c (0 mT, 0°) (A)	P_d (50 mT, 0°) (%)	P_d (50 mT, $\pm 90^\circ$) (%)	P_d (300 mT, 0°) (%)	P_d (300 mT, $\pm 90^\circ$) (%)
SCS2050	2.0	58.8	5.1	27.1	31.7	67.8
SCS6050	6.0	166.6	4.2	37.1	28.7	70.1
ST-04-E	4.0	112.0	8.0	31.3	35.7	66.9
ST-05-L	4.8	175.3	3.9	9.2	38.8	64.0
SO-12	12.0	301.4	8.3	24.6	45.5	61.1

Specifically, the 6 mm SuperPower sample SCS6050 shows the most significant angular dependence among all measured tapes. Under 300 mT external magnetic field, it experiences the smallest percentage decline 28.7% at $\theta = 0^\circ$ ($B \parallel ab - \text{plane}, B \perp I$), while the biggest percentage decline 70.1% at $\theta = \pm 90^\circ$ ($B \parallel c - \text{axis}, B \perp I$). The strong anisotropic characteristic makes this YBCO sample suitable for applications in which external field is always parallel to the ab-plane of the tape, since relatively high critical current can still be preserved with increase of the field density.

Compared with SCS6050, the other SuperPower sample SCS2050 has a smoother descendance of I_c when external field increases: from the self-field critical current 58.8 A reduced by 31.7% at 300 mT/0° and 67.8% at 300 mT/90°, as shown in Figure 5.6(b). Then, further measurement reveals that, along with changes of angle and intensity of the external magnetic field, the variation trend of critical current profiles of ST-04-E from Shanghai Superconductor is very similar to SCS2050. The differences between average percentage decline of ST-04-E and SCS2050 are only 3.6% at 50 mT and 2.5% at 300 mT, respectively.

The remaining two YBCO samples, ST-05-L from Shanghai Superconductor and SO-12 from SuperOx, are less sensitive to the angle and density of external magnetic field, indicating that these two tapes have better in-field performance in moderate fields. Among all measured 2G-HTS wires, the one with the lowest magnetic-angular dependence is SO-12, which critical current curve is less steep compared with other samples, as can be seen from Figure 5.6(e). With this relatively isotropic property, SO-12 is capable to perform very well when assembled in rotating devices, e.g., superconducting motors, due to its high effective critical current in varying electromagnetic environment compared with other measured samples.

Using the fitting method derived in this chapter, it was found that the parameters $B_0 = 80.83$ mT, $\alpha = 1$, $\beta = 0.72$ and $\gamma^2 = 4.35$ can provide a desirable fitting result for the sample ST-04-E, as can be seen from Figure 5.6(d). Calculation gave that the corresponding MAPD and RMSD in this case were 1.75% and 1.48, respectively. Using the same method, for the tape SCS6050 (Figure 5.6(c)), it was found that 83 out of 8000 parameter combinations could lead to precise fitting curves (MAPD within 3%). The lowest MAPD and RMSD in this case were 2.30% and 3.06, which were generated by the following data set: $B_0 = 56.04$ mT, $\alpha = 1$, $\beta = 0.67$ and $\gamma^2 = 7.69$.

Setting $\alpha = 1$ prior to the optimization is suitable for ST-04-E and SCS6050. However, when the studied tapes express more complicated anisotropy of critical current properties, the tolerance requirement between the optimization results and experimental observations can no longer be accomplished: e.g. for the 2.0 mm tape SCS2050, the lowest MAPD and RMSD can be achieved with $\alpha = 1$ is 5.37% and 3.19, which means the peaks of current curves are distorted by more than ten percent.

In order to achieve desirable accuracy and maintain the least number of fitting parameters, the value of α will have to be varied to provide accurate estimations. With an alterable α in the optimizing procedure, the MAPD and RMSD of SCS2050 was substantially reduced to 1.21% and 0.77, respectively. The specific values of parameters to obtain fittings shown in Figure 5.6(b) are: $B_0 = 58.27$ mT, $\alpha = 1.29$, $\beta = 0.50$ and $\gamma^2 = 4.76$. In the same way, accurate expressions for the $J(B, \theta)$ dependence of the remaining two YBCO samples were achieved as well. For the stainless-steel laminated tape that manufactured by Shanghai Superconductor, ST-05-L, minimization showed that with $B_0 = 100.38$ mT, $\alpha = 1.98$, $\beta = 0.45$ and $\gamma^2 = 4.17$, the MAPD and RMSD can be as low as 1.06% and 1.47, respectively (Figure 5.6(e)). In addition, optimal fitting parameters of the 12mm wide sample SO-12 were proved to be: $B_0 = 53.26$ mT, $\alpha = 1.59$, $\beta = 0.36$ and $\gamma^2 = 3.34$. The corresponding MAPD and RMSD of this fitting are 1.88% and 4.01.

The explorations of $J(B, \theta)$ of all measured commercial tapes were successfully finished. The results above convincingly demonstrated the universality of our numerical approach, since in this paper the YBCO samples we studied were completely different from the samples we used in our previous research. The optimized fitting parameters and precision information of each 2G HTS tape are listed in Table 5.6.

Table 5.6: Optimal fitting parameters of the tapes and corresponding precision information

2G HTS tapes	I_{c0} (A)	B_0 (mT)	α	β	γ	MAPD	RMSD
SCS2050	58.81	58.27	1.29	0.5	4.76	1.21%	0.77
SCS6050	166.55	56.04	1	0.67	7.69	2.30%	3.06
ST-04-E	112.02	80.83	1	0.72	4.35	1.75%	1.48
ST-05-L	175.25	100.38	1.98	0.45	4.17	1.06%	1.47
SO-12	301.42	53.26	1.59	0.36	3.34	1.88%	4.01

5.6 Simulation of RSFCLs behaviours with consideration of the magnetic field-angular dependence of critical current $I_c(B, \theta)$

Figure 5.5 and Figure 5.6 show that the critical current of the 2G HTS conductor is significantly influenced by the external magnetic fields, especially when the external field is perpendicular to the surface of the conductor. Since the conductors of RSFCLs see huge current during system faults, the magnetic field they generate and its influence on nearby conductors in the RSFCL cannot be neglected. The magnetic field generated by the current flowing through the superconducting conductors can be approximately calculated based on the following equation:

$$B = \frac{\mu_0 I}{2\pi a} \quad (5.7)$$

In this section we study a RSFCL model which current limiting module is composed of two parallel placed long HTS cylinder conductors with diameter of 10 mm, which means the centre-to-centre distance equals 10 mm as well. Along with the expansion of

modern power grids, system faults with fault levels higher than 20 kA is very common. Hence, it is assumed that each conductor needs to limit 10 kA current during faults (20 kA in total).

According to Equation 5.7, the external magnetic field parallel to the surface of each conductor (generated by the other one) can be estimated as $B = \frac{4\pi \cdot 10^{-7} \cdot 10^4}{2\pi \cdot 10^{-2}} T = 200 \text{ mT}$. Figure 5.5 and Figure 5.6 shows when the commercial tapes were placed under 200 mT perpendicular magnetic field, their critical current properties are all reduced by more than 50%. For the SCS6050, the in-field critical current is only 36% of the self-field value. Based on these figures, it can be expected that the RSFCL would quench after this factor taken into consideration, and study of the change in current limiting behaviours is of great importance for RSFCL simulations.

Therefore, the E-J power law RSFCL model developed in Chapter 4 is further improved by integrating the $J_c(\theta, B)$ dependence derived for SCS6050 (see Table 5.6), and the structure of the current limiting module is set to be two parallel cylinder HTS conductor as discussed in this section. Then, under the condition of a 23 kA short circuit fault, the current limiting performance of the improved model and the original E-J RSFCL model is compared and plotted as follows.

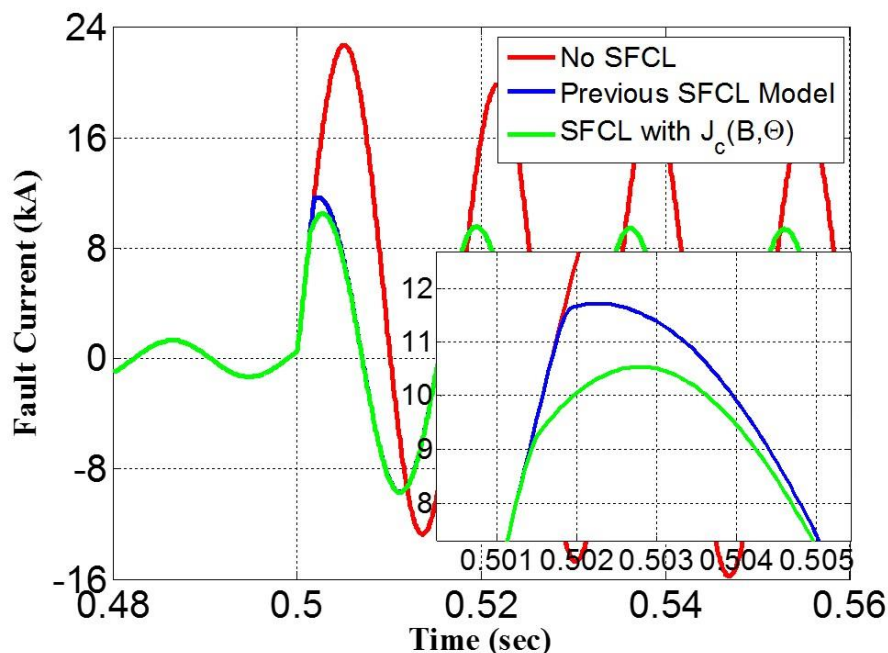


Figure 5.7: Comparison between current limiting performance of the original E-J power law RSFCL model and the E-J model with $J_c(\theta, B)$ dependence. The fault level without RSFCL is 23 kA. ($\theta = 90^\circ$, magnetic field perpendicular to the ab-plane)

Figure 5.7 shows that after considering the $J_c(\theta, B)$ dependence of the HTS conductor, the first peak limitation decreased by 10.2% from 11.7 kA to 10.5 kA. This observation is in accordance with our expectation. The current flowing through the RSFCL raised sharply after the fault, leading to significant decrease of critical current due to the external magnetic field. Hence, the quench processes of the two conductors accelerated accordingly. Moreover, it can be seen that the current limiting performances of the two models became the same after the first cycle. This phenomenon agrees well with the setting that the resistivity of the HTS conductor remained constant after the material entering normal state.

Then, the current limiting performance of the two models were compared again under a 9 kA fault. The simulation result was shown in Figure 5.8.

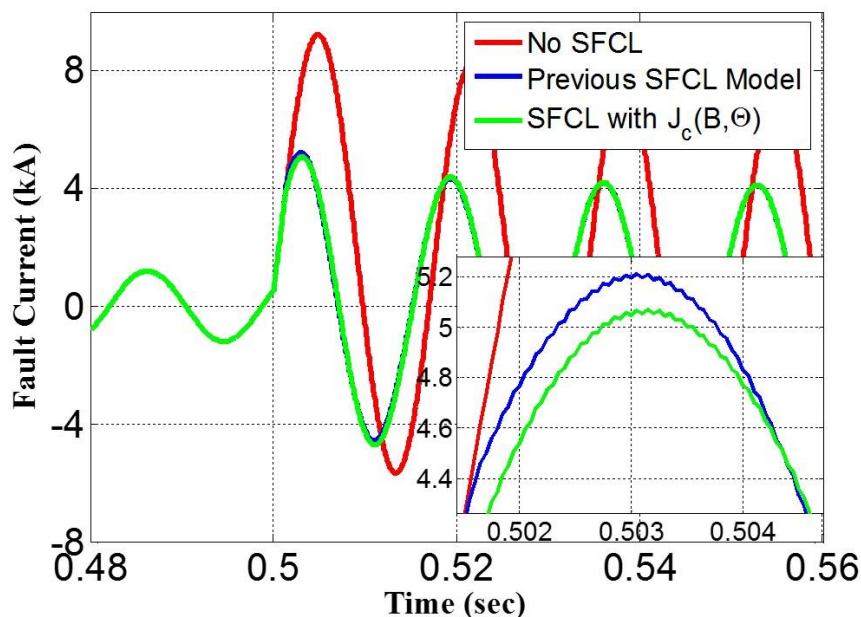


Figure 5.8: Comparison between current limiting performance of the original E-J power law RSFCL model and the E-J model with $J_c(\theta, B)$ dependence. The fault level without RSFCL is 9 kA. ($\theta = 90^\circ$, magnetic field perpendicular to the ab-plane)

As can be seen from Figure 5.8, adding of the $J_c(\theta, B)$ dependence of the HTS conductor into the RSFCL model still can make the quench process of the RSFCL faster, but the acceleration effect was less distinct in this case. Compared with the original model, the first peak only decreased by 6%. The reason is quite straightforward: the magnetic field generated by the conductors was smaller in this case since the magnitude of fault current was lower.

The influence of integrating the $J_c(\theta, B)$ dependence of the HTS material into the RSFCL model varies with many factors, such as capacity of the device, property of the material, structure of the current limiting module. Nevertheless, considering the high fault current that the RSFCL needs to bear and the trend that the fault level will keep increasing, there is no doubt that this study is of great importance for the simulation and design of the RSFCLs.

5.7 Conclusions

This chapter presents a thorough study of the magneto-angular dependence of the in-field critical current function in the so-called Lorentz configuration, $I_c(B, \theta)$ with $B \perp I$, of ten different samples of commercially available 2G-HTS tapes. The experimental results have been obtained for external magnetic fields of up to 400 mT, and range from 0° to 90° , i.e., with B parallel to the ab-plane of the YBCO tape, towards the perpendicularity conditions where B is parallel to the c-axis. In general, we have selected 2G-HTS tapes with broad differences regarding their width, fabrication process, and laminar structure (materials composition), in order to seek for a universal function that may describe the $I_c(B, \theta)$ behaviour of different commercial tapes from the numerical minimization of the objective functions introduced in equations 5.3 and 5.4. The obtained magnetic field-angular dependence of critical current of HTS samples was applied in the simulation of RSFCs behaviours, showing unneglectable effect on the first peak limiting performance during faults. This study is helpful to the design and simulation of RSFCLs and other HTS applications which require superconducting wires operating inside magnetic fields.

Chapter 6

Active Quenching Technique Developed for RSFCLs: Quench Acceleration and Protection

The application of resistive-type superconducting fault current limiters (RSFCLs) in electrical networks is very attractive due to their relative compactness, light weight, and good performance. However, this technology still has drawbacks: asymmetrical quench, uncertain limiting velocity, passive action, and incapability of enlarging capacity. Here, we present an active quenching technique which can potentially solve these problems. The quenching process is triggered using high frequency (HF) AC fields, which are generated by two coupled copper coils attached on both sides of the YBCO sample.

6.1 Introduction

As stated in previous chapters, the resistive-type SFCL (RSFCL) is one of the most promising choices among all types of SFCLs that have been developed. Due to its structural advantages, RSFCLs can be built very compact and light-weight, and the continuous drop of prices for 2G coated conductors keeps lowering their manufacturing costs. There are many RSFCLs that have been built and tested, showing good performance at limiting short-circuit faults. However, a few limitations still exist for this technology. First, the critical current properties of high temperature superconducting (HTS) wires are not uniform in both horizontal and perpendicular directions. Therefore, the wires may quench unevenly during faults, leading to regional overheating or even irreversible damage. This problem can be reduced by adding stabilizer into HTS tapes, but insertion of a metal stabilisation layer also reduces the

normal resistance of RSFCLs [175]. Second, RSFCLs are passive devices since their quench actions are determined by characteristics of the HTS wires. It is therefore not possible to precisely set the triggering current in advance. Third, to guarantee effective current limiting performance, the capacities of RSFCLs have to be designed based on features of present electrical systems, which means considerable upgrade costs are unavoidable with the expansion of power grids. Forth, the quench velocity cannot be controlled. In cases where faults are not severe, the RSFCLs may not be able to quench fast enough to limit the first peaks of short-circuit current [176].

We have developed and tested a high frequency (HF) field-assisted quench approach that helps mitigate these drawbacks of RSFCLs. Two coupled copper coils were fabricated to carry HF AC current with frequency ranging from 10 kHz to 100 kHz. By attaching at both sides of the YBCO sample, the two copper coils could provide various HF fields to trigger the active quenching process. Then, the device was placed in a DC magnet, in order to test how the HF-assisted quench behaviour of the sample is influenced by external DC fields of different intensities and directions. Using this technique, the tape quenched uniformly with a high velocity, and pre-set of triggering current was also achieved. Moreover, it can be expected that with this design, electrical grid operators can leave certain margin while choosing capacities of RSFCLs. Thus, when the scale of power systems is expanded, they can increase magnitudes of the triggering current instead of replacing all the equipment, so operating costs could be considerably reduced.

6.2 Experimental System

Figure 6.1 is a schematic drawing of the entire experimental system, and Figure 6.2(a) shows installation of the sample holder on the frame of the DC field magnet. The two coupled copper coils wrapped around a superconducting wire are demonstrated in

Figure 6.2 (b). The 10 mm wide YBCO tape used in this experiment was manufactured by Shanghai Superconductor Technology Co., Ltd. (SHSC) [177]. Measurement showed that its self-field critical current was 290 A with a critical electric field criterion $E_0 = 1 \times 10^{-6} V/cm$. The total length of the studied sample was set at 180 mm. Two copper coils made from 18 strands $\varnothing 0.5$ mm wire were coupled together and pressed tightly on the tape surface. Their combined resistance and inductance were $80 m\Omega$ and $9.6 \mu H$ at 77K, respectively. To minimize the effect of heat generated by the coupled coils, two layers of insulating tape were pasted on the HTS sample side of each copper coil. Then, both the HTS tape and the coupled coils were installed in the sample holder. To guarantee ideal electrical connection, 40 mm tape from each terminal was surrounded by high purity indium and clamped by copper plates. The joint resistance was measured to be $0.2 m\Omega$. Finally, the sample holder was mounted on the shelf of a 600 mT electromagnet below a high precision rotary stage, which had a graduation of 1° and Vernier of $5'$.

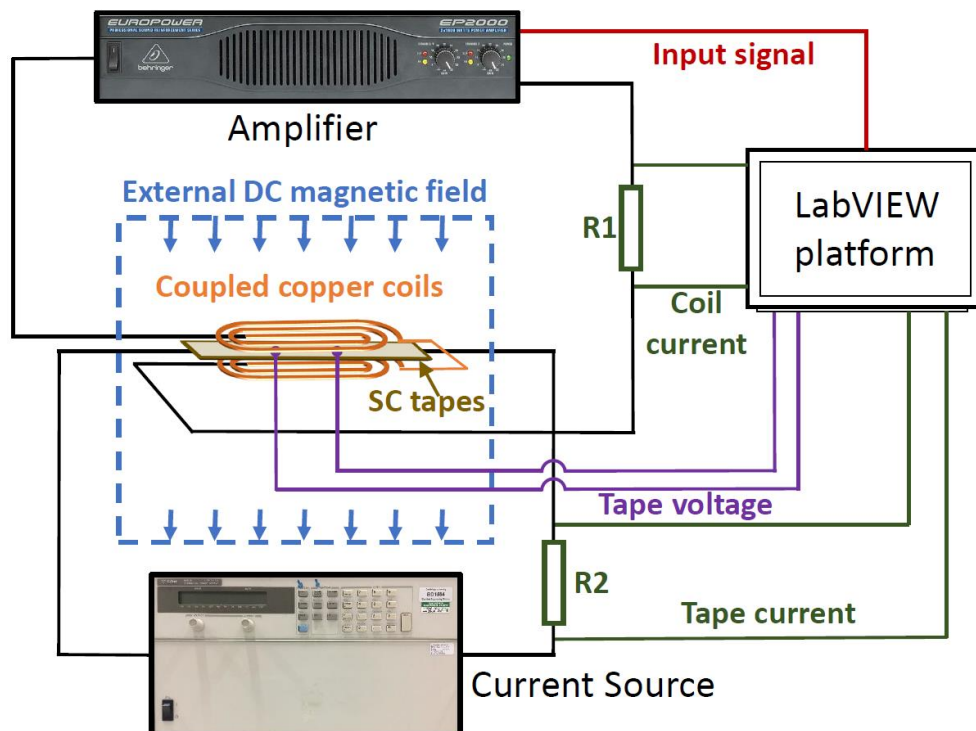


Figure 6.1: Schematic drawing of the experimental system.

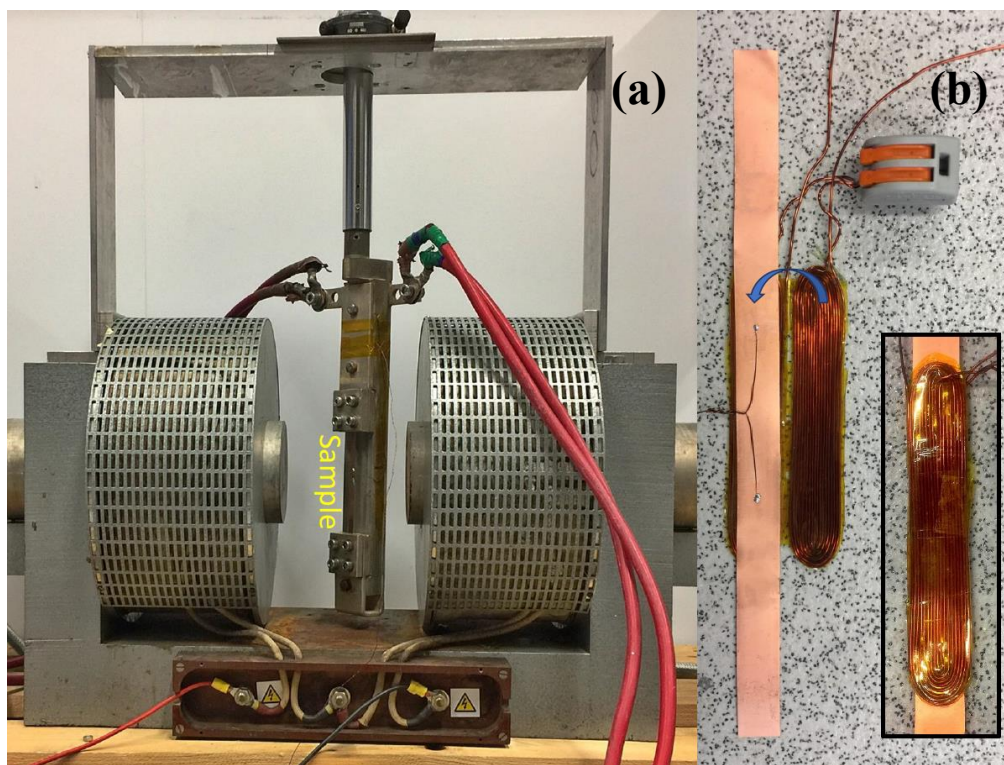


Figure 6.2: (a) Picture of the sample holder in the air gap of the field magnet. (b) Picture of the 2G HTS tape that placed in the middle of two coupled copper coils.

The controlling logic of our experiment can be explained as follows. For the superconducting loop, an Agilent 6680A was used as DC current source to provide transport current for the HTS wire. To monitor the status of the tape, two voltage taps were soldered on the surface of YBCO sample 50 mm apart. The HF signals injected into the coupled coils were produced by the LabVIEW platform and then amplified to different magnitudes by a Behringer EP4000. With the HF signals, the copper coils can generate an AC magnetic field on the ab-plane of the HTS wire. Then, the influence of the HF AC field on the quench behaviour was studied. The experiment was conducted in a liquid nitrogen bath.

6.3 Study of Quench Triggered by HF AC Magnetic Field

6.3.1 Transient study of the quench development

Many factors such as frequency, intensity and duration of the HF AC magnetic field, as well as the transport current carried by the HTS tape influence the quench characteristics of the YBCO sample [178]. To systematically study the impact of each of them, a series of experiments without external DC magnetic field was conducted. First, we chose frequency and intensity of the HF AC magnetic field to be $f = 50 \text{ kHz}$ and $B = 20 \text{ mT}$, and transport current of the tape $I = 150 \text{ A}$. By gradually increasing duration of the applied AC field, the process of quench development of the YBCO tape could be clearly observed.

Figure 6.3 shows voltage responses of the sample to the HF AC magnetic field with different durations. The distortion in curves was caused by insufficient sampling frequency of our Data Acquisition (DAQ) card. Normally, sampling frequencies ten times higher than the original signal should be used to acquire ideal waveform, but the highest sampling frequency we were able to achieve with our DAQ card was 80 kHz , 1.6 times the frequency of the applied AC field. However, this fact did not affect the accuracy of our experiment, since there was no need to record all signals precisely. For studying quench characteristics of the YBCO conductor, the DC component of the tape voltage and how it changes at with the applied AC field were determining factors. Recording data at 80 kHz is well beyond precision demands for our purpose, therefore our experimental results can be considered reliable.

As can be seen from Figure 6.3, an alternating voltage between the two voltage taps appeared immediately after applying the HF AC magnetic field. The biased voltage signal was composed of two parts: the induced voltage generated in the voltage

measurement circuit, and the voltage caused by dynamic resistance (with a DC component) [179]. When the AC field was applied for 5 ms, the peak value of biased voltage raised up to 150 mV first and then dropped to zero almost instantaneously at the end of AC signal.

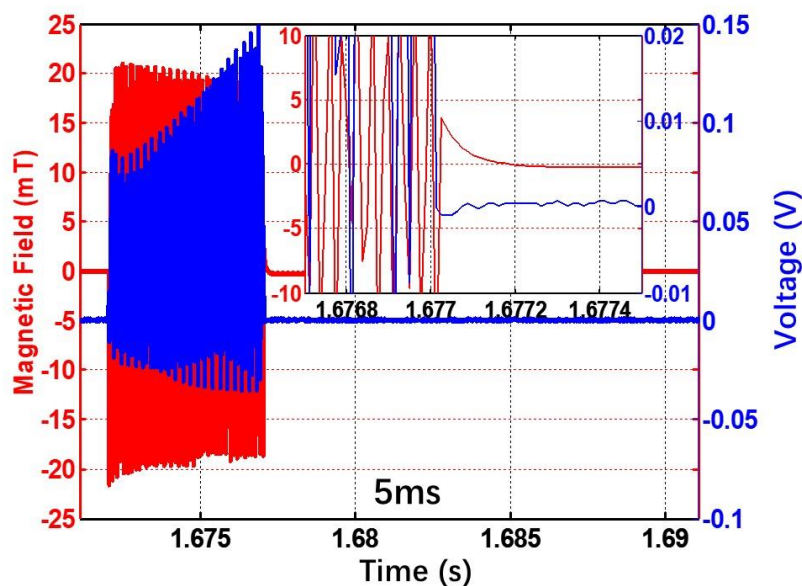


Figure 6.3: Dynamic voltage characteristics of the YBCO wire under HF AC magnetic field. The YBCO wire was carrying transport current of 150A. The frequency and intensity of the HF AC field were 50 kHz and 20 mT, respectively. The magnetic field was applied for 5 ms.

Then, with the duration of applied field increased to 9 ms, a noticeable delay in sample recovery was found. As shown in subfigure of Figure 6.4, it took 4 ms for the tape voltage to disappear.

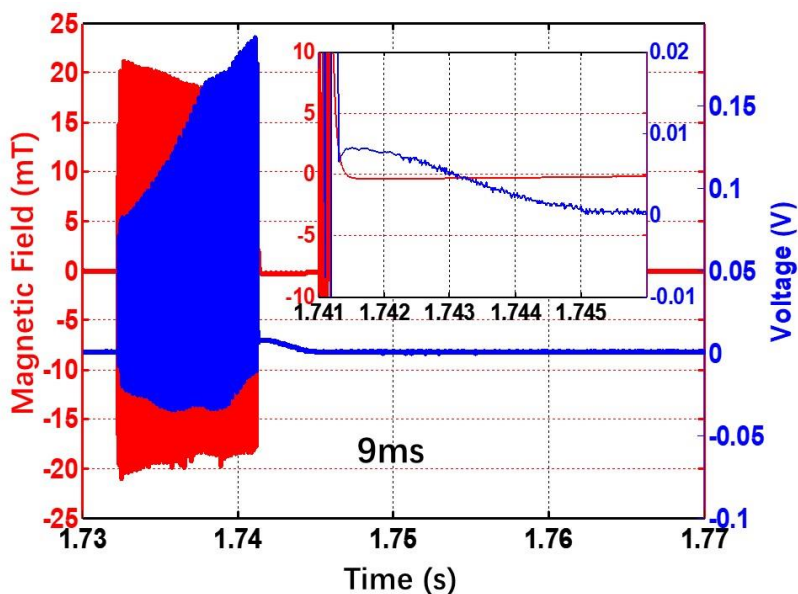


Figure 6.4: Dynamic voltage characteristics of the YBCO wire under the HF AC magnetic field of 9 ms.

However, under the effect of a 10 ms long AC field, different behaviour was observed. The sample tended to recover without the applied field, but its voltage increased rapidly after a small drop, and finally led to quench of the entire tape (Figure 6.5).

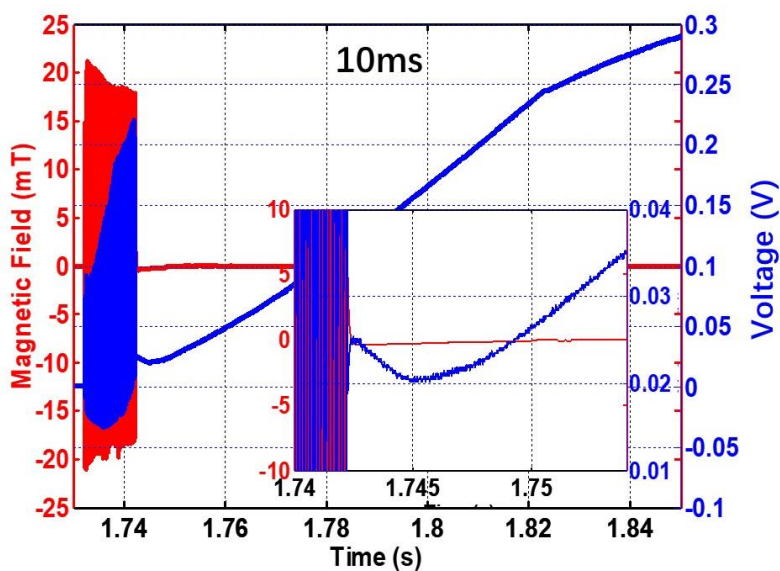


Figure 6.5: Dynamic voltage characteristics of the YBCO wire under the HF AC magnetic field of 10 ms.

This result implies that the conductor was already in an unstable state due to influence of the HF AC signal. After termination of applied field, the heat generation rate inside the YBCO wire was still higher than the heat dissipation rate, therefore quench became unavoidable due to the snowball effect. Figure 6.6 demonstrates that when the AC field was further lengthened, the peak-to-peak value of the tape voltage does not increase anymore, but the magnitude of DC component keeps growing constantly, resulting in a faster quench at the end of the applied field.

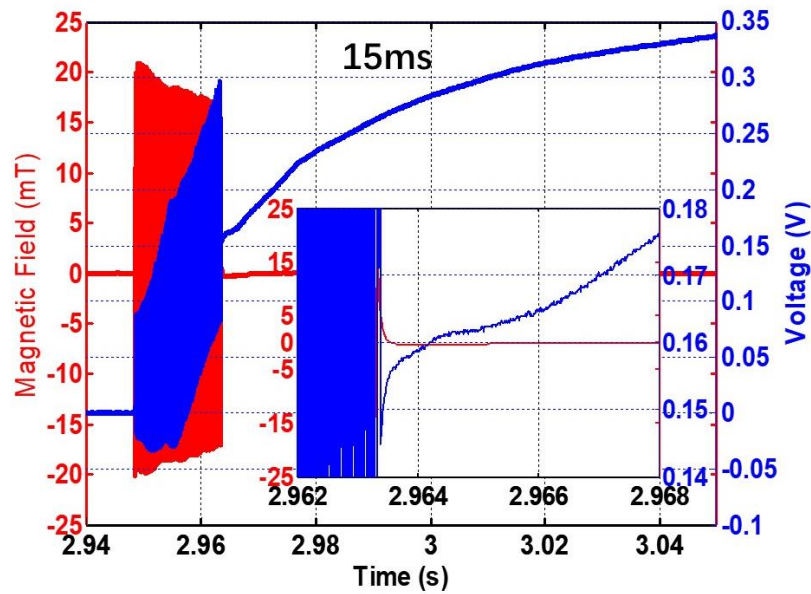


Figure 6.6: Dynamic voltage characteristics of the YBCO wire under the HF AC magnetic field of 15 ms.

The quench of the 2G HTS tape was mainly caused by its thermal instability. Under the combined effect of the applied HF AC field and the transport current, several sources contributed to the heat generation and the corresponding temperature rise. First, the change in external magnetic field generated a loss inside the superconductor, which can be considered as dynamic resistance [179-181]:

$$R_{dyn} = \frac{2afL}{I_{c0}} \left(B_a + \frac{B_a^2}{B_0} \right) \quad (6.1)$$

where a is the width of the sample, f is the frequency of the applied AC magnetic field, L is the interaction length of the AC field with the YBCO tape, which refers to the length of the coupled coils in our experiment. I_{c0} describes the critical current of the studied sample, and B_0 is the empirical constant of magnetic field used in Kim Model.

Although the copper coils lost ~80% of their room temperature resistance when immersed in the liquid nitrogen bath, the heat transferred from the coils to the sample still cannot be neglected. In addition, AC magnetization loss in the superconductor contributed to the heat generation, and the copper stabilizer of the sample also generates non-negligible eddy-current loss under HF AC magnetic field [182]. These sources acting together caused temperature rise of the YBCO tape. After enough heat is accumulated, the critical current of the tape is reduced to near the transport current. Then, the sample enters the flux flow state and starts to generate heat because of the emerging flux flow resistance. This leads to an increase of temperature at a higher rate [183]. The heat dissipation of the YBCO tape was mainly due to heat transfer between the tape surface and liquid nitrogen. When heat generation was too high the liquid nitrogen vaporized. Since the intervals between YBCO sample and copper coils were very narrow, the nitrogen bubbles got trapped, which significantly weakened the heat dissipation capability. This positive feedback considerably accelerated the heat accumulation process and finally gave rise to quench of the entire tape.

6.3.2 Study on influence factors of the quench time

As stated in Section 6.3.1, there were three factors which influenced the quench time of the sample: the magnitude of the transport current, and the frequency and the intensity of the applied HF AC magnetic field. To investigate their relationship with the quench time, a series of experiments was conducted with the following parameters: transport current of 50 A, 100 A, 150 A and 200 A; frequency of AC field at

10 kHz, 20kHz, 50 kHz and 100 kHz; intensity of AC field ranging from 10 mT to 50 mT. Due to capacity constraints of the amplifier, a high intensity of the AC field gradually became unachievable with increase of the field frequency. However, the experiments that we were able to perform were very representative and more than enough for the analysis. All results about the quench time are shown in Table 6.1.

Table 6.1: Variation of quench time along with change in transport current and applied HF AC magnetic field

(a) Transport Current: 50A						(b) Transport Current: 100A					
	10mT	20mT	30mT	40mT	50mT		10mT	20mT	30mT	40mT	50mT
10kHz	No	106ms	64ms	41ms	26ms	10kHz	No	87ms	32ms	16ms	10ms
20kHz	No	74ms	40ms	25ms		20kHz	No	36ms	14ms	9ms	
50kHz	No	52ms				50kHz	No	25ms			
100kHz	No					100kHz	197ms				
(c) Transport Current: 150A						(d) Transport Current: 200A					
	10mT	20mT	30mT	40mT	50mT		10mT	20mT	30mT	40mT	50mT
10kHz	No	27ms	19ms	13ms	6ms	10kHz	107ms	13ms	9ms	7ms	4ms
20kHz	102ms	20ms	10ms	5ms		20kHz	53ms	9ms	5ms	4ms	
50kHz	84ms	11ms				50kHz	44ms	6ms			
100kHz	72ms					100kHz	38ms				

Unlike in [184] where the frequency of applied magnetic field was more than 100 kHz, we found that one tenth of their predicted value was high enough to trigger the quench process, as can be seen from each sub-table. This finding is important for the promotion of this technology. Moreover, the time required for the YBCO tape to quench kept decreasing when the frequency or the intensity of applied magnetic field was increased. For instance, Table 6.1(d) shows that while the frequency remained at 10 kHz and the field intensity was increased from 10 mT to 50 mT, the quench time of the sample dropped significantly from 107 ms to 4 ms. Similarly, after we

increased the frequency of 10 mT/ 10 kHz AC magnetic field to 100 kHz, the quench time of the sample dropped from 107 ms to 38 ms.

The reason can be explained as follows. As we have stated in the previous section, the quench was triggered mainly by dynamic resistance loss, magnetization loss, eddy-current loss in the copper stabilizer, flux flow resistance loss, and heat transferred from the coupled coils to the sample. Since the dynamic resistance, magnetization loss and eddy-current loss are all in direct proportion to the frequency of applied field, the heat generation rate rises with an increase in frequency. Therefore, the quenching process is shortened correspondingly. In contrast, these three heat sources and the heat generated in coupled coils are directly proportional to the square of the field intensity. Hence, a more obvious acceleration effect is observed when the field intensity is enhanced.

Under the same applied field, the higher the transport current, the faster the quenching process will be. This happens for two reasons. First, when a high transport current is flowing, less heat is required by the sample to enter flux flow state. Hence, less time will be needed for the YBCO tape to quench. Second, according to Oomen [181], Equation 6.1 is valid only if the intensity of applied AC field is higher than the full penetration field of the HTS sample. In other words, the applied field must be stronger than a threshold value, so that it can interact with the transport current carried by the tape. A higher transport current means a lower threshold field for the generation of dynamic resistance, and therefore the sample can quench faster under the same AC magnetic field. This is also a main reason that in half of the 10 mT cases the magnetic field is not capable of triggering the quenching process: an important heat source is missing since the field intensity is too low to overcome the threshold field.

As suggested by Vyacheslav F. et al [184], similar designs could increase the uniformity of quench and therefore increase the service life of HTS wires. This phenomenon was also found during our experiments. Under proper operation, the

studied sample quenched more than 150 times but still showed no noticeable degradation. The reason for this is that unprotected quench of a YBCO tape tends to start from defects and then propagates slowly. The low normal zone propagation velocity [185, 186] gives rise to extreme thermal stress near the defects, and then damages or even destroys an entire sample. However, due to the flux flow resistance caused by reduction of critical current and the dynamic resistance, quench processes initiated by an HF magnetic field always develop uniformly. Hence, the imbalance of thermal stress over the tape can be significantly reduced, and the service life can be accordingly extended. This characteristic makes the proposed quench initiation design very useful for the protection of current limiting devices like SFCLs.

Moreover, according to Table 6.1(d), when an HF magnetic field of $10\text{ kHz}/50\text{ mT}$ or $20\text{ kHz}/40\text{ mT}$ was applied, the quenching process can be triggered in 4 ms . This quench velocity is fast enough for SFCLs, but can still be improved on. Considering the limitation of our equipment, we speculate that further acceleration is possible with AC field of higher frequency and intensity. Moreover, in our experiment the transport current is fixed at 200 A. However, fault current flowing through SFCLs will be much higher during system faults, which means uniform flux flow states can be developed faster. With the capability of triggering quench so quickly, even taking into account delays caused by fault detection and HF field generation, SFCLs with application of this technique still can cut faults before their first peaks.

6.4 Study of Active Quench under Various External DC Fields

Previously we studied the angular-field dependence of critical current $J_c(\theta, B)$ of YBCO tapes, which demonstrated that the magnitude and direction of external DC magnetic field have significant impact on the critical current of studied samples [187]. Combining that conclusion with the present study, we believe that DC background field might be able to accelerate the HF-assisted quench. If true, this technique will be of great importance for the potential applications of HF-assisted quench in RSFCLs. The reason is that, due to the large amount of HTS conductor in RSFCLs, the copper coils used for generation of AC signals must be quite long for protecting the full length of superconductor. It is well known that an increase in wire length leads to growth of resistance and inductance, which means it will be more difficult to generate HF signals in them. However, if the DC background field can cooperate with the HF AC field, then the specification for the AC power supplies can be accordingly reduced. Since providing a static magnetic field is much easier, the entire system will be much cheaper and less technically sophisticated. However, it should be noticed that although the DC magnetic field provides advantage, it can only assist the HF AC field instead of replacing it, since the DC field is not able to guarantee HTS tapes quenching uniformly.

6.4.1 Field-angular dependence of critical current of the studied sample

To explore HF-assisted quench of the sample under external DC magnetic field, firstly we investigated critical current characteristics of the sample inside various DC fields and orientations. In our previous research we had generalized a fitting function

which was capable of accurately describing the $I_c(\theta, B)$ relationship of 2G HTS tapes [187]:

$$I_c(\theta, B) = I_{c0} \left[1 + \varepsilon_\theta \left(\frac{B}{B_0} \right)^\alpha \right]^{-\beta} \quad 6.2$$

with

$$\varepsilon_\theta = \sqrt{\gamma^{-2} \sin^2(\theta) + \cos^2(\theta)} \quad 6.3$$

where $I_{c0} = I_c(0, \theta)$ is the critical current in self-field, B is the norm of the magnetic field intensity, B_0 and β are empirical parameters proposed by Kim [21]. In addition, a variable α is introduced to make this fitting approach more general and more accurate. The applied field was also scaled by ε_θ , a function formed based upon the electron mass anisotropy ratio of the material $\gamma^2 = m_c^*/m_{ab}^*$ [172].

For validation of Equation 6.2, in total we studied ten YBCO tapes manufactured by different companies which had different structures. The precise fitting results of all samples convincingly showed the universality of the approach we proposed. Using this method, the magnetic-angular dependence of the critical current of the sample we used in this study was measured and fitted, as plotted in Figure 6.7.

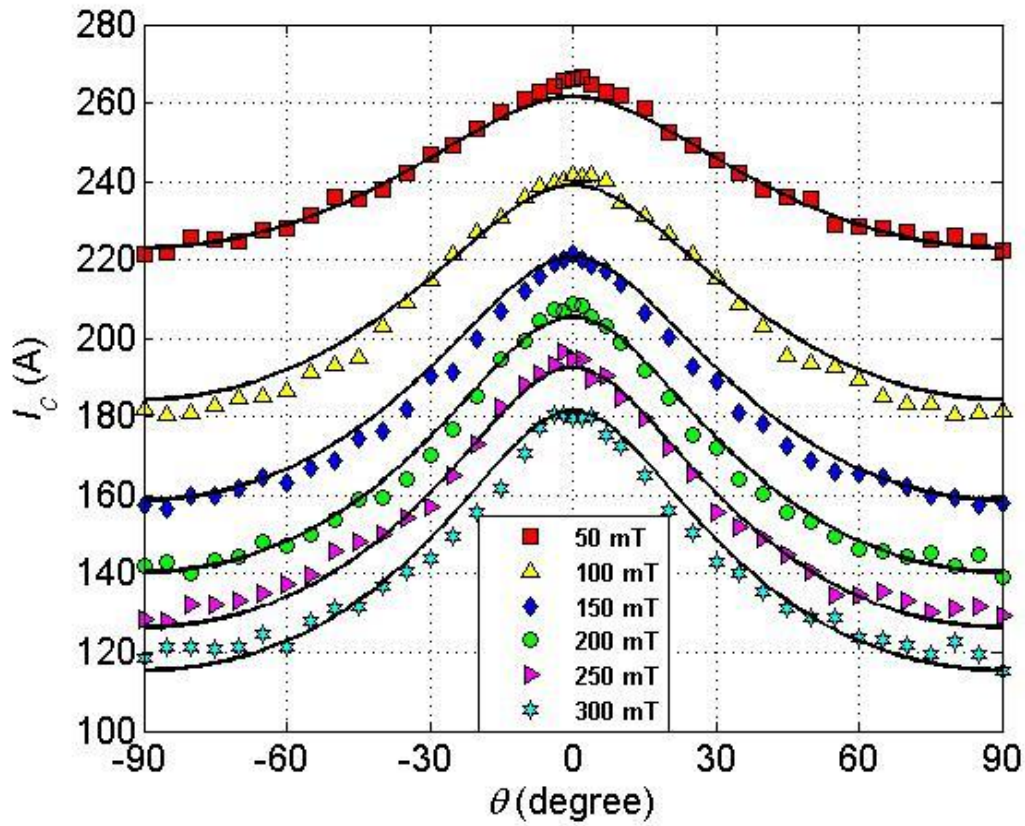


Figure 6.7: In-field magnetic-angular dependence of the studied sample: experimental data (symbols) and fitting curves (solid lines). Experimental measurements at less important angles were not plotted for clarity.

It can be seen from Figure 6.7 that the sample exhibited peaks when the external magnetic field was parallel to the film surfaces ($B // ab$), and valleys while the DC field was parallel to the c -axis ($B \perp ab$). In the extreme condition of our experiment, e.g. when the sample was placed in a 300 mT DC background field perpendicular to the ab -plane, the critical current decreased from 290 A to 120 A . When the 300 mT magnetic field was parallel to the ab -plane, it still caused a $\sim 40\%$ reduction in the critical current (to 180 A). Based on the general fitting approach expressed by Eq. (2) and Eq. (3), the in-field critical current characteristics of the YBCO tape can be described as: $I_c(\theta, B) = 290 \times [1 + 0.35 \times (B/110)]^{-0.7}$. This fitting result is very precise since the mean absolute percentage deviation is only 1.28%.

6.4.2 Relationship between the quench time and the intensity of DC background field

Two aspects of the DC magnetic field influence quench behaviour of HTS tapes, namely the intensity and the angle. To investigate relationship between the quench time and the field intensity, the DC field was set to be perpendicular to the ab-plane of the sample. Then, we fixed transport current at 100 A and HF AC field intensity at 10 mT , which left two variables in the experiment: the frequency of HF AC field and the magnitude of DC field. The quench times we obtained with this setup are plotted in Figure 6.8.

As can be seen from the figure, while DC magnetic field remained unchanged, the increase of the frequency of HF AC field always reduces the quench time. In addition, the quench process triggered by the same HF signal accelerated almost linearly when the DC background field became stronger. The reason for the first observation was previously stated in Section 6.3.2, that the heat generation rate grows along with the rise in AC field frequency. The second phenomenon was mainly because that the existence of DC magnetic field causes a drop in the critical current of studied sample, and a lower critical current means faster heat generation and faster entrance to flux flow state.

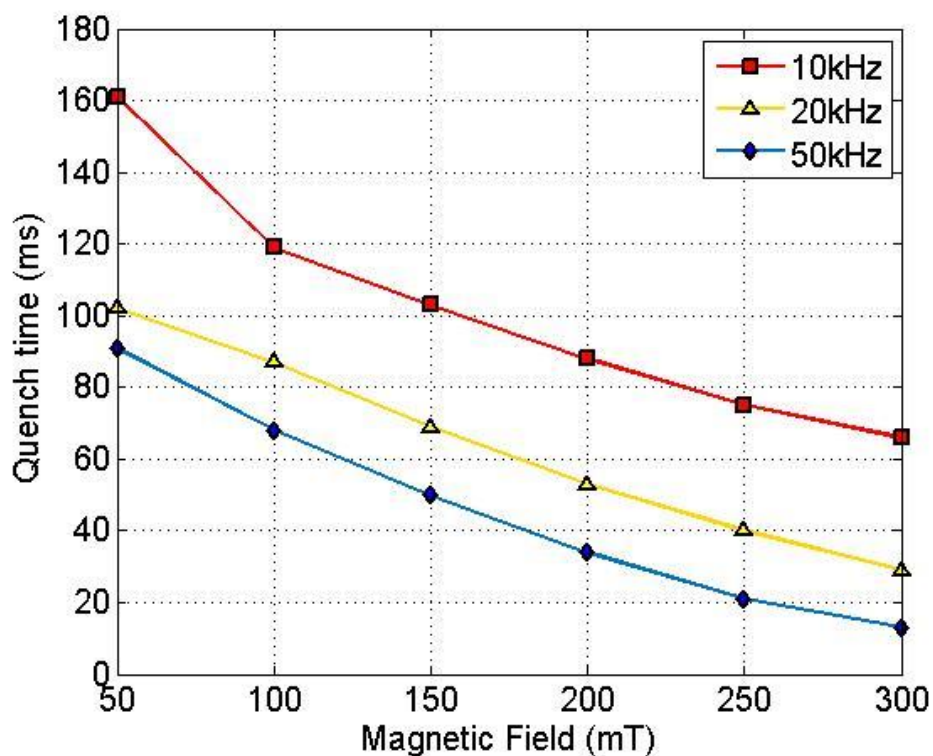


Figure 6.8: Reduction in quench time caused by the increase of DC field intensity and the HF AC field frequency. The transport current remained at 100 A and the intensity of HF AC field was set at 10 mT . The direction of DC field was always perpendicular to the sample surface.

According to Table 6.1(b), if the frequency is lower than 100 kHz , an HF AC field of 10 mT does not quench a sample carrying transport current of 100 A . However, under external DC magnetic fields, quench of the sample could always be accomplished, as demonstrated in Figure 6.8. To be more specific, with a 300 mT DC background field, the 10 mT , $10/20/50\text{ kHz}$ HF AC signals triggered quench processes within $67/29/13\text{ ms}$. These durations were shorter than that achieved using 20 mT , $10/20/50\text{ kHz}$ HF signals without assistance of DC fields, which was 87 ms , 36 ms and 25 ms , respectively. This shows that a DC field can accelerate the HF-assisted quench. In other words, with the same performance requirement, applying DC background fields can ease demands for AC power sources, and therefore significantly reduce cost of the system.

Then, to see how the transport current influences the quench time, the sample was placed under different DC background fields while carrying different current. The AC field was set to be $10\text{ kHz}/20\text{ mT}$. This group of experimental results were gathered in Figure 6.9.

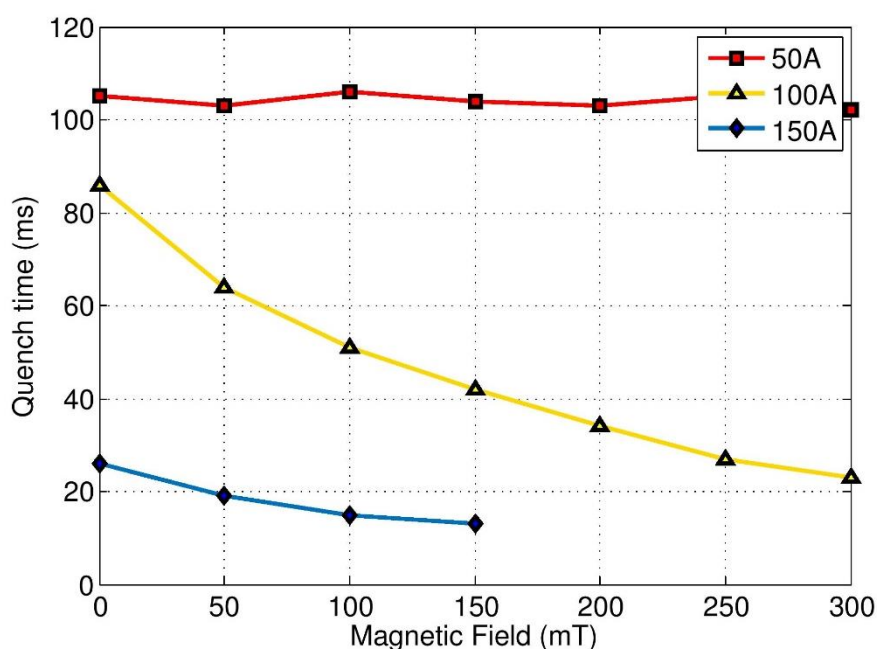


Figure 6.9: Quench time of the sample when quench processes were triggered by $10\text{ kHz}/20\text{ mT}$ AC magnetic field. The experiments were conducted when the sample was placed in different DC background fields and carried different transport current. See Figure 6.7 for the data of I_c for the sample.

As shown in Figure 6.9, when the magnitude of transport current changed, the effects of quench acceleration caused by the increase of DC field intensity became markedly different. To begin with, the transport current of the studied sample was set to be 50 A . By enhancing the DC background field from 0 to 300 mT , there was only a slight decrease in quench time. This was mainly because that the critical current of the sample under 300 mT DC field was much higher than 50 A , so the heat generation was still small due to low-energy AC signal and low transport current. By considering the redundant cooling capacity and the boiling-off characteristics of liquid nitrogen, the

small amount of excess heat brought by the rise of DC field is consumed relatively fast. Hence it barely had any effect on the quench time. However, the situation became different after we increased the transport current to 100 A. Originally, it took the HF AC signal 87 ms to quench the sample. Under the influence of a 300 mT DC background field, a 74% reduction of the quench time was observed. The reason is similar to the explanation of the phenomenon shown in Figure 6.8. In addition, it can also be noticed that with a higher transport current (150 A) the acceleration effect got weaker again with the quench time dropping from 27 ms to 12 ms. According to these results, we conclude that the performance of adding DC background field is dependent on the amplitude of transport current and properties of HF AC signals. Therefore, when designing a quench system for RSFCLs using this technique, the magnitude of both the AC and DC field should be chosen carefully to achieve optimal performance with the least cost and complexity.

6.4.3 Relationship between the quench time and the angle of DC background field

We investigated the relationship between the quench characteristics and the angle of DC magnetic field. The magnitude of the HF AC field was fixed at 10 mT, with frequency of 10 kHz, 20 kHz or 50 kHz. To observe the angular dependence clearly, we set the DC field intensity at 300 mT. The DC field was always perpendicular to the transport current, which is the maximum Lorentz force configuration. The field angle θ is defined as 0° while the DC field parallel to the ab-plane of the sample. We measured the quench time for every 5° near the centre (from -10° to 10°) and every 10° at other angles. The experimental results were shown in Figure 6.10.

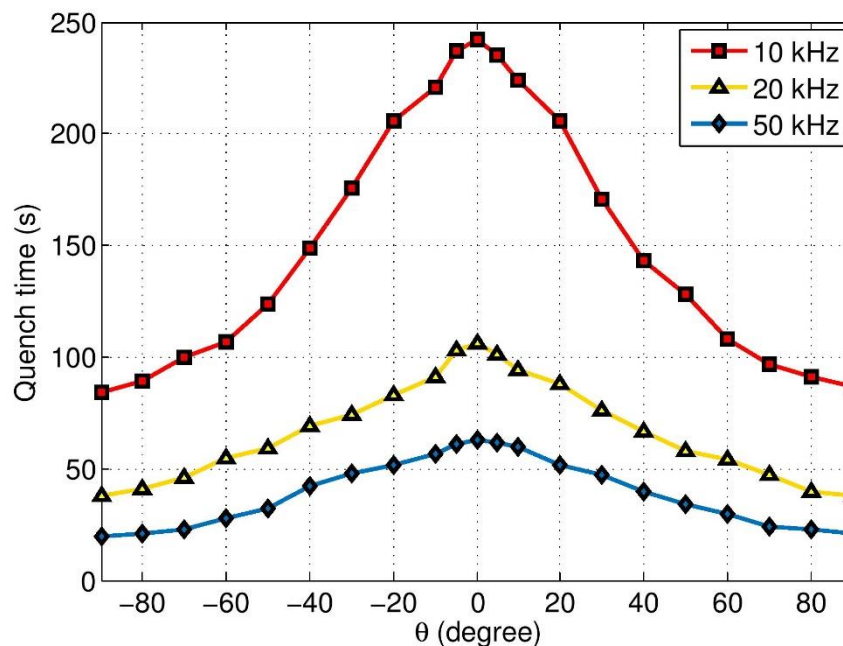


Figure 6.10: Angular dependence of quench time under 300 mT DC background field. The sample carried 100 A transport current, and its quench procedures were triggered by 10 mT HF AC magnetic field with frequency of 10 kHz , 20 kHz and 50 kHz .

As can be seen from Figure 6.10, no matter the AC field frequency, the quench time was always considerably influenced by the angle between the DC magnetic field and sample surface. The 10 kHz AC signal applied parallel to the ab-plane of the sample quenched the tape in 241 ms . However, with a 90° AC field this figure dropped to 76 ms , which means the quench time was reduced by 68%. The curve of quench time triggered by 20 kHz signal appeared to be flatter than the 10 kHz case, but nearly the same decline proportion 65% (103 ms and 37 ms , respectively) was observed. Similar behaviour was found with the 50 kHz scenario. Along with the rotation of AC triggering signal from 0° to 90° , the quench time decreased by 67% from 66 ms to 21 ms . It can be concluded that within the studied frequency range, the quench time can be reduced more than 60% by adjusting the direction of the 300 mT DC field. During the design of potential applications, this should be carefully considered to guarantee optimal performance.

6.4.4 Magnetic field-angular dependence of the quench time

In previous subsections we have separately studied how the quench time is influenced by the intensity and the angle of DC background field. The next step was to produce a comprehensive figure, which can provide a clearer understanding of DC field intensity dependence and angular dependence of the quench time simultaneously. We used transport current of 100 A and fixed the HF AC magnetic field to be $10\text{ kHz}/20\text{ mT}$. For DC background field of each intensity between 50 mT and 300 mT (with intervals of 50 mT), the quench time was recorded with angles ranging from -90° to 90° . This information about the anisotropic field dependence of quench time is plotted in Figure 6.11.

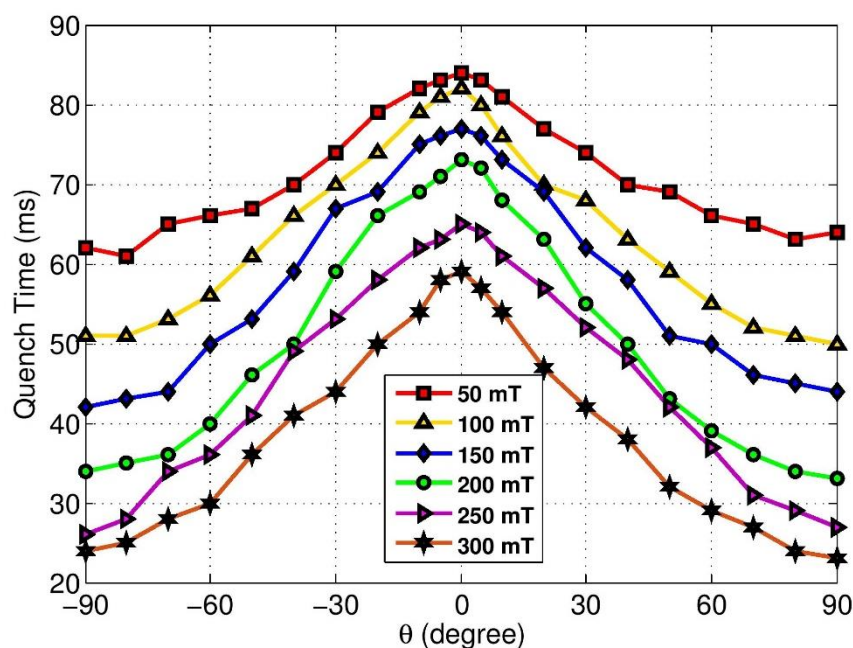


Figure 6.11: Magnetic field-angular dependence of quench time of the YBCO sample. The transport current of the tape was 100 A and the HF AC field used to trigger quench processes was $10\text{ kHz}/20\text{ mT}$.

Figure 6.11 demonstrates that applying a DC background field always reduces the quench time regardless of the field intensity. According to Table 6.1, the tape needed 87 ms to quench without assistance of the DC field. Under field of 50 mT , this

value dropped to 63 *ms*, showing more than 25% increase in quench speed. Moreover, with the 300 *mT* DC field perpendicular to the ab-plane of the tape surface, the quench process could be triggered within 24 *ms*, only a quarter of the original figure. In addition, the anisotropy of quench time was relatively large and kept growing with the increase of DC field intensity. As can be seen from the comparison between Figure 6.7 and Figure 6.11, this phenomenon is in accordance with the $J_c(\theta, B)$ dependence of the sample. Figure 6.7 shows that under DC magnetic field from 50 *mT* to 300 *mT*, the percentage deviations between critical current at 0° and 90° are 17%, 25%, 27%, 31%, 35%, and 34%. Correspondingly, the percentage deviations between quench time at 0° and 90° DC background field are 24%, 39%, 45%, 52%, 58%, and 58%. The two sets of data are roughly in proportion, but the anisotropy of the quench time is greater. This is mainly because both the dynamic resistance loss and the magnetization loss in superconductor increase with a drop of critical current. It becomes easier for the tape to enter the flux flow state, and the sample starts to generate heat due to flux flow resistance. Based on this result, we deduce that with different transport current and different HF AC signal, the magnetic field-angular dependence of the quench time would follow the same pattern.

6.5 Conclusions

An HF AC-assisted quench study of a YBCO conductor was presented in this chapter. The development process of the quench triggered by AC magnetic field was recorded, and the quench time relationship with the transport current and the AC field was studied. Unlike the deduction given in [26], we found that AC signals of 10 *kHz* could trigger quench of the HTS tape. Also, the device proved to be effective at guaranteeing uniform quench of the sample. Our experiments showed that the efficiency of quench was in direct proportion to the current carried by the YBCO wire, the intensity and the frequency of the HF AC magnetic field. Based on these observations, it is concluded

that the quench procedures were developed mainly due to dynamic resistance loss, magnetization loss, eddy-current loss in the copper stabilizer, flux flow resistance loss, and heat transferred from the coupled coils.

We placed the HTS sample and the coupled copper coils in a DC magnet, to study whether the quench process can be accelerated by the application of DC magnetic field. We found that with its direction constant, the DC field could effectively reduce the time required for quench, but its performance was dependent on the amplitude of transport current and characteristics of HF AC signals. In addition, the angle between the DC magnetic field and the tape surface had a huge impact on the quench time, which can be more than 60%. By applying both DC and an AC magnetic field, the total cost of the device can be considerably reduced. A comprehensive field-angular dependence of the quench time of studied sample was produced, revealing the same pattern as $J_c(\theta, B)$ dependence of the tape, but with a greater anisotropy. To summarize, this technique showed outstanding performance regarding quench acceleration and tape protection. We believe the HF-assisted quenching technology has a promising future in current limiting devices and hope our findings will be helpful for its potential applications.

Chapter 7

Conclusions and Future Work

This thesis presented a study of resistive superconducting fault current limiter and its application in power systems. The RSFCL is a novel device that can help to mitigate the increasing level of fault currents, therefore, it is extremely beneficial to have a deep understanding for its physical principles and current limiting behaviour in power systems, and improve its transient as well as recovery performance.

In Chapter 3, a power system model based on the Korean electric grid was built, and the transient analysis of short-circuit currents was explained. The operating principle of RSFCL and the detailed structure of a step-resistance RSFCL model were briefly introduced. To validate the current limiting performance of the SFCL module, wind farm protection schemes were studied under three fault scenarios: the distribution grid fault, the customer grid fault and the transmission line fault. After thorough analysis it was concluded that from both the economic and the technical point of view, the optimal allocating strategy of SFCLs for the studied power grid model is the application of one SFCL at the integrating point of the system model. With this arrangement, the fault currents can be effectively limited, and the DG source is not negatively affected.

Chapter 4 presented a comprehensive study on the performance and optimal allocation analysis of RSFCLs inside two power system models built based on the UK network standard. To assess the impact of incorporating SC material properties on the performance of SFCLs, three different models were used throughout the study: the step resistance model, the exponential resistance model, and the E-J power law model. Although computing time can be reduced when step-resistance and exponential equation models are used, such simplifications led to strong overestimations of the actual prospective performance of the SFCL and may result in wrong conclusion of

optimal installing strategies. Thus, this comparison showed that adequate physical properties for the electro-thermal dynamics of the SC materials should be considered to accurately predict behavior of SFCLs inside a power system. Systematic studies were then performed using the prospective strategies for the installation of one or more SFCLs. We have proven that installing more SFCLs does not necessarily mean better overall performance. For both power system models, the simultaneous use of three SFCLs is the best protection strategy in terms of the performance, economic efficiency and the reliability of the overall grid. To draw this conclusion, all the potential combinations of two, three, four, and five SFCLs were studied under a wide number of fault scenarios and measuring strategies.

In Chapter 5, a series of experiments were performed to study the magneto-angular dependence of the in-field critical current $I_c(B, \theta)$ with $B \perp I$, of ten different samples of commercially available 2G-HTS tapes. The experimental results were obtained for external magnetic fields of up to 400 mT, and range from 0° to 90° . In general, we have selected 2G-HTS tapes with broad differences regarding their width, fabrication process, and laminar structure (materials composition), to seek for a universal function that may describe the $I_c(B, \theta)$ behaviour of different commercial tapes. The obtained magnetic field-angular dependence of critical current of HTS samples was applied in the simulation of RSFCs behaviours, showing unneglectable effect on the first peak limiting performance during faults. This study is helpful to the design and simulation of RSFCLs and other HTS applications which require superconducting wires operating inside magnetic fields.

An HF AC-assisted quench study of a YBCO conductor was presented in Chapter 6. The development process of the quench triggered by AC magnetic field was recorded, and the quench time relationship with the transport current and the AC field was studied. We found that AC signals of 10 kHz could trigger quench of the HTS tape. Also, the device proved to be effective at guaranteeing uniform quench of the sample. Our

experiments showed that the efficiency of quench was in direct proportion to the current carried by the YBCO wire, the intensity and the frequency of the HF AC magnetic field. Based on these observations, it is concluded that the quench procedures were developed mainly due to dynamic resistance loss, magnetization loss, eddy-current loss in the copper stabilizer, flux flow resistance loss, and heat transferred from the coupled coils. After then, we placed the HTS sample and the coupled copper coils in a DC magnet, to study whether the quench process can be accelerated by the application of DC magnetic field. We found that with its direction constant, the DC field could effectively reduce the time required for quench, but its performance was dependent on the amplitude of transport current and characteristics of HF AC signals. In addition, the angle between the DC magnetic field and the tape surface had a huge impact on the quench time. By applying both DC and an AC magnetic field, the total cost of the device can be considerably reduced. A comprehensive field-angular dependence of the quench time of studied sample was produced, revealing the same pattern as $J_c(\theta, B)$ dependence of the tape, but with a greater anisotropy. To summarize, this technique showed outstanding performance regarding quench acceleration and tape protection. We believe the HF-assisted quenching technology has a promising future in current limiting devices and hope our findings will be helpful for its potential applications.

As for future work, it would be interesting to perform simulations to study how the installation of RSFCLs would influence the traditional fault detection schemes, and how the present protection devices should be regulated to cooperate with RSFCLs. In addition, the experiment of the active quenching technique was conducted with relatively low transport current. Hence, to further prove the effectiveness of the device, it would be helpful to investigate the performance of the active switch when the tape carries transport current higher than its critical current.

In conclusion, this thesis presents a comprehensive study of the RSFCL and its current limiting performance in power systems. This study can be extremely beneficial for the design, optimization and application of RSFCLs.

References

- [1] H. K. Onnes, "The superconductivity of mercury," *Comm. Phys. Lab. Univ. Leiden*, vol. 122, p. 124, 1911.
- [2] J. E. Kunzler, E. Buehler, F. a. Hsu, and J. H. Wernick, "Superconductivity in Nb₃Sn at high current density in a magnetic field of 88 kgauss," *Physical review letters*, vol. 6, no. 3, p. 89, 1961.
- [3] J. G. Bednorz and K. A. Müller, "Possible highT_c superconductivity in the Ba-La-Cu-O system," *Zeitschrift für Physik B Condensed Matter*, vol. 64, no. 2, pp. 189-193, 1986.
- [4] M.-K. Wu *et al.*, "Superconductivity at 93 K in a new mixed-phase Y-Ba-Cu-O compound system at ambient pressure," *Physical Review Letters*, vol. 58, no. 9, p. 908, 1987.
- [5] M. Subramanian *et al.*, "A new high-temperature superconductor: Bi₂Sr_{3-x}CaxCu₂O_{8+y}," *Science*, vol. 239, no. 4843, pp. 1015-1018, 1988.
- [6] M. Einaga *et al.*, "Crystal structure of the superconducting phase of sulfur hydride," *Nature physics*, vol. 12, no. 9, p. 835, 2016.
- [7] O. University. (2016). *Unraveling the crystal structure of a -70° Celsius superconductor; a world first.* Available: https://www.eurekalert.org/pub_releases/2016-08/ou-utc082316.php
- [8] W. Buckel and R. Kleiner, "Fundamental Properties of Superconductors," *Superconductivity: Fundamentals and Applications*, pp. 11-71, 2008.
- [9] D. Larbalestier, A. Gurevich, D. M. Feldmann, and A. Polyanskii, "High-T_c superconducting materials for electric power applications," *Nature*, vol. 414, no. 6861, pp. 368-377, 2001.
- [10] V. L. Ginzburg and L. D. Landau, "On the theory of superconductivity," *Zh. eksp. teor. Fiz*, vol. 20, no. 1064-1082, p. 35, 1950.
- [11] H. A. F. C. P. Poole, and R. J. Creswick, *Superconductivity*. Academic Press, 2007.

-
- [12] E. H. Brandt, "The flux-line lattice in superconductors," *Reports on Progress in Physics*, vol. 58, no. 11, p. 1465, 1995.
- [13] K. Fosshem and A. Sudbø, *Superconductivity: physics and applications*. John Wiley & Sons, 2005.
- [14] P. Gammel, D. Bishop, J. Rice, and D. Ginsberg, "Images of the vortex chain state in untwinned YBa₂Cu₃O_{7-δ} crystals," *Physical review letters*, vol. 68, no. 22, p. 3343, 1992.
- [15] R. French, J. Lowell, and K. Mendelssohn, "Almost ideal behaviour in some type II superconducting alloys," *Cryogenics*, vol. 7, no. 1, pp. 83-88, 1967.
- [16] H. Hess, R. Robinson, R. Dynes, J. Valles Jr, and J. Waszczak, "Scanning-tunneling-microscope observation of the Abrikosov flux lattice and the density of states near and inside a fluxoid," *Physical review letters*, vol. 62, no. 2, p. 214, 1989.
- [17] A. Yaouanc, P. D. de Réotier, and E. Brandt, "Effect of the vortex core on the magnetic field in hard superconductors," *Physical Review B*, vol. 55, no. 17, p. 11107, 1997.
- [18] S. Foltyn *et al.*, "Materials science challenges for high-temperature superconducting wire," *Nature materials*, vol. 6, no. 9, pp. 631-642, 2007.
- [19] C. P. Bean, "Magnetization of hard superconductors," *Physical Review Letters*, vol. 8, no. 6, p. 250, 1962.
- [20] C. P. Bean, "Magnetization of high-field superconductors," *Reviews of modern physics*, vol. 36, no. 1, p. 31, 1964.
- [21] Y. Kim, C. Hempstead, and A. Strnad, "Critical persistent currents in hard superconductors," *Physical Review Letters*, vol. 9, no. 7, p. 306, 1962.
- [22] Y. Kim, C. Hempstead, and A. Strnad, "Magnetization and critical supercurrents," *Physical Review*, vol. 129, no. 2, p. 528, 1963.
- [23] P. Anderson, "Theory of flux creep in hard superconductors," *Physical Review Letters*, vol. 9, no. 7, p. 309, 1962.
- [24] J. Bardeen and M. Stephen, "Theory of the motion of vortices in superconductors," *Physical Review*, vol. 140, no. 4A, p. A1197, 1965.

- [25] Y. Yoshida, M. Uesaka, and K. Miya, "Magnetic field and force analysis of high T_c superconductor with flux flow and creep," *IEEE transactions on magnetics*, vol. 30, no. 5, pp. 3503-3506, 1994.
- [26] Y. Yoshida, M. Uesaka, and K. Miya, "Evaluation of dynamic magnetic force of high T_c superconductor with flux flow and creep," *INTERNATIONAL JOURNAL OF APPLIED ELECTROMAGNETICS IN MATERIALS*, vol. 5, no. 1, pp. 83-83, 1994.
- [27] A. Gladun, G. Fuchs, K. Fischer, D. Busch, R. Eujen, and J. Huedepohl, "Critical current densities and activation energy of BiPbSrCaCuO tapes," *IEEE transactions on applied superconductivity*, vol. 3, no. 1, pp. 1390-1393, 1993.
- [28] J. Rhyner, "Magnetic properties and AC-losses of superconductors with power law current—voltage characteristics," *Physica C: Superconductivity*, vol. 212, no. 3, pp. 292-300, 1993.
- [29] S. Stavrev *et al.*, "Comparison of numerical methods for modeling of superconductors," *IEEE transactions on magnetics*, vol. 38, no. 2, pp. 849-852, 2002.
- [30] G. Didier and J. L  v  que, "Influence of fault type on the optimal location of superconducting fault current limiter in electrical power grid," *International Journal of Electrical Power & Energy Systems*, vol. 56, pp. 279-285, 2014.
- [31] A. Mahmoudian, M. Niasati, and M. A. Khanesar, "Multi objective optimal allocation of fault current limiters in power system," *International Journal of Electrical Power & Energy Systems*, vol. 85, pp. 1-11, 2017.
- [32] X. Zhang *et al.*, "Power flow analysis and optimal locations of resistive type superconducting fault current limiters," *SpringerPlus*, vol. 5, no. 1, p. 1972, 2016.
- [33] X. Zhang, H. Ruiz, J. Geng, and T. Coombs, "Optimal location and minimum number of superconducting fault current limiters for the protection of power grids," *International Journal of Electrical Power & Energy Systems*, vol. 87, pp. 136-143, 2017.
- [34] M. Noe and M. Steurer, "High-temperature superconductor fault current limiters: concepts, applications, and development status," *Superconductor Science and Technology*, vol. 20, no. 3, p. R15, 2007.

- [35] A. Kalinov, I. Voloshin, and L. Fisher, "SPICE model of high-temperature superconducting tape: application to resistive fault-current limiter," *Superconductor Science and Technology*, vol. 30, no. 5, p. 054002, 2017.
- [36] A. Neumann, G. Britain, and P. Power, *Application of fault current limiters*. BERR, 2007.
- [37] W. Bo, "Applied Study on the Magnetic Flux Constraint Fault Current Limiter," *Thesis for the Degree of Master of Engineering*, Jan, 2012 2012. Huazhong University of Science and Technology
- [38] L. Li, L. Aimin, and W. Kecheng, "Analysis of Short-Circuit Current Exceeding Standard of Guangdong Power Grid and Research on Limitation Measures," *Southern Power System Technology*, vol. 3, no. Suppl, pp. 14-20, 2009.
- [39] S. S. V. V.A. Centeno, P. Paretkar, D. Fan, M. Verma, S. Ming, and R. Phillips, "Literature Review of Fault Location Prediction and Detection for Distribution Systems," p. 134, 14/02/2008 2008.
- [40] T. Takagi, Y. Yamakoshi, M. Yamaura, R. Kondow, and T. Matsushima, "Development of a new type fault locator using the one-terminal voltage and current data," *power apparatus and systems, ieee transactions on*, no. 8, pp. 2892-2898, 1982.
- [41] J. Thorp, A. Phadke, and K. Karimi, "Real time voltage-phasor measurement for static state estimation," *Power Apparatus and Systems, IEEE Transactions on*, no. 11, pp. 3098-3106, 1985.
- [42] J.-A. Jiang, C.-S. Chen, and C.-W. Liu, "A new protection scheme for fault detection, direction discrimination, classification, and location in transmission lines," *Power Delivery, IEEE Transactions on*, vol. 18, no. 1, pp. 34-42, 2003.
- [43] K. Wong, H. Ryan, and J. Tindle, "Power system fault prediction using artificial neural networks," 1996.
- [44] H. Mori, "State-of-the-art overview on data mining in power systems," in *Power Systems Conference and Exposition, 2006. PSCE'06. 2006 IEEE PES*, 2006, pp. 33-34: IEEE.
- [45] D. C. Elizondo and J. De La Ree, "Analysis of hidden failures of protection schemes in large interconnected power systems," in *Power Engineering Society General Meeting, 2004. IEEE*, 2004, pp. 107-114: IEEE.

- [46] E. E. Bernabeu, J. Thorp, and V. Centeno, "Methodology for a security/dependability adaptive protection scheme based on data mining," *Power Delivery, IEEE Transactions on*, vol. 27, no. 1, pp. 104-111, 2012.
- [47] J. Chen, J. S. Thorp, and I. Dobson, "Cascading dynamics and mitigation assessment in power system disturbances via a hidden failure model," *International Journal of Electrical Power & Energy Systems*, vol. 27, no. 4, pp. 318-326, 2005.
- [48] "North American Electric Reliability Council Disturbances Analysis Working Group Database [Online]. Available: <http://www.nerc.com/~dawg/database.html>."
- [49] K. Bae and J. S. Thorp, "A stochastic study of hidden failures in power system protection," *Decision Support Systems*, vol. 24, no. 3, pp. 259-268, 1999.
- [50] G. Chen, Z. Y. Dong, D. J. Hill, G. H. Zhang, and K. Q. Hua, "Attack structural vulnerability of power grids: A hybrid approach based on complex networks," *Physica A: Statistical Mechanics and its Applications*, vol. 389, no. 3, pp. 595-603, 2010.
- [51] S. Garlapati, H. Lin, S. Sambamoorthy, S. K. Shukla, and J. Thorp, "Agent based supervision of zone 3 relays to prevent hidden failure based tripping," in *Smart Grid Communications (SmartGridComm), 2010 First IEEE International Conference on*, 2010, pp. 256-261: IEEE.
- [52] S. Saxena, A. Singh, K. Gandhi, and M. Ali, "Various Types of Circuit Breakers used in Power System for Smooth Working of the Transmission Line," *MIT International Journal of Electrical and Instrumentation Engineering*, 2012.
- [53] T. Gonen, *Electric power distribution engineering*. CRC press, 2014.
- [54] S. Natti, P. Jirutitjaroen, M. Kezunovic, and C. Singh, "Circuit breaker and transformer inspection and maintenance: probabilistic models," in *Probabilistic Methods Applied to Power Systems, 2004 International Conference on*, 2004, pp. 1003-1008: IEEE.
- [55] Y. Wu *et al.*, "Numerical modeling of arc root transfer during contact opening in a low-voltage air circuit breaker," *IEEE transactions on plasma science*, vol. 36, no. 4, pp. 1074-1075, 2008.

- [56] E. Schade, "Physics of high-current interruption of vacuum circuit breakers," *Plasma Science, IEEE Transactions on*, vol. 33, no. 5, pp. 1564-1575, 2005.
- [57] H. Knobloch, "The comparison of arc-extinguishing capability of sulfur hexafluoride (SF₆) with alternative gases in high-voltage circuit-breakers," in *Gaseous Dielectrics VIII*: Springer, 1998, pp. 565-571.
- [58] G. J. Anders, H. Maciejewski, B. Jesus, and F. Remtulla, "A comprehensive study of outage rates of air blast breakers," *Power Systems, IEEE Transactions on*, vol. 21, no. 1, pp. 202-210, 2006.
- [59] M. M. Bilac, J. J. Dougherty, W. J. Premerlani, and I. Purkayastha, "Circuit breaker and protective relay unit," ed: Google Patents, 1987.
- [60] C. Meyer, S. Schroder, and R. W. De Doncker, "Solid-state circuit breakers and current limiters for medium-voltage systems having distributed power systems," *Power Electronics, IEEE Transactions on*, vol. 19, no. 5, pp. 1333-1340, 2004.
- [61] S. M. Brahma and A. A. Girgis, "Development of adaptive protection scheme for distribution systems with high penetration of distributed generation," *Power Delivery, IEEE Transactions on*, vol. 19, no. 1, pp. 56-63, 2004.
- [62] K. Kunde, M. Kleimaier, L. Klingbeil, H. Hermann, C. Neumann, and J. Patzhold, "Integration of fast acting Electronic Fault Current Limiters (EFCL) in medium-voltage systems," in *CIREN 17th International Conference on Electricity Distribution, Barcelona, Spain*, 2003.
- [63] K.-H. Hartung and V. Schmidt, "Limitation of short circuit current by an I S-limiter," in *Electrical Power Quality and Utilisation, 2009. EPQU 2009. 10th International Conference on*, 2009, pp. 1-4: IEEE.
- [64] R. Dommerque *et al.*, "First commercial medium voltage superconducting fault-current limiters: production, test and installation," *Superconductor Science and Technology*, vol. 23, no. 3, p. 034020, 2010.
- [65] H.-S. Choi, H.-R. Kim, O.-B. Nyun, and S.-J. Kim, "Quench properties of Y-Ba-Cu-O films after overpowering quenches [superconducting fault current limiters]," *Applied Superconductivity, IEEE Transactions on*, vol. 11, no. 1, pp. 2418-2421, 2001.

- [66] J. Bock *et al.*, "Development and successful testing of MCP BSCCO-2212 components for a 10 MVA resistive superconducting fault current limiter," *Superconductor Science and Technology*, vol. 17, no. 5, p. S122, 2004.
- [67] M. Noe, K.-P. Juengst, F. Werfel, L. Cowey, A. Wolf, and S. Elschner, "Investigation of high-Tc bulk material for its use in resistive superconducting fault current limiters," *Applied Superconductivity, IEEE Transactions on*, vol. 11, no. 1, pp. 1960-1963, 2001.
- [68] D. Sarkar, A. Upadhyaya, A. Choudhury, and D. Roy, "Performance analysis of a saturated iron core superconducting fault current limiter using different core materials," in *Control, Instrumentation, Energy and Communication (CIEC), 2014 International Conference on*, 2014, pp. 387-391: IEEE.
- [69] E. M. Leung, "Superconducting fault current limiters," *Power Engineering Review, IEEE*, vol. 20, no. 8, pp. 15-18, 30, 2000.
- [70] G. Tang and M. Iravani, "Application of a fault current limiter to minimize distributed generation impact on coordinated relay protection," in *International Conference on Power Systems Transients (IPST'05), Montreal, Canada*, 2005, pp. 19-23.
- [71] G. Karady, "Principles of fault current limitation by a resonant LC circuit," in *IEE Proceedings C (Generation, Transmission and Distribution)*, 1992, vol. 139, no. 1, pp. 1-6: IET.
- [72] V. Sokolovsky, V. Meerovich, I. Vajda, and V. Beilin, "Superconducting FCL: design and application," *Applied Superconductivity, IEEE Transactions on*, vol. 14, no. 3, pp. 1990-2000, 2004.
- [73] L. Martini, M. Noe, T. Pascal, A. Hobl, and M. Bocchi, "The ECCOFLOW project: design and simulation results of a superconducting fault current limiter for operation in electricity networks," in *Proceedings CIREN2011, 21th Int. Conf. on Electricity Distribution*, 2011.
- [74] K. Bauml and U. Kaltenborn, "Inductive shielded superconducting fault current limiter-a new cost effective solution for industrial network applications," in *Petroleum and Chemical Industry Conference Europe Conference Proceedings (PCIC EUROPE), 2011*, 2011, pp. 1-7: IEEE.

- [75] Y. Nikulshin, Y. Wolfus, A. Friedman, and Y. Yeshurun, "Dynamic Inductance in Saturated Cores Fault Current Limiters," *Journal of Superconductivity and Novel Magnetism*, pp. 1-5, 2014.
- [76] Y. Shiohara, T. Taneda, and M. Yoshizumi, "Overview of materials and power applications of coated conductors project," *Japanese Journal of Applied Physics*, vol. 51, no. 1R, p. 010007, 2012.
- [77] Z. Hong *et al.*, "The development and performance test of a 10 kV resistive type superconducting fault current limiter," *Applied Superconductivity, IEEE Transactions on*, vol. 22, no. 3, pp. 5600504-5600504, 2012.
- [78] J. Bock *et al.*, "Field demonstration of world wide largest superconducting fault current limiter and novel concepts," in *Electricity Distribution, 2005. CIRED 2005. 18th International Conference and Exhibition on*, 2005, pp. 1-5: IET.
- [79] T. Verhaege *et al.*, "Experiments with a high voltage (40 kV) superconducting fault current limiter," *Cryogenics*, vol. 36, no. 7, pp. 521-526, 1996.
- [80] T. Hara, T. Okuma, T. Yamamoto, D. Ito, K. Tasaki, and K. Tsurunaga, "Development of a new 6.6 kV/1500 A class superconducting fault current limiter for electric power systems," *Power Delivery, IEEE Transactions on*, vol. 8, no. 1, pp. 182-192, 1993.
- [81] C. Neumann, "Superconducting fault current limiter (SFCL) in the medium and high voltage grid," in *Power Engineering Society General Meeting, 2006. IEEE, 2006*, p. 6 pp.: IEEE.
- [82] D. Klaus *et al.*, "Superconducting fault current limiters—UK network trials live and limiting," in *Electricity Distribution (CIRED 2013), 22nd International Conference and Exhibition on*, 2013, pp. 1-4: IET.
- [83] X. Yuan, K. Tekletsadik, L. Kovalsky, J. Bock, F. Breuer, and S. Elschner, "Proof-of-concept prototype test results of a superconducting fault current limiter for transmission-level applications," *Applied Superconductivity, IEEE Transactions on*, vol. 15, no. 2, pp. 1982-1985, 2005.
- [84] M. Chen *et al.*, "6.4 MVA resistive fault current limiter based on Bi-2212 superconductor," *Physica C: Superconductivity*, vol. 372, pp. 1657-1663, 2002.

- [85] C. A. Baldan, C. Y. Shigue, D. G. Pinatti, E. Ruppert-Filho, R. C. Freitas, and R. P. Homrich, "Resistive fault current limiter using HTS single-layer coils," *Physica C: Superconductivity*, vol. 408, pp. 937-939, 2004.
- [86] L. Martini, M. Bocchi, M. Levati, and V. Rossi, "Simulations and electrical testing of superconducting fault current limiter prototypes," *Applied Superconductivity, IEEE Transactions on*, vol. 15, no. 2, pp. 2067-2070, 2005.
- [87] C. Passos *et al.*, "Superconducting fault current limiter device based on (Hg, Re)-1223 superconductor," *Applied physics letters*, vol. 89, no. 24, pp. 242503-242503-3, 2006.
- [88] B. Gromoll *et al.*, "Resistive fault current limiters with YBCO films 100 kVA functional model," *Applied Superconductivity, IEEE Transactions on*, vol. 9, no. 2, pp. 656-659, 1999.
- [89] H. Kubota, Y. Arai, M. Yamazaki, H. Yoshino, and H. Nagamura, "A new model of fault current limiter using YBCO thin film," *Applied Superconductivity, IEEE Transactions on*, vol. 9, no. 2, pp. 1365-1368, 1999.
- [90] K. Shimohata, S. Yokoyama, T. Inaguchi, S. Nakamura, and K. Yasuda, "Quench characteristics of fault current limiting element with YBCO thin film," *Applied Superconductivity, IEEE Transactions on*, vol. 13, no. 2, pp. 2108-2111, 2003.
- [91] S. Noguchi, T. Tanikawa, and H. Igarashi, "Operating property analysis of parallelized resistive fault current limiter using YBCO thin films," *Applied Superconductivity, IEEE Transactions on*, vol. 17, no. 2, pp. 1835-1838, 2007.
- [92] S. Kim, M. Nishimoto, J. Joo, and S. Murase, "Transport characteristics of meander and bispiral types resistive fault current limiters," *Physica C: Superconductivity*, vol. 468, no. 15, pp. 2059-2062, 2008.
- [93] H. Ohsaki, M. Sekino, and S. Nonaka, "Characteristics of resistive fault current limiting elements using YBCO superconducting thin film with meander-shaped metal layer," *Applied Superconductivity, IEEE Transactions on*, vol. 19, no. 3, pp. 1818-1822, 2009.
- [94] H.-S. Choi, O.-B. Hyun, and H.-R. Kim, "Quench characteristics of resistive superconducting fault current limiters based on $\text{YBa}_2\text{Cu}_3\text{O}_7$ films," *Physica C: Superconductivity*, vol. 351, no. 4, pp. 415-420, 2001.

- [95] O.-B. Hyun *et al.*, "6.6 kV resistive superconducting fault current limiter based on YBCO films," *Applied Superconductivity, IEEE Transactions on*, vol. 15, no. 2, pp. 2027-2030, 2005.
- [96] S.-W. Yim, H.-R. Kim, O.-B. Hyun, and J. Sim, "Quench and recovery characteristics of Au/YBCO thin film type SFCL," *Physica C: Superconductivity*, vol. 463, pp. 1172-1175, 2007.
- [97] A. Usoskin *et al.*, "SUPERPOLI fault-current limiters based on YBCO-coated stainless steel tapes," *Applied Superconductivity, IEEE Transactions on*, vol. 13, no. 2, pp. 1972-1975, 2003.
- [98] A. Kudymow, M. Noe, C. Schacherer, H. Kinder, and W. Prusseit, "Investigation of YBCO coated conductor for application in resistive superconducting fault current limiters," *Applied Superconductivity, IEEE Transactions on*, vol. 17, no. 2, pp. 3499-3502, 2007.
- [99] A. Kudymow, C. Schacherer, M. Noe, and W. Goldacker, "Experimental investigation of parallel connected YBCO coated conductors for resistive fault current limiters," *Applied Superconductivity, IEEE Transactions on*, vol. 19, no. 3, pp. 1806-1809, 2009.
- [100] Y. Xie, K. Tekletsadik, D. Hazelton, and V. Selvamanickam, "Second generation high-temperature superconducting wires for fault current limiter applications," *Applied Superconductivity, IEEE Transactions on*, vol. 17, no. 2, pp. 1981-1985, 2007.
- [101] H.-R. Kim *et al.*, "Installation and testing of SFCLs," *Applied Superconductivity, IEEE Transactions on*, vol. 22, no. 3, pp. 5602704-5602704, 2012.
- [102] T. Yazawa *et al.*, "Development of 6.6 kV/600A superconducting fault current limiter using coated conductors," *Physica C: Superconductivity*, vol. 469, no. 15, pp. 1740-1744, 2009.
- [103] H.-W. Neumueller *et al.*, "Development of resistive fault current limiters based on YBCO coated conductors," *Applied Superconductivity, IEEE Transactions on*, vol. 19, no. 3, pp. 1950-1955, 2009.
- [104] H.-P. Kraemer *et al.*, "Superconducting fault current limiter for transmission voltage," *Physics Procedia*, vol. 36, pp. 921-926, 2012.

- [105] Y. Chen *et al.*, "Design and Application of Superconducting Fault Current Limiter in DC System," 2014.
- [106] S. Elschner *et al.*, "ENSYSTROB—Design, manufacturing and test of a 3-phase resistive fault current limiter based on coated conductors for medium voltage application," *Physica C: Superconductivity*, vol. 482, pp. 98-104, 2012.
- [107] A. Hobl, W. Goldacker, B. Dutoit, L. Martini, A. Petermann, and P. Tixador, "Design and production of the ECCOFLOW resistive fault current limiter," *IEEE transactions on applied superconductivity*, vol. 23, no. 3, 2013.
- [108] A. Morandi *et al.*, "Design of a DC Resistive SFCL for Application to the 20 kV Distribution System," *Applied Superconductivity, IEEE Transactions on*, vol. 20, no. 3, pp. 1122-1126, 2010.
- [109] L. Ye *et al.*, "Experimental studies of the quench behaviour of MgB₂ superconducting wires for fault current limiter applications," *Superconductor Science and Technology*, vol. 20, no. 7, p. 621, 2007.
- [110] A. Smith, A. Oliver, X. Pei, M. Husband, and M. Rindfleisch, "Experimental testing and modelling of a resistive type superconducting fault current limiter using MgB₂ wire," *Superconductor Science and Technology*, vol. 25, no. 12, p. 125018, 2012.
- [111] W. Stautner, M. Xu, S. Mine, and K. Amm, "Hydrogen cooling options for MgB₂-based superconducting systems," in *ADVANCES IN CRYOGENIC ENGINEERING: Transactions of the Cryogenic Engineering Conference-CEC*, 2014, vol. 1573, no. 1, pp. 82-90: AIP Publishing.
- [112] K. Shimohata, S. Yokoyama, I. Kodera, and K. Yasuda, "Development of kA class fault current limiting unit with YBCO thin films," *IEEJ Transactions on Power and Energy*, vol. 125, pp. 1007-1014, 2005.
- [113] "Medium and Long-Term Development Plan for Renewable Energy in China," *National Development and Reform Commission (NDRC), People's Republic of China*, September, 2007.
- [114] R. Strzelecki and G. Benysek, *Power electronics in smart electrical energy networks*. Springer, 2008.
- [115] T. Jamasb, W. J. Nuttall, and M. G. Pollitt, *Future electricity technologies and systems*. Cambridge University Press, 2006.

-
- [116] U. A. Khan, J. Seong, S. Lee, S. Lim, and B. Lee, "Feasibility analysis of the positioning of superconducting fault current limiters for the smart grid application using simulink and simpowersystem," *Applied Superconductivity, IEEE Transactions on*, vol. 21, no. 3, pp. 2165-2169, 2011.
- [117] "IEEE Standard Requirements for Liquid-Immersed Power Transformers-Corrigendum 2: Correction of A.3.2.13 Autotransformer LTC application considerations " pp. 1 - 14 Dec. 6 2013.
- [118] "Chinese Standard of Overhead Line Parameters," *Chinese Society of Electrical Engineering*, pp. 9-11, 2011.
- [119] Y. Yong and W. Qi, *Power System Analysis*. China Electric Power Press, 2007.
- [120] H. Saadat, *Power system analysis*. WCB/McGraw-Hill, 1999.
- [121] Y. He and Z. Wen, *Power System Analysis*. Huazhong University of Science and Technology Press, 2002.
- [122] A. T. Rowley, "Superconducting fault current limiters," 1995.
- [123] Y. Shirai, M. Taguchi, M. Shiotsu, H. Hatta, and T. Nitta, "Simulation study on operating characteristics of superconducting fault current limiter in one-machine infinite bus power system," *Applied Superconductivity, IEEE Transactions on*, vol. 13, no. 2, pp. 1822-1827, 2003.
- [124] "Network Protection & Automation Guide," *Alstom Grid*, 2011.
- [125] S. M. Blair, C. D. Booth, and G. M. Burt, "Current-time characteristics of resistive superconducting fault current limiters," *Applied Superconductivity, IEEE Transactions on*, vol. 22, no. 2, pp. 5600205-5600205, 2012.
- [126] P. Caspi, A. Curic, A. Maignan, C. Sofronis, and S. Tripakis, "Translating discrete-time Simulink to Lustre," in *Embedded Software*, 2003, pp. 84-99: Springer.
- [127] M. Singh, K. Panigrahi, and R. Maheshwari, "Transmission line fault detection and classification," in *Emerging Trends in Electrical and Computer Technology (ICETECT), 2011 International Conference on*, 2011, pp. 15-22: IEEE.

- [128] J. Suonan, K. Liu, and G. Song, "A novel UHV/EHV transmission-line pilot protection based on fault component integrated impedance," *Power Delivery, IEEE Transactions on*, vol. 26, no. 1, pp. 127-134, 2011.
- [129] J. Zhang *et al.*, "Development of a combined YBCO/Bi2223 coils for a model fault current limiter," *IEEE Transactions on Applied Superconductivity*, vol. 23, no. 3, pp. 5601705-5601705, 2013.
- [130] F. Zheng, C. Deng, L. Chen, S. Li, Y. Liu, and Y. Liao, "Transient performance improvement of microgrid by a resistive superconducting fault current limiter," *IEEE Transactions on Applied Superconductivity*, vol. 25, no. 3, pp. 1-5, 2015.
- [131] L. Kovalsky, X. Yuan, K. Tekletsadik, A. Keri, J. Bock, and F. Breuer, "Applications of superconducting fault current limiters in electric power transmission systems," *IEEE Transactions on Applied Superconductivity*, vol. 15, no. 2, pp. 2130-2133, 2005.
- [132] L. Ye and K.-P. Juengst, "Modeling and simulation of high temperature resistive superconducting fault current limiters," *IEEE Transactions on Applied Superconductivity*, vol. 14, no. 2, pp. 839-842, 2004.
- [133] G. Angeli *et al.*, "Status of superconducting fault current limiter in italy: final results from the in-field testing activity and design of the 9 kv/15.6 mva device," *IEEE Transactions on Applied Superconductivity*, vol. 26, no. 3, pp. 1-5, 2016.
- [134] H. S. Ruiz, X. Zhang, and T. Coombs, "Resistive-type superconducting fault current limiters: concepts, materials, and numerical modeling," *IEEE Transactions on Applied Superconductivity*, vol. 25, no. 3, pp. 1-5, 2015.
- [135] W.-J. Park, B. C. Sung, and J.-W. Park, "The effect of SFCL on electric power grid with wind-turbine generation system," *IEEE Transactions on Applied Superconductivity*, vol. 20, no. 3, pp. 1177-1181, 2010.
- [136] W.-J. Park, B. C. Sung, K.-B. Song, and J.-W. Park, "Parameter optimization of SFCL with wind-turbine generation system based on its protective coordination," *IEEE Transactions on Applied Superconductivity*, vol. 21, no. 3, pp. 2153-2156, 2011.
- [137] J. Langston, M. Steurer, S. Woodruff, T. Baldwin, and J. Tang, "A generic real-time computer simulation model for superconducting fault current limiters and its application in system protection studies," *IEEE transactions on applied superconductivity*, vol. 15, no. 2, pp. 2090-2093, 2005.

- [138] D. Colangelo and B. Dutoit, "Mv power grids integration of a resistive fault current limiter based on hts-ccs," *IEEE Transactions on Applied Superconductivity*, vol. 23, no. 3, pp. 5600804-5600804, 2013.
- [139] S. Butler, "UK Electricity Networks: The nature of UK electricity transmission and distribution networks in an intermittent renewable and embedded electricity generation future," 2001.
- [140] Y. Feng, P. Tavner, and H. Long, "Early experiences with UK Round 1 offshore wind farms," *Proceedings of the Institution of Civil Engineers: energy*, vol. 163, no. 4, pp. 167-181, 2010.
- [141] B. C. Sung, D. K. Park, J.-W. Park, and T. K. Ko, "Study on a series resistive SFCL to improve power system transient stability: modeling, simulation, and experimental verification," *IEEE transactions on industrial electronics*, vol. 56, no. 7, pp. 2412-2419, 2009.
- [142] S. Alaraifi, M. El Moursi, and H. Zeineldin, "Optimal allocation of HTS-FCL for power system security and stability enhancement," *IEEE Transactions on Power Systems*, vol. 28, no. 4, pp. 4701-4711, 2013.
- [143] S. M. Blair, C. D. Booth, and G. M. Burt, "Current-time characteristics of resistive superconducting fault current limiters," *IEEE transactions on applied superconductivity*, vol. 22, no. 2, pp. 5600205-5600205, 2012.
- [144] J. Bock, A. Hobl, J. Schramm, S. Krämer, and C. Jänke, "Resistive superconducting fault current limiters are becoming a mature technology," *IEEE Transactions on Applied Superconductivity*, vol. 25, no. 3, pp. 1-4, 2015.
- [145] D. Buhl, T. Lang, and L. Gauckler, "Critical current density of Bi-2212 thick films processed by partial melting," *Superconductor Science and Technology*, vol. 10, no. 1, p. 32, 1997.
- [146] W. Paul and J. Meier, "Inductive measurements of voltage-current characteristics between 10-12 V/cm and 10-2 V/cm in rings of Bi2212 ceramics," *Physica C: Superconductivity*, vol. 205, no. 3, pp. 240-246, 1993.
- [147] J. Bock *et al.*, "CURL 10: Development and field-test of a 10 kV/10 MVA resistive current limiter based on bulk MCP-BSCCO 2212," *IEEE transactions on applied superconductivity*, vol. 15, no. 2, pp. 1955-1960, 2005.

- [148] M. Noe, K.-P. Juengst, F. Werfel, L. Cowey, A. Wolf, and S. Elschner, "Investigation of high-Tc bulk material for its use in resistive superconducting fault current limiters," *IEEE transactions on applied superconductivity*, vol. 11, no. 1, pp. 1960-1963, 2001.
- [149] W. Paul, M. Chen, M. Lakner, J. Rhyner, D. Braun, and W. Lanz, "Fault current limiter based on high temperature superconductors—different concepts, test results, simulations, applications," *Physica C: Superconductivity*, vol. 354, no. 1, pp. 27-33, 2001.
- [150] S. Elschner, F. Breuer, A. Wolf, M. Noe, L. Cowey, and J. Bock, "Characterization of BSCCO 2212 bulk material for resistive current limiters," *IEEE transactions on applied superconductivity*, vol. 11, no. 1, pp. 2507-2510, 2001.
- [151] S. Kozak, T. Janowski, B. Kondratowicz-Kucewicz, J. Kozak, and G. Wojtasiewicz, "Experimental and numerical analysis of energy losses in resistive SFCL," *IEEE transactions on applied superconductivity*, vol. 15, no. 2, pp. 2098-2101, 2005.
- [152] T. Rettelbach and G. Schmitz, "3D simulation of temperature, electric field and current density evolution in superconducting components," *Superconductor Science and Technology*, vol. 16, no. 5, p. 645, 2003.
- [153] V. Meerovich and V. Sokolovsky, "Thermal regimes of HTS cylinders operating in devices for fault current limitation," *Superconductor Science and Technology*, vol. 20, no. 5, p. 457, 2007.
- [154] S. M. Blair, C. D. Booth, N. K. Singh, G. M. Burt, and C. G. Bright, "Analysis of energy dissipation in resistive superconducting fault-current limiters for optimal power system performance," *IEEE Transactions on Applied Superconductivity*, vol. 21, no. 4, pp. 3452-3457, 2011.
- [155] A. Morandi, "State of the art of superconducting fault current limiters and their application to the electric power system," *Physica C: Superconductivity*, vol. 484, pp. 242-247, 2013.
- [156] P. Kundur, N. J. Balu, and M. G. Lauby, *Power system stability and control*. McGraw-hill New York, 1994.
- [157] Z. Melhem, *High temperature superconductors (HTS) for energy applications*. Elsevier, 2011.

- [158] A. Colmenar-Santos, J. Pecharromán-Lázaro, C. de Palacio Rodríguez, and E. Collado-Fernández, "Performance analysis of a superconducting fault current limiter in a power distribution substation," *Electric Power Systems Research*, vol. 136, pp. 89-99, 2016.
- [159] L. Ye, M. Majoros, T. Coombs, and A. Campbell, "System studies of the superconducting fault current limiter in electrical distribution grids," *Applied Superconductivity, IEEE Transactions on*, vol. 17, no. 2, pp. 2339-2342, 2007.
- [160] W.-J. Park, B. C. Sung, and J.-W. Park, "The effect of SFCL on electric power grid with wind-turbine generation system," *IEEE Trans. Appl. Supercond.*, vol. 20, no. 3, pp. 1177-1181, 2010.
- [161] Z. Hanzelka and J. Milanovic, "Power Electronics in Smart Electrical Energy Networks," 2008.
- [162] M. Vojenčiak *et al.*, "Study of ac loss in Bi-2223/Ag tape under the simultaneous action of ac transport current and ac magnetic field shifted in phase," *Superconductor Science and Technology*, vol. 19, no. 4, p. 397, 2006.
- [163] A. Campbell and J. Evetts, "Flux vortices and transport currents in type II superconductors," *Advances in Physics*, vol. 21, no. 90, pp. 199-428, 1972.
- [164] A. Badía-Majós, C. López, and H. Ruiz, "General critical states in type-II superconductors," *Physical Review B*, vol. 80, no. 14, p. 144509, 2009.
- [165] H. Ruiz, C. López, and A. Badía-Majós, "Inversion mechanism for the transport current in type-II superconductors," *Physical Review B*, vol. 83, no. 1, p. 014506, 2011.
- [166] *American Superconductor Amperium HTS Wire*. Available: www.amsc.com/solutions-products/hts_wire.html
- [167] *SuperPower 2G HTS Wire*. Available: http://www.superpower-inc.com/system/files/SP_HTS+Energy_2014_v1.pdf
- [168] *Shanghai Superconductor Technology Co. Ltd. 2G HTS strip*. Available: <http://www.shsctec.com/Pages/SpecialProductList.aspx?ID=64&cl=en>
- [169] *SuperOx 2G HTS Wire*. Available: <http://www.superox.ru/products/0001.pdf>

- [170] G. Blatter, M. V. Feigel'man, V. B. Geshkenbein, A. I. Larkin, and V. M. Vinokur, "Vortices in high-temperature superconductors," *Reviews of Modern Physics*, vol. 66, no. 4, p. 1125, 1994.
- [171] L. Rostila *et al.*, "How to determine critical current density in YBCO tapes from voltage–current measurements at low magnetic fields," *Superconductor Science and Technology*, vol. 20, no. 12, p. 1097, 2007.
- [172] D. Harshman *et al.*, "Magnetic penetration depth in single-crystal Y Ba 2 Cu 3 O 7– δ ," *Physical Review B*, vol. 39, no. 1, p. 851, 1989.
- [173] F. Grilli, F. Sirois, V. M. Zermeno, and M. Vojenčiak, "Self-consistent modeling of the I_{c} of HTS devices: How accurate do models really need to be?," *IEEE Transactions on Applied Superconductivity*, vol. 24, no. 6, pp. 1-8, 2014.
- [174] D. Hu, M. D. Ainslie, M. J. Raine, D. P. Hampshire, and J. Zou, "Modeling and comparison of in-field critical current density anisotropy in high-temperature superconducting (HTS) coated conductors," *IEEE Transactions on Applied Superconductivity*, vol. 26, no. 3, pp. 1-6, 2016.
- [175] T. Kiss *et al.*, "Critical current properties in HTS tapes," *Physica C: Superconductivity*, vol. 392, pp. 1053-1062, 2003.
- [176] V. F. Solovyov and Q. Li, "Application of active quenching of second generation wire for current limiting," *Physica C: Superconductivity and its applications*, vol. 519, pp. 130-136, 2015.
- [177] *Shanghai Superconductor Technology Co. Ltda. 2G HTS strip*. Available: <http://shsctec.com/Pages/SpecialProductList.aspx?ID=64&cl=en>
- [178] J. Geng, C. Li, and T. A. Coombs, "A fast AC field controlled impedance in HTS coated conductors: response speed and electric field value," *IEEE Transactions on Applied Superconductivity*, 2017.
- [179] G. P. Mikitik and E. H. Brandt, "Generation of a dc voltage by an ac magnetic field in type-II superconductors," *Physical Review B*, vol. 64, no. 9, p. 092502, 2001.
- [180] V. Andrianov, V. Zenkevich, V. Kurguzov, V. Sytchev, and F. Ternovskii, "Effective resistance of an imperfect type-II superconductor in an oscillating magnetic field," Inst. of Low Temperature, Moscow 1970.

-
- [181] M. Oomen, J. Rieger, M. Leghissa, B. Ten Haken, and H. Ten Kate, "Dynamic resistance in a slab-like superconductor with $J_c(B)$ dependence," *Superconductor Science and Technology*, vol. 12, no. 6, p. 382, 1999.
- [182] W. Carr Jr, *AC loss and macroscopic theory of superconductors*. CRC Press, 2001.
- [183] M. Risse, M. Aikele, S. Doettinger, R. Huebener, C. Tsuei, and M. Naito, "Dissipation in the superconducting mixed state in the presence of a small oscillatory magnetic-field component," *Physical Review B*, vol. 55, no. 22, p. 15191, 1997.
- [184] V. F. Solovyov and Q. Li, "Fast high-temperature superconductor switch for high current applications," *Applied Physics Letters*, vol. 103, no. 3, p. 032603, 2013.
- [185] E. Martinez, L. Angurel, J. Pelegrin, Y. Xie, and V. Selvamanickam, "Thermal stability analysis of YBCO-coated conductors subject to over-currents," *Superconductor Science and Technology*, vol. 23, no. 2, p. 025011, 2009.
- [186] M. Sumption *et al.*, "Thermal diffusion and quench propagation in YBCO pancake coils wound with ZnO and Mylar insulations," *Superconductor Science and Technology*, vol. 23, no. 7, p. 075004, 2010.
- [187] X. Zhang, Z. Zhong, H. Ruiz, J. Geng, and T. Coombs, "General approach for the determination of the magneto-angular dependence of the critical current of YBCO coated conductors," *Superconductor Science and Technology*, vol. 30, no. 2, p. 025010, 2016.